TWO-DIMENSIONAL TRANSONIC AERODYNAMIC DESIGN AND ANALYSIS USING THE EULER EQUATIONS

by

MARK DRELA

S.M., Massachusetts Institute of Technology (1983)

S.B., Massachusetts Institute of Technology (1982)

Submitted to the
Department of Aeronautics and Astronautics
in partial fulfillment of the requirements
of the Degree of

**DOCTOR OF PHILOSOPHY IN
AERONAUTICS AND ASTRONAUTICS**

at the

MASSACHUSETTS INSTITUTE OF TECHNOLOGY

December 1985

Signature of Author _____
Dept. of Aeronautics and Astronautics, 19 Dec 1985

Certified by _____
Professor Jack L. Kerrebrock Thesis Supervisor

Certified by _____
Professor W.T. Thompkins, Jr. Thesis Committee

Certified by _____
Professor Earll M. Murman Thesis Committee

Accepted by _____
Professor Harold Y. Wachman Chairman, Departmental
Graduate Committee

TWO-DIMENSIONAL TRANSONIC AERODYNAMIC DESIGN AND ANALYSIS USING THE EULER EQUATIONS

by

Mark Drela

Submitted to the Department of Aeronautics and Astronautics on 2 December 85 in partial fulfillment of the requirements of the Degree of Doctor of Philosophy in Aeronautics and Astronautics

Abstract

A method is developed for the solution of the steady two-dimensional Euler equations with viscous corrections for transonic design and analysis problems. The steady finite volume integral equations are formulated on an intrinsic streamline grid, and are solved using a global Newton method. Conservative differencing together with artificial bulk viscosity in supersonic regions permit correct shock capturing. The design capability of the method stems from the streamline-based grid and Newton solution method, which allow both direct and inverse boundary conditions and constraints to be readily applied to the governing equations. For all boundary condition types, the effects of boundary layers and wakes on the inviscid flow are modeled by the displacement thickness concept. The boundary layer and wake parameters are described by compressible integral boundary layer equations which are coupled to the inviscid flow and are included in the global Newton solution scheme. This coupling procedure gives stable convergence for flows with limited separation regions. A transition criterion based on the Orr-Sommerfeld equation is developed and applied to transitional separation bubbles. Accurate drag predictions are obtained for subsonic and shocked transonic airfoils. Design examples involving airfoils and cascades are presented.

Thesis Supervisor: Jack L. Kerrebrock

Title: Maclaurin Professor of Aeronautics and Astronautics

Acknowledgements

I would like to thank all the people I've known at MIT for helping to make my tour of duty here well worth it. In particular, I'd like to give thanks to Mike Giles, math-stud extraordinaire, for sharing the Rats!'s and Rah!'s of this research effort. To Tom Roberts, who can (and does) laugh in the face of just about anything, I'd like to give thanks for his friendship, his critical comments, and for helping to keep the local Chinese restaurant business booming. I'm grateful to Bob Haimes (for keeping that vital silicon beastie humming), John Dannenhoffer (for his truly unbounded frankness in all aspects of life), Ken Powell, Steve Allmaras, Bernard Loyd, and the rest of the CFDL crew (for being such a swell bunch of guys).

I would particularly like to thank Professor Tilt Thompkins, my first thesis supervisor, for his advice and for letting me diverge into butterflies and wings and things whenever I felt like it. To Professor Jack Kerrebrock, my second and last thesis supervisor, I give thanks for his endless optimism and support in all my endeavors. And also, I'd like to thank Professor Earll Murman for his help and advice.

Finally, I would like to thank my parents and my sister for their support and encouragement throughout all these years.

This work was supported by the Air Force Office of Scientific Research grant F49620-78C-0084, with Dr. James D. Wilson as technical monitor.

* * *

Observation: Hindsight is always 20/20, foresight is invariably blind, and Braille is much too difficult.

Table of Contents

List of Figures

6.1 Laminar closure relations

6.2 Comparison of finite difference, dissipation-closure, and Thwaites' methods for incompressible laminar flow

6.3 Turbulent and laminar skin friction correlations

6.4 Turbulent shape parameter correlation

6.5 Typical turbulent velocity and total shear profiles

6.6 Equilibrium G-β locus

6.7 Orr-Sommerfeld spatial amplification curves

6.8 Boundary layer variable locations (suction side)

6.9 Wake displacement thickness

6.10 Division of boundary layer equation variables between Jacobian matrix blocks

6.11 Modified $\mathbf{A}_i$ block structure

7.1.1 Effect of domain size for isolated airfoil

7.1.2 Calculated and exact C_p distributions for Joukowsky airfoil

7.1.3 Converged grid near Joukowsky airfoil

7.2.1 Calculated and experimental pressure distributions for RAE 2822 airfoil (M_∞ = 0.726 , Re = 6.5e6)

7.2.2 Measured and calculated suction surface δ^* and θ distributions for RAE 2822 (Case 6 of ref.[12])

7.2.3 Measured and calculated suction and pressure surface H distributions for RAE 2822

7.3.1 Calculated and experimental pressure distributions for RAE 2822 airfoil (M_∞ = 0.750 , Re = 6.2e6)

7.3.2 Measured and calculated suction surface δ^* and θ distributions for RAE 2822 (Case 10 of ref.[12])

7.3.3 Measured and calculated suction and pressure

List of Symbols

$\vec{\mathbf{A}}$	normal cell face vector
A_1, A_2 ...	prescribed-pressure degrees of freedom
A_n	cross-sectional streamtube area
$\vec{\mathbf{B}}$	streamline cell face vector
C_D	dissipation coefficient, drag coefficient
C_f	skin friction coefficient
C_L	lift coefficient
C_τ	max shear coefficient
D	drag
D_x, D_y	far-field doublet components
F_1, F_2...	prescribed-pressure DOF shape functions
G	Clauser's shape parameter
h_t	stagnation enthalpy
H, H^*, H^{**}	shape parameters
H_k, H_k^*	kinematic shape parameters
i, j	grid indices
I, J	maximum grid indices
m	streamtube mass flux ; u_e gradient parameter (in Chapter 6)
M	Mach number
n	local normal coordinate
$\tilde{n}$	disturbance amplification ratio
Δn	gap between streamline and wall
p	pressure (on normal cell face)
$\vec{\mathbf{q}}$	velocity
q	speed $= \lvert\vec{\mathbf{q}}\rvert$
Re_θ	momentum thickness Reynolds number
$\hat{\mathbf{s}}$	unit velocity vector $= \vec{\mathbf{q}}/q$
S_{inl}, S_{out}	cascade inlet and outlet flow slopes
u_s	effective wall slip velocity
u, v	velocity components
x, y	Cartesian coordinates

α	freestream angle of attack
β	$\sqrt{1-M_\infty^2}$; Clauser's pressure gradient parameter (in Chapter 6)
γ	ratio of specific heats (C_p/C_v)
γ_{tr}	transition intermittency factor
Γ	airfoil circulation
δ	boundary layer thickness
δ^*	displacement thickness
δ^{**}	density thickness
θ	momentum thickness
θ^*	kinetic energy thickness
ξ, η	local coordinates along and normal to boundary layer
λ	artificial bulk viscosity coefficient
μ	dynamic viscosity
ν	Newton iteration index
Π	pressure (on streamline cell face)
ρ	density
ρ_t	stagnation density
σ	fractional arc length from leading to trailing edge
Σ	airfoil source strength
τ_w	wall shear stress
Φ, ϕ	total and perturbation velocity potentials

Subscripts and Superscripts

$( )_e$	quantity at edge of boundary layer
$( )_t$	stagnation quantity
$( )_x$	x-component
$( )_y$	y-component
$( )_{i,j}$	quantity at grid node i,j
$( )_i$	quantity at left cell face
$( )_2$	quantity at right cell face
$( )^-$	quantity at bottom cell face
$( )^+$	quantity at top cell face
$( )_\infty$	freestream quantity

1. INTRODUCTION

Numerical solution of the fundamental governing equations of fluid flow is a very powerful aid to aerodynamic design. The traditional approach to design is to rely on wind tunnel data or even actual flight data as a guide for improvement. Unfortunately, both tunnel tests and flight tests are time consuming and extremely expensive, particularly in the transonic flow regime. This sets a severe limit on the amount of detailed design improvement which can be accomplished in a given cost and time schedule. The use of numerical simulation rather than wind tunnel testing to predict aerodynamic characteristics greatly increases the amount of design refinement which can be performed. This is due to both the relatively low cost of computation and the ease with which design changes can be made and evaluated.

Many numerical design algorithms of greatly varying sophistication and complexity have been developed to date. Virtually all of these can be classified as either inverse methods or optimization methods. Inverse methods deal with the determination of the body geometry which will produce a given surface pressure distribution. The methods of Lighthill [32,33], Tranen [48], Carlson [5], Volpe and Melnik [51], and Bauer, Garabedian, Korn, and Jameson [1] fall into this category. Optimization methods typically involve the linking of a direct aerodynamic solver, which accepts a body geometry as input, with an optimization algorithm to minimize some object function, such as drag or the integrated difference between the actual and target pressure distributions. Examples of such an approach are those of Vanderplaats [49], and Hicks [26].

Each category has its advantages and disadvantages. The inverse methods are relatively fast but usually leave the designer with only indirect control over the body geometry via the specified pressure distribution. Some methods, such as those of Carlson [5], and the Boeing PANAIR design option [43], also treat the more general mixed-

inverse problem. Here, the geometry is prescribed on part of the body and the pressure is prescribed on the rest. This gives the designer somewhat better control over the overall geometry. The optimization methods generally give the designer more control over non-aerodynamic features, since they permit arbitrary constraints to be imposed on the final design. They also allow multi-point design provided a suitable object function can be defined. On the negative side, the optimization methods can require as much as two orders of magnitude more computer time than the inverse methods. For this reason, they currently cannot be used for routine design work in an industrial environment.

The design aspect of the design/analysis method developed in this thesis falls under the category of inverse methods with mixed-inverse capability. It has several features, however, which distinguish it from the inverse methods listed above. Virtually all compressible flow design methods developed to date are based on either a linearized-panel or a full-potential formulation. The present method is based on a conservative formulation of the Euler equations to permit accurate analysis of shocked transonic flows. An equally important feature is the method's computational speed. For airfoil grids which give better than engineering accuracy, a direct solution requires no more CPU time than a state-of-the-art time-marching Euler solver. For cascade grids, the present method is considerably faster. In addition, an inverse solution with the present method requires roughly the same amount of CPU time as a direct solution, making the method fast enough to be used in interactive design/analysis sessions on a minicomputer. Finally, the present method incorporates a new boundary-layer coupling procedure which permits accurate loss predictions in both design and analysis calculations with or without limited separation regions. This inclusion of the boundary layer calculation does not significantly add to the computation time.

An important feature of the present design/analysis method which further enhances its speed is that the change between design and ana-

lysis modes and vice versa is through a simple boundary condition switch. A solution of a design problem is thus guaranteed to be a solution of an analysis problem with the same geometry and freestream conditions. This represents a considerable CPU time savings over inverse methods such as those of Tranen [48] and Carlson [5], whose design solutions do not exactly satisfy the discrete equations of motion and hence require additional analysis calculations to verify any design solution. Another important feature is that design solutions can be performed with the boundary layer coupling included. With this option, a coupled viscous analysis does not have to be performed to verify a design solution since the design solution is already a solution to the analysis problem. This again results in significant CPU time savings.

* * *

Transonic flow fields are governed by the full Reynolds-averaged Navier-Stokes equations. However, the viscous effects in high Reynolds number flows of interest are confined to thin boundary layers and wakes, and the Euler equations can be used to describe the inviscid part of the flow. The further assumption of irrotational flow would result in the potential equation, which can be solved more economically than the Euler equations. However, the potential equation does not capture shocks properly because it cannot allow vorticity production, and has non-unique solutions in certain Mach number ranges as shown by Salas et al [41]. As a result, the potential equation can give large errors in shocked flows, and for this reason the Euler equations are solved here instead.

The present design/analysis method is based on a novel discretization and solution technique for the steady Euler equations. The discretization is based on an intrinsic grid in which one set of coordinate lines corresponds to streamlines and hence there is no convection across the corresponding faces of the conservation cells. This type of coordinate system is very attractive for the steady state Euler equa-

tions. Both the continuity and energy equations are replaced by the simple conditions of constant mass flux and stagnation enthalpy in each streamtube, thus reducing the number of unknowns per grid node from four to two. With conventional finite-volume discretization, all four equations and four unknowns per grid node must be retained in general, and only the energy equation can be eliminated in the special case of constant upstream total enthalpy. Another advantage of a streamline grid is that there is no numerical diffusion of entropy or enthalpy, these quantities being only convected along streamtubes. The only way signals propagate between streamtubes is through the streamline geometry and through the pressure field. Thus, a streamline-coordinate-based scheme faithfully reproduces the analytic information propagation mechanisms of the steady Euler equations. The older streamline curvature methods, such as that of Novak [39], take full advantage of these properties of intrinsic coordinates. However, the streamline curvature methods are not conservative and their iterative solvers tend to be unstable in supersonic regions. This makes them unsuitable for shocked transonic flows. The present streamtube formulation is fully conservative, and together with artificial bulk viscosity and a stable Newton solution procedure, shocked transonic flows can be readily computed.

The key feature of the present discretization scheme which permits inverse solutions to be performed is that since the streamline grid evolves as part of the solution, the airfoil shape (which is defined by two particular streamlines) can evolve as well. In the discrete equations, it is as easy to specify that the surface pressure match some given distribution as it is to specify that the surface streamlines match the airfoil shape. Special constraints must be imposed to ensure the resulting body shape is closed. These constraints can be identified with the classical prescribed-velocity constraints of Lighthill [32]. For incompressible flow, Lighthill proved that specifying both the freestream pressure and the surface pressure distribution leads to an ill-posed problem and/or an open body shape if the surface pressure

distribution does not satisfy certain integral constraints. Volpe and Melnik [51] conclude that constraints also exist for compressible potential flow, and their inverse calculation procedure is designed to satisfy these constraints.

To accurately predict the drag on an airfoil, some sort of boundary layer and wake calculation must be performed. The traditional approach is to use the pressure distribution from a purely inviscid calculation as input to a direct boundary layer and wake calculation. An implicit assumption in this procedure is that the boundary layers and wake do not significantly affect the inviscid pressure distribution. For transonic flows such an assumption is questionable, and for separating flows it is outright wrong. In the case of transonic flow, the strong effect of the viscous layers on the inviscid flow is primarily due to the overall sensitivity of the transonic flowfield to surface perturbations, especially if shock waves are present. At separation, the strong viscous effect is due to the theoretically infinite sensitivity of the displacement thickness to pressure gradient variations.

A much more accurate viscous calculation procedure which mostly eliminates the errors inherent in the small-viscous-effect assumption is to take account of the presence of the viscous layers in the inviscid calculation. This procedure is commonly referred to as boundary layer coupling. As analyzed by Lighthill [34], the leading order effect of the viscous layers is to displace the inviscid flow away from the body or wake by a distance equal to the displacement thickness. The classical boundary layer coupling approach is to first perform a purely inviscid calculation, and use the resulting pressure distribution to obtain a displacement thickness distribution. This displacement thickness is then used to modify the effective body shape which is then used to recalculate a new inviscid pressure distribution, and the process is repeated. Unfortunately, this process tends to be unstable unless the geometry updating step is severely underrelaxed, as was

shown by Wigton and Holt [56]. The underrelaxation leads to very poor convergence rates and high computational costs. Also, if separation occurs, the direct boundary layer calculation cannot continue, and the classical coupling approach will invariably fail. A method which mostly eliminates these difficulties is the semi-inverse coupling approach where the boundary layer calculation is performed in the inverse mode with the displacement thickness or the mass defect prescribed. The resulting pressure distribution is then compared with the inviscid pressure distribution and the difference is used to obtain a new displacement thickness or mass defect distribution from some interaction law formula (Carter [6]). A refinement of this procedure is the quasi-simultaneous coupling approach (Veldman [50], Edwards and Carter [17]), where the specified displacement thickness or mass defect distribution is updated simultaneously with the boundary layer calculation.

The coupling approach developed in this thesis is fundamentally different from the classical, semi-inverse, or quasi-simultaneous methods. Instead of the usual space-marching boundary layer solution every viscous-inviscid iteration, the boundary layer equations for all streamwise stations are included in the global Newton system and solved together with the inviscid equations as a fully-coupled system. There are many advantages of this approach as compared with the other coupling methods. One advantage is that an interaction law is not required, since the Newton solution procedure automatically propagates the viscous displacement effects throughout the domain every iteration. This gives a very robust coupling algorithm. Another advantage is that the very rapid convergence rate of the Newton procedure produces computation times which are nearly the same as for purely inviscid cases. Hence the computational cost penalty for the viscous coupling is essentially negligible.

The Newton solution procedure is an integral part of the overall design and analysis method developed in this thesis. Conventional Euler solvers use pseudo-time marching procedures to converge the

unsteady Euler equations to steady state. The present method solves the steady state Euler equations directly. Furthermore, most of the equations associated with the inverse and boundary layer coupling problems are not readily put into unsteady forms, making time marching even less applicable. The Newton method, however, is applicable to any well-posed linear or non-linear system of equations.

One of the features of the Newton solution method is that, unlike a time-marching method, it converges extremely rapidly once the partially converged solution is close to the exact solution. This is a very valuable property in interactive design work, where after some starting solution is calculated, design changes are usually made in small increments. Hence, after a typical design change the resulting design problem will have a good starting approximation from the previous solution and will thus converge very rapidly. Typically, only one or two Newton iterations are required for minor prescribed-pressure distribution changes. On a minicomputer such as a VAX-11/780, this represents between 40 seconds and 4 minutes of CPU time for engineering-accuracy grids. Clearly the method is fast enough for interactive use.

Another advantage of the Newton solution method is that it allows the calculation of sensitivities with respect to global parameters at virtually no additional cost. The usual method of obtaining a global parameter sensitivity--by perturbing the parameter, calculating a new solution, and taking a finite difference quotient--is expensive and is subject to numerical noise. With the Newton method, the calculation of additional solutions is not necessary. For example, in addition to the usual lift and drag coefficients C_L and C_D, analytically-accurate sensitivities such as $\partial C_L/\partial\alpha$, $\partial C_D/\partial\alpha$, and $\partial C_D/\partial M_\infty$ are obtained from a single point calculation. The result is that integral quantities such as C_L can be easily prescribed since the sensitivity $\partial C_L/\partial\alpha$ is all that is required to drive the angle of attack α to a specified C_L. Other sensitivities such as $\partial C_D/\partial M_\infty$ can be used to monitor the onset of transonic drag rise as design calculations are carried out.

* * *

It must be mentioned here that the necessary stability and well-posedness analyses of the streamtube formulation which form the core of the present design/analysis method were derived and presented in the PhD thesis of Michael Giles [19]. Giles also performed detailed order of accuracy studies which clearly show the streamtube formulation to be second-order accurate, at least for shock-free flows. Thus, Giles' thesis is a solid foundation on which the design and boundary layer coupling capabilities of the present work are built.

The presentation approach in this thesis is to first derive the Euler equations as discretized with the basic streamtube formulation, which is done in Chapter 2. The boundary conditions and constraints necessary to close the direct problem are presented in Chapter 3. Chapter 4 describes the Newton solution procedure and implementation in detail. The inverse problem theory and discrete formulation are presented in Chapter 5, together with the linearizations necessary for the Newton method. In Chapter 6, the integral boundary layer formulation, transition criterion, and coupling procedures are derived. The modifications to the inviscid Newton solver which must be made to solve the coupled boundary layer problem are also presented in Chapter 6. Finally, results and concluding remarks are given in Chapters 7 and 8.

2. STEADY STATE EQUATIONS

2.1 Euler Equations

The discrete Euler equation set is derived from the integral form of the steady state, two-dimensional Euler equations. The integral equations are applied to a closed control volume C with outward unit normal $\hat{n}$, as shown in Figure 2.1.

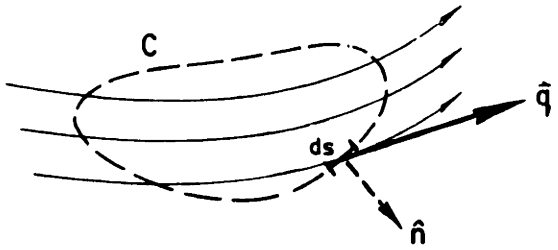

Figure 2.1 Control volume for integral Euler equations

Mass equation $$\oint \rho \vec{q} \cdot \hat{n} \, ds = 0 \qquad (2.1)$$

Momentum equation $$\oint \left(\rho (\vec{q} \cdot \hat{n}) \vec{q} + p \hat{n} \right) ds = 0 \qquad (2.2)$$

Energy equation $$\oint \rho \vec{q} \cdot \hat{n} \, h_t \, ds = 0 \qquad (2.3)$$

The discrete Euler equations used are an approximation to these equations in which the curve C is the boundary of an area usually referred to as a conservation cell. This approach is standard in computational fluid dynamics, but a unique feature of this implementation is that the cells are defined such that one pair of opposing faces are streamlines of the flow and so there is no mass flux across them. Thus the only contribution to the above integrals from these two faces is the pressure term in equation (2.2). This means that the density and

velocity need only be defined on the other two faces. Also, the direction of the velocity must somehow be related to the local geometry to be consistent with the statement that two of the faces are streamlines. A feature of this formulation which also is the basis of streamline curvature schemes but which is not found in standard time-marching Euler solvers is that the grid is not known a priori and must be determined as part of the solution.

A typical conservation cell is shown in Figure 2.2. The geometry variables (x,y) are located at the grid nodes marked ×. The cell nodes marked as • are defined to be at the midpoints of the lines connecting the grid nodes. The upper and lower bent faces of the cell are the streamline faces across which there is no mass flux. In this chapter, the geometry node numbering convention shown in Figure 2.2 is used when discussing the discrete Euler equations for a particular cell.

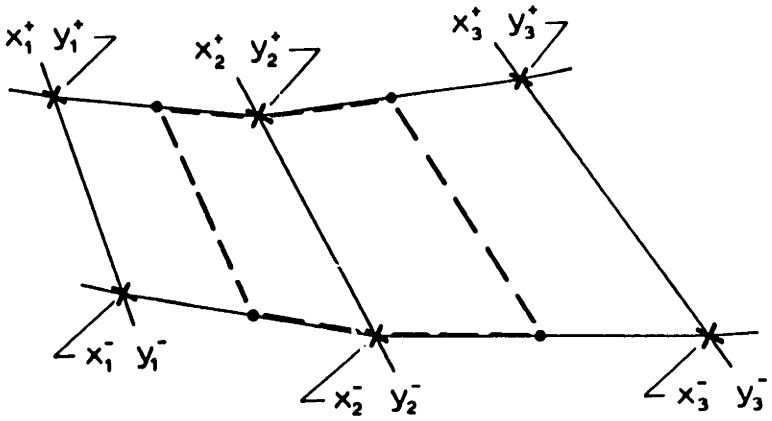

Figure 2.2 Conservation cell and defining geometry locations

Four vectors which need to be defined are the vectors along the faces of the cell, which are illustrated in Figure 2.3. For the bent streamline faces the vectors are the vector sum of the two parts.

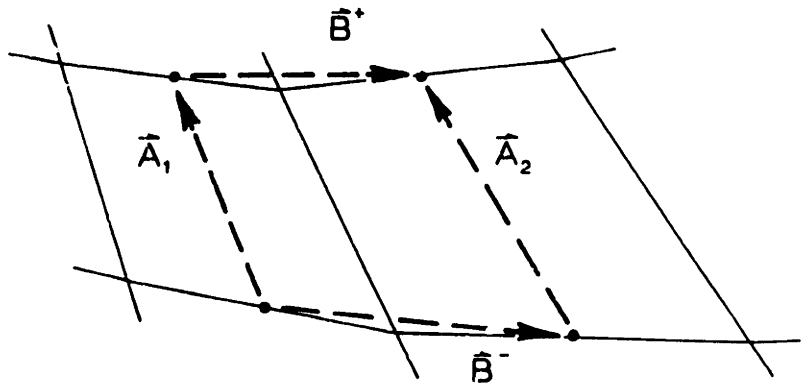

Figure 2.3 Conservation cell face vectors

$$A_{x_1} = \frac{1}{2}(x_1^+ + x_2^+) - \frac{1}{2}(x_1^- + x_2^-) \quad , \quad A_{y_1} = \frac{1}{2}(y_1^+ + y_2^+) - \frac{1}{2}(y_1^- + y_2^-) \qquad (2.4a,b)$$

$$A_{x_2} = \frac{1}{2}(x_2^+ + x_3^+) - \frac{1}{2}(x_2^- + x_3^-) \quad , \quad A_{y_2} = \frac{1}{2}(y_2^+ + y_3^+) - \frac{1}{2}(y_2^- + y_3^-) \qquad (2.4c,d)$$

$$B_x^- = \frac{1}{2}(x_3^- - x_1^-) \quad , \quad B_y^- = \frac{1}{2}(y_3^- - y_1^-) \qquad (2.4e,f)$$

$$B_x^+ = \frac{1}{2}(x_3^+ - x_1^+) \quad , \quad B_y^+ = \frac{1}{2}(y_3^+ - y_1^+) \qquad (2.4g,h)$$

Two additional vectors which it is convenient to define are $\vec{S}$, which is the average of $\vec{B}^-$ and $\vec{B}^+$, and $\vec{N}$, which is the average of $\vec{A}_1$ and $\vec{A}_2$.

$$S_x = \frac{1}{2}(B_x^- + B_x^+) \quad , \quad S_y = \frac{1}{2}(B_y^- + B_y^+) \qquad (2.5a,b)$$

$$N_x = \frac{1}{2}(A_{x_1} + A_{x_2}) \quad , \quad N_y = \frac{1}{2}(A_{y_1} + A_{y_2}) \qquad (2.5c,d)$$

Since the nodes $(x_1^+, y_1^+), (x_2^+, y_2^+), (x_3^+, y_3^+)$ and $(x_1^-, y_1^-), (x_2^-, y_2^-), (x_3^-, y_3^-)$ are defined to lie on streamlines, the local velocity direction must be related to them. This is accomplished by defining the unit flow vector

$\hat{s}_1$ to be tangent to the line joining the average of nodes 1^+ and 1^- to the average of nodes 2^+ and 2^-. The unit flow vector $\hat{s}_2$ is defined similarly. Both are shown in Figure 2.4, and their definitions are given below.

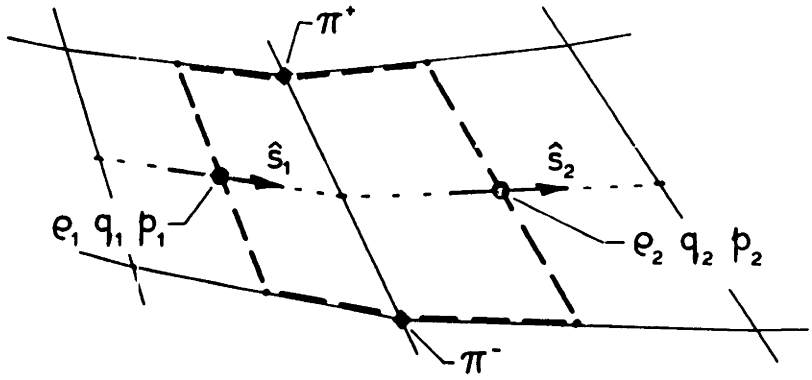

Figure 2.4 State variables and unit velocity $\hat{s}$ vectors

$$s_{x_1} = (x_2^- + x_2^+)/2 - (x_1^- + x_1^+)/2 \quad , \quad s_{y_1} = (y_2^- + y_2^+)/2 - (y_1^- + y_1^+)/2 \qquad (2.6a,b)$$

$$s_1 = (s_{x_1}^2 + s_{y_1}^2)^{\frac{1}{2}} \quad , \quad \hat{s}_{x_1} = s_{x_1}/s_1 \quad , \quad \hat{s}_{y_1} = s_{y_1}/s_1 \qquad (2.6c\text{-}e)$$

$$s_{x_2} = (x_3^- + x_3^+)/2 - (x_2^- + x_2^+)/2 \quad , \quad s_{y_2} = (y_3^- + y_3^+)/2 - (y_2^- + y_2^+)/2 \qquad (2.7a,b)$$

$$s_2 = (s_{x_2}^2 + s_{y_2}^2)^{\frac{1}{2}} \quad , \quad \hat{s}_{x_2} = s_{x_2}/s_2 \quad , \quad \hat{s}_{y_2} = s_{y_2}/s_2 \qquad (2.7c\text{-}e)$$

The velocity at the midpoint of the left face of the conservation cell is thus defined to have direction $\hat{s}_1$ and magnitude q_1 so that $\vec{q}_1 = q_1 \hat{s}_1$. The final geometric quantities to be defined are the normal areas A_{n_1} and A_{n_2}, which are the vector dot products of the unit velocity vectors and the normal area vectors of the faces. Since $\vec{A}_1$ and $\vec{A}_2$ are defined along the faces, not normal to them, the actual definitions of A_{n_1} and A_{n_2} are,

$$A_{n_1} = s_{x_1} A_{y_1} - s_{y_1} A_{x_1} \equiv |\hat{s}_1 \times \vec{A}_1| \quad , \quad A_{n_2} = s_{x_2} A_{y_2} - s_{y_2} A_{x_2} \equiv |\hat{s}_2 \times \vec{A}_2| \qquad (2.8a,b)$$

where the operator | | is defined to mean taking the scalar component in the third (out of plane) dimension, and will only be applied to vectors having only a component in the third dimension. It is important to note that the scalar value given by | | may be positive or negative depending on the direction of the vector. The operator | | does <u>not</u> return the absolute value and so is an unconventional operator, but one that is very convenient in this application.

The flow variables ρ, q, and p, denoting the density, speed and pressure, are located at the midpoints of the faces which are not streamlines, as shown in Figure 2.4. Another pressure variable, denoted differently by Π for clarity, is located on the streamline faces where, as previously noted, no other flow variables are required.

The discrete mass equation is simply a statement that the mass flux along a streamtube is a constant.

$$m = \rho_1 q_1 A_{n_1} = \rho_2 q_2 A_{n_2} \qquad (2.9)$$

With due regard to the directions of the vectors $\vec{A}_1, \vec{A}_2, \vec{B}^-$ and $\vec{B}^+$ the discrete approximations to the x and y-components of the integral form of the momentum equation (2.2) are,

$$\begin{aligned} & mq_1 \hat{s}_{x_1} - mq_2 \hat{s}_{x_2} + p_1 A_{y_1} - p_2 A_{y_2} + \Pi^+ B_y^+ - \Pi^- B_y^- \\ &= mq_1 \hat{s}_{x_1} - mq_2 \hat{s}_{x_2} + (p_1 - p_2) N_y + (\Pi^+ - \Pi^-) S_y + \tfrac{1}{2}(\Pi^+ + \Pi^- - p_1 - p_2)(B_y^+ - B_y^-) \\ &= 0 \end{aligned} \qquad (2.10)$$

$$\begin{aligned} & mq_1 \hat{s}_{y_1} - mq_2 \hat{s}_{y_2} - p_1 A_{x_1} + p_2 A_{x_2} - \Pi^+ B_x^+ + \Pi^- B_x^- \\ &= mq_1 \hat{s}_{y_1} - mq_2 \hat{s}_{y_2} - (p_1 - p_2) N_x - (\Pi^+ - \Pi^-) S_x - \tfrac{1}{2}(\Pi^+ + \Pi^- - p_1 - p_2)(B_x^+ - B_x^-) \\ &= 0 \end{aligned} \qquad (2.11)$$

The step from the first line to the second line in these two equations is achieved using the definitions of $\vec{S}$ and $\vec{N}$, and the identity $\vec{B}^+ - \vec{B}^- = \vec{A}_2 - \vec{A}_1$.

The energy equation reduces to the statement that the stagnation enthalpy is constant along a streamtube, although of course the value of the stagnation enthalpy, like the value of the mass flux, may vary from one streamtube to another.

$$h_t = \frac{\gamma}{\gamma-1}\frac{p_1}{\rho_1} + \frac{1}{2}q_1^2 = \frac{\gamma}{\gamma-1}\frac{p_2}{\rho_2} + \frac{1}{2}q_2^2 \qquad (2.12)$$

2.2 Auxiliary pressure relation

The discrete Euler equations given above require an additional relation to constrain the average value of Π in each cell. In a uniform flow, the pressure p on the normal cell faces (Figure 2.4) is related to ρ and q through the mass equation (2.9) and energy equation (2.12). However, the streamline cell face pressure Π can take on any value, since the momentum equation (2.11) only constrains the difference between Π^- and Π^+. For consistency the average local value of Π must be approximately equal to the average local value of p with the equality becoming exact in the limit $\Delta x, \Delta y \to 0$. This is achieved most simply by requiring that

$$\Pi^- + \Pi^+ = p_1 + p_2 \qquad (2.13)$$

which constrains the average of the pressures on each pair of opposing faces to be the same. Equation (2.13) is called the Π-equation. Although many other constraints between p and Π can be formulated, (2.13) is the simplest constraint which is also second order accurate. Also, it will ultimately produce the same number of unknowns as equations in the global equation set as shown by Giles [19].

One problem with the x and y-momentum equations (2.10-11) and the

Π-equation (2.13) is that they are transparent to the sawtooth grid oscillations shown in Figure 2.5.

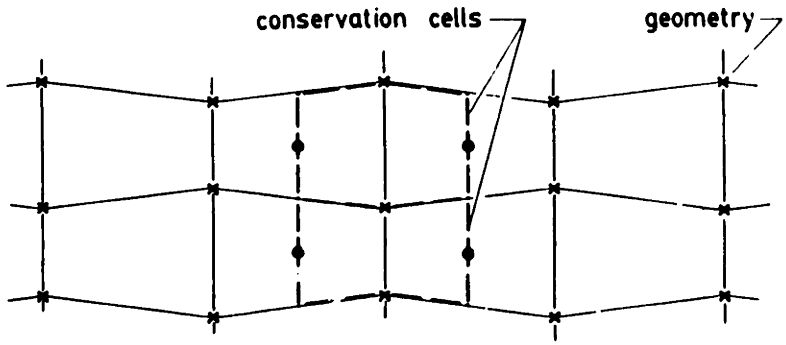

Figure 2.5 Grid sawtooth oscillations

These oscillations are neutrally stable, and normally are adequately inhibited by solid-wall boundary conditions. For inverse boundary conditions, however, it is desirable to eliminate them completely. One way to do this is to correct the average of the Π pressures for the sawtooth-induced streamtube area change in the middle of the cell. The Π-equation is therefore modified to

$$\Pi^- + \Pi^+ = p_1 + p_2 + 2P_c \tag{2.14}$$

A possible way to relate the pressure correction change P_c to the streamtube area change is to use the isentropic pressure-area relation $\Delta p/p \approx \gamma M^2/(1-M^2)\ \Delta A/A$. The corresponding discrete form for P_c (= Δp) in uniform flow would be

$$P_c \approx \frac{p}{A_c}\gamma M^2/(1-M^2)\left(A_c - \frac{1}{2}(A_{n_1}+A_{n_2})\right) \tag{2.15}$$

where A_c is related to the grid geometry as shown in Figure 2.6.

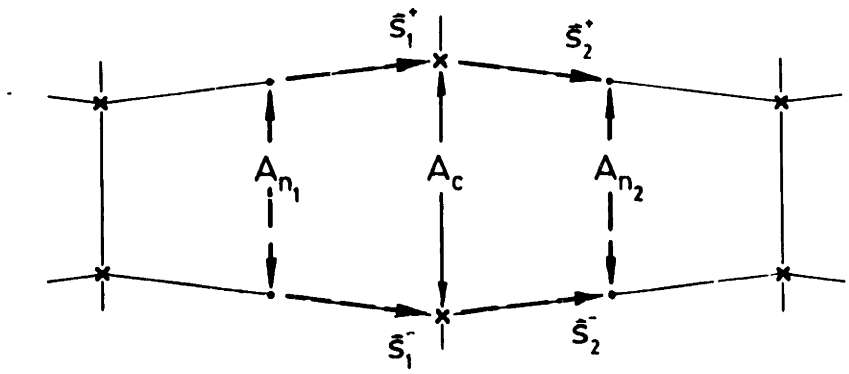

Figure 2.6 Quantities for isentropic Π correction

Using equation (2.15) to define P_c is not appropriate for several reasons. Numerical experiments revealed that the amount of pressure correction given by equation (2.15) is about an order of magnitude more than is necessary to prevent the grid sawtooth from appearing. Also, the pressure correction was found to cause instabilities in supersonic regions. A form for P_c which takes these considerations into account and is also applicable to non-uniform grids is

$$P_c = \begin{cases} k\,\gamma\,p\,M^2(1-M^2)\,\dfrac{|\vec{s}_1^-\times\vec{s}_2^-| - |\vec{s}_1^+\times\vec{s}_2^+|}{2\,|\vec{S}\times\vec{N}|} & , \quad M^2<1 \\ 0 & , \quad M^2>1 \end{cases} \tag{2.16}$$

where $\quad p = \frac{1}{2}(p_1 + p_2) \qquad M^2 = \frac{1}{2}(M_1^2 + M_2^2) \qquad (2.17a\text{-}b)$

The vectors $\vec{s}_1^-$, $\vec{s}_2^-$, $\vec{s}_1^+$, $\vec{s}_2^+$ are related to the local streamline geometry as shown in Figure 2.6. The factor k in (2.16) typically lies in the range $0.05 < k < 0.20$. With k=1 and uniform flow, the modified P_c definition (2.16) reduces to the isentropic pressure-area relation in the incompressible limit $M \ll 1$.

It is useful at this point to resolve the discrete x and y-momentum equations (2.10) and (2.11) into local streamwise and normal momen-

tum equations in the directions of $\vec{S}$ and $\vec{N}$, respectively. By taking S_x times equation (2.10) plus S_y times equation (2.11), and using the general Π equation (2.14), the S-momentum equation is obtained.

$$mq_1 f_1 - mq_2 f_2 + p_1 - p_2 + P_c \frac{|\vec{B}^- \times \vec{B}^+|}{|\vec{S} \times \vec{N}|} = 0 \qquad (2.18)$$

where $$f_1 = \frac{\hat{s}_1 \cdot \vec{S}}{|\vec{S} \times \vec{N}|} \quad , \quad f_2 = \frac{\hat{s}_2 \cdot \vec{S}}{|\vec{S} \times \vec{N}|} \qquad (2.19a\text{-}b)$$

Likewise, by taking N_x times equation (2.10) and N_y times equation (2.11), the N-momentum equation is obtained.

$$mq_1 g_1 - mq_2 g_2 + \Pi^- - \Pi^+ + P_c \frac{|\vec{A}_1 \times \vec{A}_2|}{|\vec{S} \times \vec{N}|} = 0 \qquad (2.20)$$

where $$g_1 = \frac{\hat{s}_1 \cdot \vec{N}}{|\vec{S} \times \vec{N}|} \quad , \quad g_2 = \frac{\hat{s}_2 \cdot \vec{N}}{|\vec{S} \times \vec{N}|} \qquad (2.21a\text{-}b)$$

In Drela, Giles and Thompkins [14], it is shown that equations (2.18) and (2.20) with $P_c=0$ reduce to the streamline curvature equations in the limit of infinite grid resolution, and hence are a consistent discretization of the Euler equations.

2.3 Artificial dissipation

In supersonic zones the discrete Euler equations are ill-posed without the addition of some form of artificial numerical dissipation, as is shown by the analysis in Appendix D. One way to make the equations well-posed is through the introduction of upwinded density (also termed "artificial compressibility") in the mass equation. This idea was first used by Eberle [16] for the transonic potential equation, and was later used by Wornom [57] for the quasi-one-dimensional Euler equations. Giles [19] successfully applied this form of artificial

dissipation to the the present Euler equation discretization to obtain stable transonic solutions. In this thesis, a form of artificial dissipation analogous to bulk viscosity will be used. Based on the stability analysis given in Appendix A, the S and N-momentum equations are modified to

$$m\bar{q}_1 f_1 - m\bar{q}_2 f_2 + p_1 - p_2 + P_c \frac{|\vec{B}^- \times \vec{B}^+|}{|\vec{S} \times \vec{N}|} = 0 \qquad (2.22)$$

$$m\bar{q}_1 g_1 - m\bar{q}_2 g_2 + \Pi^- - \Pi^+ + P_c \frac{|\vec{A}_1 \times \vec{A}_2|}{|\vec{S} \times \vec{N}|} = 0 \qquad (2.23)$$

where $\bar{q}_1$ and $\bar{q}_2$ are upwinded speeds defined by

$$\bar{q}_1 = q_1 - \lambda_1 (q_1 - q_0) \qquad (2.24a)$$

$$\bar{q}_2 = q_2 - \lambda_2 (q_2 - q_1) \qquad (2.24b)$$

The analysis in Appendix A suggests that a good definition for λ is

$$\lambda_2 = \max\left(0 , \frac{M^2 - M_c^2}{\gamma M^2}\right) , \qquad M^2 = \max(M_1^2, M_2^2) \qquad (2.25)$$

Thus, dissipation in the form of speed upwinding is introduced wherever the local cell maximum Mach number M exceeds the threshold value M_c. For numerical stability, M_c has to be somewhat less than unity, and is usually chosen to be approximately 0.99.

2.4 Π pressure elimination

To minimize the number of variables in the Newton solution method to be described in Chapter 4, it is necessary to eliminate the Π variables from the N-momentum equation (2.23). Π^+ is eliminated simply by adding the Π-equation (2.14) to the N-momentum equation (2.23), giving

$$m\bar{q}_1 g_1 - m\bar{q}_2 g_2 - p_1 - p_2 + P_c \frac{|\vec{A}_1 \times \vec{A}_2|}{|\vec{S} \times \vec{N}|} - 2P_c = -2\Pi^- \qquad (2.26)$$

Similarly, Π^- is eliminated by subtracting the Π-equation from the N-momentum equation, yielding

$$m\bar{q}_1 g_1 - m\bar{q}_2 g_2 + p_1 + p_2 + P_c \frac{|\vec{A}_1 \times \vec{A}_2|}{|\vec{S} \times \vec{N}|} + 2P_c = 2\Pi^+ \qquad (2.27)$$

To eliminate the Π variables from equations (2.26) and (2.27), we note that Π^- for streamtube j is in fact the same quantity as Π^+ for streamtube j-1 as shown in Figure 2.7.

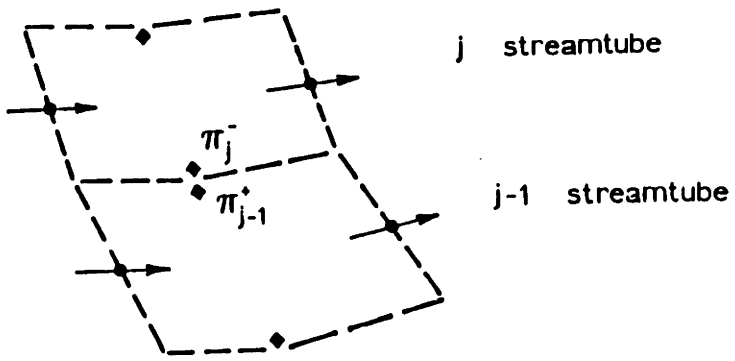

Figure 2.7 Π_j^- and Π_{j-1}^+ pressure equivalence

By adding equation (2.26) at i,j to equation (2.27) at i,j-1, the so-called reduced N-momentum equation results.

$$2\Pi^+_{i,j-1} - 2\Pi^-_{i,j} =$$

$$\left(m\bar{q}_1 g_1 - m\bar{q}_2 g_2 + p_1 + p_2 + P_c \frac{|\vec{A}_1 \times \vec{A}_2|}{|\vec{S} \times \vec{N}|} + 2P_c \right)_{j-1}$$

$$+ \left(m\bar{q}_1 g_1 - m\bar{q}_2 g_2 - p_1 - p_2 + P_c \frac{|\vec{A}_1 \times \vec{A}_2|}{|\vec{S} \times \vec{N}|} - 2P_c \right)_j = 0 \qquad (2.28)$$

Together with the S-momentum equation (2.22), the reduced N-momentum equation (2.28) is now ready to be tackled by the Newton solution algo-

rithm to be described in Chapter 4.

2.5 Streamtube inlet boundary condition

The analytic Euler equations require two thermodynamic variables to be specified at a subsonic inlet. One is already specified in the form of the stagnation enthalpy, which is in fact prescribed along the entire streamtube. The other thermodynamic quantity which is specified only at the inlet of each streamtube is the stagnation density,

$$\rho_t = \rho_1 \left(1 + \frac{\gamma-1}{2} M_1^2\right)^{1/(\gamma-1)} = \rho_1 \left(1 - \frac{1}{2h_t} q_1^2\right)^{-1/(\gamma-1)} \qquad (2.29)$$

where the subscript "1" now denotes the variables at the inlet face.

2.6 Global Variables and Equations

Every discrete equation and variable presented so far is associated with some particular node or location in the rectangular computational grid. However, for the airfoil and cascade problems which are addressed in this thesis, there are certain variables and equations which aren't associated with any particular node. These are termed "global" variables and equations. A few examples are cascade inlet and outlet flow slopes, airfoil circulation, and freestream flow angle of attack. Often, the equations which constrain these variables are obvious, such as a specified inlet flow slope or a specified freestream angle of attack. Other constraints are more subtle and must be obtained from physical insight. An example is the Kutta condition, which must be applied to the cascade and airfoil problems to fix the outlet flow slope and the circulation, respectively. Global variables and equations will be introduced and discussed as they arise for each problem category in the subsequent chapters.

3. DIRECT PROBLEM

This chapter will present the boundary conditions encountered in the solution of the direct, or analysis problem. In addition, certain global variables and constraints which arise in the direct problem will also be addressed. Treatment will be restricted to cascade and isolated airfoil geometries. The grid in each case is a logical rectangle with the indexing system shown in Figure 3.1.

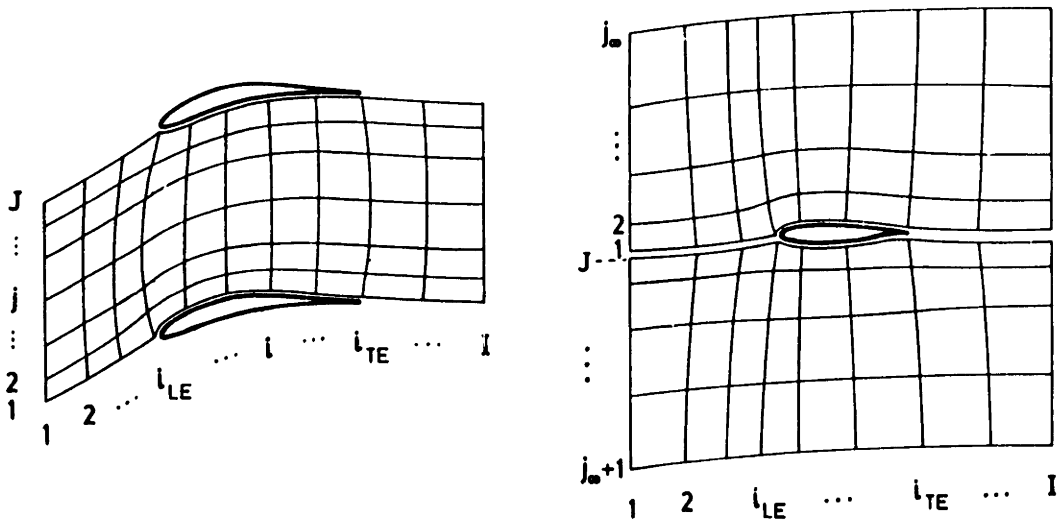

Figure 3.1 Grid indexing for cascade and isolated airfoil

Note that for the airfoil case, the streamline index j starts with the value of 1 at the airfoil suction surface, and then "wraps around" at j_∞ to end up with the value of J at the pressure surface. There is a dummy streamtube between the streamlines $j = j_\infty$ and $j = j_\infty+1$ where the governing equations will be replaced by the far field boundary conditions of a lifting airfoil.

3.1 Solid Wall Boundary Conditions

The wall boundary conditions which are required to close the entire system of equations for both cascades and airfoils are extremely simple. At a solid wall, the only physical boundary condition is that

the flow is tangent to the surface. In the discrete equations, this is implemented by requiring that each wall streamline lie on the wall itself, as shown in Figures 3.2 and 3.3.

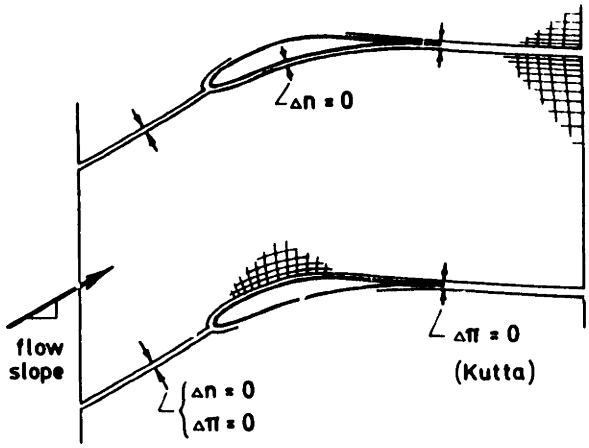

Figure 3.2 Cascade boundary conditions

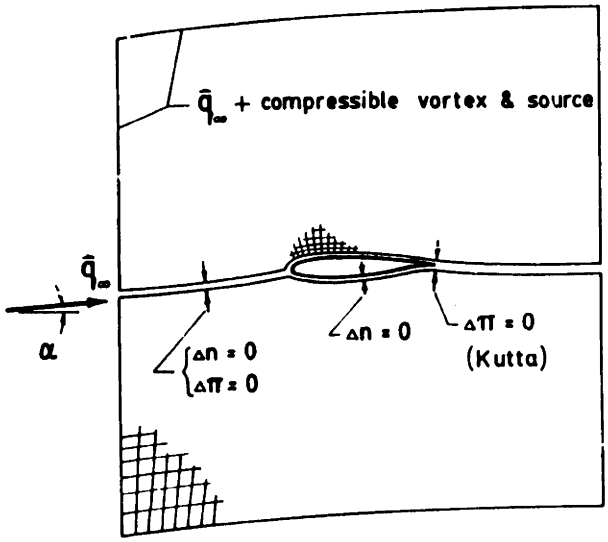

Figure 3.3 Isolated Airfoil boundary conditions

A local coordinate n in the direction perpendicular to the solid wall is defined at each node. As will be described in detail in Chapter 4, the grid nodes are restricted to move only along this normal coordinate, with the node spacing along the airfoil surface being prescribed. The solid wall boundary conditions are therefore

$$\Delta n_{i,1} = 0$$

$$\Delta n_{i,J} = 0 \qquad i_{LE} \leq i \leq i_{TE} \qquad (3.1a\text{-}b)$$

where Δn is the gap between the wall and the surface streamline as shown in Figures 3.2 and 3.3. These boundary conditions still allow the surface grid nodes to slide along the airfoil. Such sliding occurs in the case of a blunt leading edge, where the position of the stagnation point on the airfoil is a result of the calculation. This aspect of the direct problem will be treated later in this chapter. In Chapter 6, equations (3.1a-b) will be modified to account for the viscous displacement thickness. It is interesting to note that no other boundary conditions are required by the discrete Euler equation set. In particular, the wall Π pressures do not have to be extrapolated from the field interior, as in most time-marching Euler solvers, but are a result of the calculation.

On the part of each stagnation streamline which does not lie on the airfoil surface, two boundary conditions are required. One is a geometry continuity condition:

$$\Delta n_i = 0 \quad , \quad 2 \leq i \leq i_{LE}-1 \quad \text{and} \quad i_{TE}+1 \leq i \leq I-1 \qquad (3.2)$$

Here, Δn_i denotes the gap between streamlines j=1 and j=J as shown in Figure 3.2. The other boundary condition is a pressure continuity condition:

$$\Pi^{-}_{i,1} - \Pi^{+}_{i,J-1} = 0 \quad , \quad 2 \leq i \leq i_{LE}-1 \quad \text{and} \quad i_{TE}+1 \leq i \leq I-1 \qquad (3.3)$$

The Π pressures in equation (3.3) are easily related to the other local variables by using equations (2.26) and (2.27). All of the equations above are applied to both cascades and isolated airfoils. For the cascade case, equations (3.2) and (3.3) can be interpreted as periodicity conditions.

3.2 Cascade Far-field Boundary Conditions

In the cascade problem, the discrete Euler equation set requires geometric boundary conditions for the streamline endpoints, one at the inlet (i = 1) and one at the outlet (i = I). For consistency, these boundary conditions must allow the flow to become invariant along each streamtube far upstream and far downstream of the cascade. The simplest approach would be to set the vertical spacing between the streamline nodes such that the cross-sectional area of each streamtube is proportional to its mass flux. Unfortunately, this boundary condition would be incorrect if the entropy differed between streamtubes because of nonzero inlet vorticity or shock entropy generation. A boundary condition which is still valid for non-isentropic flows is to specify that all the streamline segments between the inlet plane (i=1) and the plane just inside (i=2) have a common slope S_{inl}. This is expressed as

$$\frac{y_{2,j} - y_{1,j}}{x_{2,j} - x_{1,j}} = S_{inl} \qquad , \quad 1 \leq j \leq J \qquad (3.4)$$

Likewise, the outlet streamlines are constrained to have the outlet slope S_{out}.

$$\frac{y_{I,j} - y_{I-1,j}}{x_{I,j} - x_{I-1,j}} = S_{out} \qquad , \quad 1 \leq j \leq J \qquad (3.5)$$

S_{inl} and S_{out} are two global variables which have been introduced into the equation set. To retain a closed system, two additional equations must be introduced to constrain them. An appropriate equation to constrain S_{inl} is to simply set it to some specified value:

$$S_{inl} - \left(S_{inl}\right)_{spec} = 0 \qquad (3.6)$$

At the outlet, a flow slope can be specified as well. However, this will in general produce a large pressure jump across the stagnation streamline at the sharp trailing edge. In the corresponding physical situation this cannot occur since vorticity will be shed until the pressure jump across the trailing edge is zero. This is a viscous mechanism which establishes the ciculation and hence the lift on any

airfoil-like body, and the zero-pressure jump is the well-known Kutta condition. With viscous Navier-Stokes solvers, and also with conventional Euler solvers which have numerical viscosity, the Kutta condition becomes satisfied automatically. In potential solvers, which have no dissipation, the Kutta condition must be set explicitly. Since the present streamtube Euler solver does not have any numerical viscosity in subsonic regions, it is necessary to explicitly impose the Kutta condition here as well.

$$\Pi^{-}_{i_{TE},1} - \Pi^{+}_{i_{TE},J-1} = 0 \tag{3.7}$$

Note that the Kutta condition (3.7) is in fact the same equation as the pressure-continuity boundary condition (3.3) which is applied to all the all the wake and and inlet stagnation streamline points. However, equation (3.7) is considered a global equation since it is used to constrain the global variable S_{out}, just like the global equation (3.6) constrains the global variable S_{inl}.

3.3 Airfoil Far-Field Boundary Conditions

As shown in Appendix B, the leading order behavior for the velocity potential Φ at a large distance from the airfoil is given by the superposition of a uniform flow, a vortex, a source, and the two components of a doublet. The potential of this combination is

$$\Phi = \beta\bar{x} - \frac{\Gamma}{2\pi}\Theta + \frac{\Sigma}{2\pi}\ln(\bar{r}) + \frac{D_x}{2\pi}\frac{\cos\Theta}{\bar{r}} + \frac{D_y}{2\pi}\frac{\sin\Theta}{\bar{r}} + \left(\frac{\Gamma M_\infty}{2\pi}\right)^2\left(E\frac{\ln(\bar{r})}{\bar{r}}\cos\Theta + F\frac{\cos 3\Theta}{\bar{r}}\right) \tag{3.8}$$

where

$$\bar{r} = \left(\bar{x}^2 + \bar{y}^2\right)^{\frac{1}{2}} \qquad \Theta = \arctan\frac{\bar{y}}{\bar{x}} \qquad \beta = \left(1-M_\infty^2\right)^{\frac{1}{2}} \tag{3.9a-c}$$

and

$$E = \frac{1}{4}\left(\frac{\gamma+1}{\beta^3} + \frac{3-\gamma}{\beta}\right) \qquad F = \frac{-1}{16}\left(\frac{\gamma+1}{\beta^3} + \frac{\gamma+1}{\beta}\right) \tag{3.9d-e}$$

Here, $\bar{x}$ and $\bar{y}$ are transformed coordinates aligned with the freestream. They are related to the physical coordinates x and y, the freestream angle of attack α, and to the freestream Mach number M_∞ by the following shift, rotation, and scaling transformation:

$$\bar{x} = \Big((x-x_o)\cos(\alpha) + (y-y_o)\sin(\alpha)\Big)\frac{1}{\beta} \qquad (3.10a)$$

$$\bar{y} = -(x-x_o)\sin(\alpha) + (y-y_o)\cos(\alpha) \qquad (3.10b)$$

x_o and y_o are the physical coordinates of the point where the far field vortex, source, and doublet are centered. This point is usually taken to be on the airfoil chord line at the 25% chord position.

The velocity potential Φ in equation (3.8) is used to determine the static pressure which is imposed as a boundary condition along the top and bottom streamlines ($j = j_\infty,\ j_\infty+1$).

$$\Pi^+_{i,j_\infty-1} = p_t\left(1 - \frac{q_\infty^2}{2h_t}\left(\phi_x^2 + \phi_y^2\right)_{i,j_\infty}\right)^{\frac{\gamma}{\gamma-1}}, \quad 2 \le i \le I-1 \qquad (3.11a)$$

$$\Pi^-_{i,j_\infty+1} = p_t\left(1 - \frac{q_\infty^2}{2h_t}\left(\phi_x^2 + \phi_y^2\right)_{i,j_\infty+1}\right)^{\frac{\gamma}{\gamma-1}}, \quad 2 \le i \le I-1 \qquad (3.11b)$$

The Cartesian velocity components Φ_x and Φ_y in (3.11a-b) are given by

$$(\Phi_x)_{i,j} = \frac{\cos\alpha}{\beta}(\Phi_{\bar{x}})_{i,j} - \sin\alpha\,(\Phi_{\bar{y}})_{i,j} \qquad (3.12a)$$

$$(\Phi_y)_{i,j} = \frac{\sin\alpha}{\beta}(\Phi_{\bar{x}})_{i,j} + \cos\alpha\,(\Phi_{\bar{y}})_{i,j} \qquad (3.12b)$$

where the transformed velocity components $\Phi_{\bar{x}}$ and $\Phi_{\bar{y}}$ are obtained by differentiation of the Φ definition (3.8). The resulting expressions are rather tedious and are best obtained from the code listing.

Three new global unknowns have been introduced into the system by using equations (3.11a-b) as far-field boundary conditions: the angle of attack α, far-field circulation Γ, and far-field source strength Σ. Therefore, three new constraints must be introduced. The appropriate

constraint on Γ is the Kutta condition that was used to fix the outlet slope (and hence the circulation) in the cascade case.

$$\Pi^{-}_{i_{TE},1} - \Pi^{+}_{i_{TE},J-1} = 0 \tag{3.7}$$

To constrain the angle of attack, two approaches are possible. One is to simply specify the angle of attack.

$$\alpha - \alpha_{spec} = 0 \tag{3.13}$$

The other approach is to specify the lift, which in turn is related to the integrated pressure loads over the airfoil surface.

$$L_{spec} = \frac{\beta}{2} \sum_{i=i_{LE}}^{i_{TE}} (\bar{x}_{i+1,J} - \bar{x}_{i-1,J})\, \Pi^{+}_{i,J-1} - (\bar{x}_{i+1,1} - \bar{x}_{i-1,1})\, \Pi^{-}_{i,1} \tag{3.14}$$

Thus, either the lift or the angle of attack can be specified. The quantity which is not specified is then a result of the calculation. It is worthwhile to mention here that in shock-free flows, the quantity $\rho_\infty q_\infty \Gamma$ always equals the lift obtained from surface pressure integration to within a small truncation error. This is viewed as evidence of the consitency of the present discretization scheme.

The far-field source strength Σ, which is only present in shocked flows and/or in flows with boundary layer coupling, is related directly to the stagnation pressure and displacement thickness at the outlet as shown in Appendix B.

$$\Sigma = \delta^{*}_{outlet} + \sum_{j=1}^{J-1} \left(\frac{1}{(\rho u)_{+\infty_j}} - \frac{1}{\rho_\infty u_\infty} \right) m_j \tag{3.15}$$

where

$$(\rho u)_{+\infty_j} = (2h_t)^{\frac{1}{2}} \left[1 - \left(\frac{p_\infty}{p_t} \right)_j^{\frac{\gamma-1}{\gamma}} \right]^{\frac{1}{2}} \frac{\gamma}{\gamma-1} \frac{p_\infty}{h_t} \left(\frac{p_t}{p_\infty} \right)_j^{\frac{\gamma-1}{\gamma}} \tag{3.16}$$

The two doublet strengths D_x and D_y are determined by two minimization conditions as described in Appendix B. In discrete form, these

conditions are

$$\sum_{j=j_\infty}^{j_\infty+1} \sum_{i=1}^{I-1} \left(\Phi_x \Delta y - \Phi_y \Delta x\right)_{i+\frac{1}{2},j} \left(\frac{\partial \Phi_x}{\partial D_x} \Delta y - \frac{\partial \Phi_y}{\partial D_x} \Delta x\right)_{i+\frac{1}{2},j} = 0 \qquad (3.17)$$

$$\sum_{j=j_\infty}^{j_\infty+1} \sum_{i=1}^{I-1} \left(\Phi_x \Delta y - \Phi_y \Delta x\right)_{i+\frac{1}{2},j} \left(\frac{\partial \Phi_x}{\partial D_y} \Delta y - \frac{\partial \Phi_y}{\partial D_y} \Delta x\right)_{i+\frac{1}{2},j} = 0 \qquad (3.18)$$

Here, Δx and Δy imply

$$\Delta x = x_{i+1,j} - x_{i,j} \qquad \Delta y = y_{i+1,j} - y_{i,j}$$

and Φ_x, Φ_y, $\partial \Phi_x / \partial D_x$, etc., are evaluated at the midpoint coordinates

$$x_{i+\frac{1}{2},j} = \frac{x_{i+1,j} + x_{i,j}}{2} \quad , \quad y_{i+\frac{1}{2},j} = \frac{y_{i+1,j} + y_{i,j}}{2}$$

The validity of the doublet constraints (3.17) and (3.18) has been confirmed by cases where the exact doublet strength is known, such as in the case of the incompressible flow around a circular cylinder or a very thin airfoil. In general, the calculated doublet strength equals the exact value to within a few percent.

At the inlet and outlet planes, the airfoil case requires the same geometric boundary conditions as the cascade case. The setting of a uniform slope at the inlet and outlet of a cascade flowfield is justified on the grounds that the periodic pressure disturbances due to the individual cascade airfoils decay exponentially upstream and downstream of the cascade as shown by Giles [19]. Setting all the streamlines to be parallel is inappropriate for the airfoil case, however, because of the relatively slow $1/r$ and $1/r^2$ type of decay of the far-field vortex, source, and doublet velocity field. This slow decay causes the streamline direction to vary significantly across the inlet and outlet boundaries of a reasonably sized domain. Therefore, it is better to let the prescribed streamline slope vary according to the streamline pattern of a uniform flow with a superimposed compressible vortex, source, and doublet. Hence, at the inlet and oulet boundaries, each

streamline segment is constrained to be parallel to the local velocity whose components Φ_x and Φ_y are given by equations (3.12a-b). At the inlet, this is expressed by the following cross-product:

$$\left(x_{1,j} - x_{2,j}\right)\left(\left(\Phi_y\right)_{1,j} + \left(\Phi_y\right)_{2,j}\right) -$$

$$\left(y_{1,j} - y_{2,j}\right)\left(\left(\Phi_x\right)_{1,j} + \left(\Phi_x\right)_{2,j}\right) = 0 \quad , \quad 1 \leq j \leq J \qquad (3.19)$$

At the outlet plane, the corresponding condition is:

$$\left(x_{I-1,j} - x_{I,j}\right)\left(\left(\Phi_y\right)_{I-1,j} + \left(\Phi_y\right)_{I,j}\right) -$$

$$\left(y_{I-1,j} - y_{I,j}\right)\left(\left(\Phi_x\right)_{I-1,j} + \left(\Phi_x\right)_{I,j}\right) = 0 \quad , \quad 1 \leq j \leq J \qquad (3.20)$$

3.4 Blunt leading edge treatment

A body with a blunt leading edge requires special treatment at the stagnation point if a physically realistic solution is to be obtained. In particular, the position of the stagnation point on the airfoil cannot be assumed a priori, but clearly must be a result of the solution. Therefore, the stagnation point grid node (at $i=i_{LE}$ and $j=1,J$) must be free to slide on the airfoil surface. To prevent grid cross-overs, the other surface grid nodes must also slide in a way which maintains a good grid distribution. In the present formulation, the relative spacings between grid nodes on the suction side are kept proportional to the total suction side arc length between the stagnation point and the trailing edge. The same is done for the pressure side. Hence, as the stagnation point slides on the surface, the other nodes on and near the surface also slide proportionally in an accordion-like fashion, as illustrated in Figure 3.4.

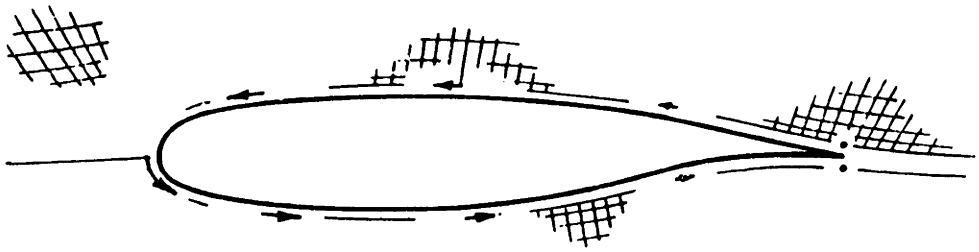

Figure 3.4 Surface node movement tied to stagnation point movement

The movement of the surface nodes does not modify any of the governing equations or boundary conditions presented so far. The only consequence will arise in the Newton solution procedure to be described in Chapter 4. In effect, the position of each surface node is now dependent on the new global variable s_{LE}, which the position of the stagnation point grid node on the airfoil in terms of arc length measured counterclockwise around the airfoil from trailing edge to trailing edge. The appropriate global equation to constrain s_{LE} is a zero pressure jump across the stagnation streamline at the stagnation point, or in other words a leading edge Kutta condition.

$$\Pi^{-}_{i_{LE},1} - \Pi^{+}_{i_{LE},J-1} = 0 \qquad (3.21)$$

In cases involving a sharp leading edge, the stagnation point is assumed to be fixed at the leading edge, and the global variable s_{LE} does not exist. Because the global equation (3.21) can no longer be enforced, a pressure jump across the leading edge will generally result. According to incompressible potential theory, this pressure jump should be infinite. Given the finite available grid resolution in the present scheme, however, the resulting pressure jump will be merely large.

* * *

Together with the solid wall, periodicity, and far-field boundary conditions presented in this chapter, and with the interior equations presented in Chapter 2, the entire equation set for the direct problem is complete. The Newton solution procedure for the equations is presented next in Chapter 4.

4. SOLUTION PROCEDURE

Chapters 2 and 3 have presented all the steady state equations obtained from the discretization of the Euler equations, and their associated boundary conditions for the direct problem. This chapter will describe the Newton method which is used to solve this system of nonlinear equations. The modifications to the method necessary for solution of the inverse and boundary layer coupling problems will be presented as they arise in subsequent chapters.

4.1 The Newton method

The Newton method is a well-established algorithm for solving nonlinear scalar or vector equations. For a scalar nonlinear equation of the form

$$f(u) = 0 \tag{4.1}$$

the Newton solution procedure at some iteration level ν is

$$f(u^{\nu+1}) \equiv f(u^{\nu}+\delta u^{\nu}) \simeq f(u^{\nu}) + f'(u^{\nu})\,\delta u^{\nu} = 0 \tag{4.2a}$$

$$\delta u^{\nu} = - f(u^{\nu}) / f'(u^{\nu}) \tag{4.2b}$$

$$u^{\nu+1} = u^{\nu} + \delta u^{\nu} \tag{4.2c}$$

This procedure converges quadratically (i.e. $\delta u^{\nu+1} \sim (\delta u^{\nu})^2$) provided the current solution u^{ν} is sufficiently close to the exact solution. For a vector of equations $\mathbf{F}$ and a vector of unknowns $\mathbf{U}$, the Newton procedure is essentially the same.

$$\mathbf{F}(\mathbf{U}) = 0 \tag{4.3}$$

$$\mathbf{F}(\mathbf{U}^{\nu+1}) \equiv \mathbf{F}(\mathbf{U}^{\nu}+\delta\mathbf{U}^{\nu}) \simeq \mathbf{F}(\mathbf{U}^{\nu}) + \left[\frac{\partial \mathbf{F}}{\partial \mathbf{U}}\right]^{\nu} \delta\mathbf{U}^{\nu} = 0 \tag{4.4a}$$

$$\delta\mathbf{U}^{\nu} = -\left[\frac{\partial \mathbf{F}}{\partial \mathbf{U}}\right]^{-1\,\nu} \mathbf{F}(\mathbf{U}^{\nu}) \tag{4.4b}$$

$$\mathbf{U}^{\nu+1} = \mathbf{U}^{\nu} + \delta\mathbf{U}^{\nu} \qquad (4.4c)$$

The expression $[\partial\mathbf{F}/\partial\mathbf{U}]^{\nu}$ in equations (4.4a) and (4.4b) is the Jacobian matrix whose (i,j) entry is the partial derivative of the i'th equation in $\mathbf{F}$ with respect to the j'th variable in $\mathbf{U}$, evaluated at $\mathbf{U}^{\nu}$. The convergence for the vector equation is quadratic for a sufficiently accurate $\mathbf{U}^{\nu}$, just as in the scalar case. The primary difficulty with the vector equation is that a linear system of equations (4.4b) must be solved at each iteration, unlike the corresponding scalar equation (4.2b) which merely requires a single division. The Jacobian matrix which arises from the linearization of all the discrete Euler and boundary layer equations for the cases presented in this thesis can be as large as 9000 × 9000. However, it is an extremely sparse and highly structured matrix of bandwidth 69, and thus can be solved economically by Gaussian block elimination.

An alternative approach to solving equation (4.4b) at each iteration is to use some sort of iterative relaxation algorithm. Jespersen [27] has tried this solution approach with a conventional finite-volume discretization. He considered the linear system to be too large to be solved efficiently by direct methods, probably because his discretization required four unknowns per node in contrast to the two unknowns per node required by the streamtube formulation. Jesperson's approach was to solve the linear Newton equations by an iterative Gauss-Seidel method accelerated using multigrid, a technique developed by Brandt [4] for solving elliptic equations. His results showed no particular speed advantage over conventional time-marching. Giles [19] has formulated and tested an iterative solver for equation (4.4b) which required a preconditioner and was limited to subsonic flow. His results showed that even for the finest grids which might be used for typical engineering calculations, the Gaussian elimination solver was faster, more robust and simpler than the iterative solver, and also handled transonic flows without difficulty. Needless to say, further

efforts at iterative solution were dropped.

4.2 Newton linearization

In the present application the vector of functions **F** in equations (4.3-4) includes all of the discrete Euler equations, boundary conditions, global constraints, and boundary layer equations. To minimize the computational cost of solving equation (4.4b) it is desirable to use the smallest possible number of unknowns in the vector $\delta\mathbf{U}$. To achieve this, each grid node will be restricted to move perpendicular to the local streamline, so that the node position changes δx and δy can be replaced the single change δn. Here, n is a local coordinate perpendicular to the streamline passing through that node. To further reduce the number of unknowns, the linearized inviscid equations must be manipulated so that only the density and streamline position changes $\delta\rho$ and δn are left as independent variables. There are two basic approaches to this task. To clarify their differences, they will first be presented in a simplified, symbolic form. The much simpler approach, which is the one used in the program, will then be applied to the discrete equation set.

The first and perhaps most obvious approach is to explicitly express the discrete equations in terms of only ρ and n, and then differentiate. For instance, the S-momentum equation (2.22) has the form

$$F(S,N,s,q,p) = 0 \qquad (4.5)$$

where

$$S = S(x(n),\ y(n)) \qquad N = N(x(n),\ y(n)) \qquad s = s(x(n),\ y(n)) \qquad (4.6a\text{-}c)$$

and $$q = q(\rho,A) \qquad p = p(\rho,q) \qquad A = A(x(n),y(n)) \qquad (4.6d\text{-}f)$$

Node indices, subscripts, and other ornaments have been suppressed for the sake of clarity. The functional dependencies $q(\rho,A)$ and $p(\rho,q)$ are obtained from the mass and energy equations (2.9) and (2.12). In principle, equation (4.5) can be expressed explicitly in terms of ρ and n by fully expanding the functional dependencies $S(x,y)$, $x(n)$, $y(n)$,

$q(\rho,A)$, etc., and then linearized by differentiation with respect to ρ and n:

$$F(\rho,n) = 0 \tag{4.7}$$

$$\delta F(\rho,n) \simeq \frac{\partial F}{\partial \rho}\,\delta\rho + \frac{\partial F}{\partial n}\,\delta n \tag{4.8}$$

The difficulty with this approach is that $F(\rho,n)$ is an absurdly complicated expression and $\partial F/\partial\rho$ and $\partial F/\partial n$ are much worse. Coding them for the necessary evaluation at each iteration level would be rather impractical.

The second, simpler approach is to break down the differentiation in equation (4.6b) into a sequence of much simpler steps by invoking the chain rule, and then assembling the individual steps at the Fortran level. This process is illustrated in the following example. First, the expressions for x and y are linearized. As mentioned previously, each grid node is constrained to move in the direction of the unit vector $\hat{\mathbf{n}}$ perpendicular to the streamline, and hence the changes δx and δy are simply given by

$$\delta x = \frac{\partial x}{\partial n}\,\delta n = n_x\,\delta n \qquad\qquad \delta y = \frac{\partial y}{\partial n}\,\delta n = n_y\,\delta n \tag{4.9a-b}$$

Since $\hat{\mathbf{n}}$ is prescribed before each iteration, its components n_x and n_y are known constants. Next, the changes in S, N, s, A are obtained by straightforward chain-rule differentiation of their definitions.

$$\delta S \simeq \frac{\partial S}{\partial x}\,\delta x + \frac{\partial S}{\partial y}\,\delta y \qquad\qquad \delta N \simeq \frac{\partial N}{\partial x}\,\delta x + \frac{\partial N}{\partial y}\,\delta y \tag{4.10a-b}$$

$$\delta s \simeq \frac{\partial s}{\partial x}\,\delta x + \frac{\partial s}{\partial y}\,\delta y \qquad\qquad \delta A \simeq \frac{\partial A}{\partial x}\,\delta x + \frac{\partial A}{\partial y}\,\delta y \tag{4.11a-b}$$

Derivatives with respect to x and y such as $\partial S/\partial x$ and $\partial N/\partial y$, which are relatively simple expressions, are readily evaluated at the current iteration level and stored. For the current iteration, they thus become constants which trivially relate δS, δN, δs, δA and the independent variables δx and δy.

Next, the change δq is expressed in the same manner as δA was. The definition $q(\rho,A)$ is obtained from the mass equation (2.9) and is differentiated to give

$$\delta q \simeq \frac{\partial q}{\partial \rho}\,\delta\rho + \frac{\partial q}{\partial A}\,\delta A \tag{4.12}$$

The derivatives $\partial q/\partial\rho$ and $\partial q/\partial A$ are very simple expressions which are evaluated at the current iteration level and stored. Likewise, the expression for the change δp is obtained by differentiation of its definition $p(\rho,q)$ derived from the energy equation (2.12).

$$\delta p \simeq \frac{\partial p}{\partial \rho}\,\delta\rho + \frac{\partial p}{\partial q}\,\partial q \tag{4.13}$$

Again, the simple expressions $\partial p/\partial\rho$ and $\partial p/\partial q$ are evaluated and stored.

Now that all the intermediate expressions such as $q(\rho,A)$ and $p(\rho,q)$ have been linearized, the next step is to linearize $F(S,N,s,q,p)$ itself.

$$\delta F \simeq \frac{\partial F}{\partial S}\,\delta S + \frac{\partial F}{\partial N}\,\delta N + \frac{\partial F}{\partial s}\,\delta s + \frac{\partial F}{\partial q}\,\delta q + \frac{\partial F}{\partial p}\,\delta p \tag{4.14}$$

The derivatives in equation (4.14), which again are relatively simple expressions, are evaluated and stored as usual. The final step is to use equations (4.9) through (4.13) to express the changes δS, δN, δs, δq, δp in equation (4.14) in terms of only the independent variables $\delta\rho$ and δn. By direct substitution,

$$\begin{aligned}
\delta F \simeq\ & \left(\frac{\partial F}{\partial q}\frac{\partial q}{\partial \rho} + \frac{\partial F}{\partial p}\frac{\partial p}{\partial \rho}\right)\delta\rho \\
& + \left(\left(\frac{\partial F}{\partial N}\frac{\partial N}{\partial x} + \frac{\partial F}{\partial S}\frac{\partial S}{\partial x} + \frac{\partial F}{\partial s}\frac{\partial s}{\partial x} + \frac{\partial F}{\partial q}\frac{\partial q}{\partial A}\frac{\partial A}{\partial x} + \frac{\partial F}{\partial p}\frac{\partial p}{\partial q}\frac{\partial q}{\partial A}\frac{\partial A}{\partial x}\right)\frac{\partial x}{\partial n} \right. \\
& \left. + \left(\frac{\partial F}{\partial N}\frac{\partial N}{\partial y} + \frac{\partial F}{\partial S}\frac{\partial S}{\partial y} + \frac{\partial F}{\partial s}\frac{\partial s}{\partial y} + \frac{\partial F}{\partial q}\frac{\partial q}{\partial A}\frac{\partial A}{\partial y} + \frac{\partial F}{\partial p}\frac{\partial p}{\partial q}\frac{\partial q}{\partial A}\frac{\partial A}{\partial y}\right)\frac{\partial y}{\partial n} \right)\delta n
\end{aligned} \tag{4.15}$$

Since all the derivatives have already been calculated and stored, this final step is trivially done at the Fortran level.

Using the chain rule to break down the linearization process as

illustrated above is clearly the preferred linearization method, for reasons of both clarity and efficiency. This linearization method will now be applied to all the governing Euler equations and direct problem boundary conditions.

4.3 Jacobian structure

Before the linearized equations are derived, it is helpful to visualize the zone of dependence, or "molecule" of each discrete equation. For an I×J grid, there are (I-2)×(J-1) S-momentum equations (2.22) and (I-2)×(J-2) reduced N-momentum equations (2.28) to be solved. The molecule of each of these equations is shown in Figure 4.1. Other equations, such as airfoil far field boundary conditions involve global variables such as $\delta\Gamma$ and/or $\delta\alpha$.

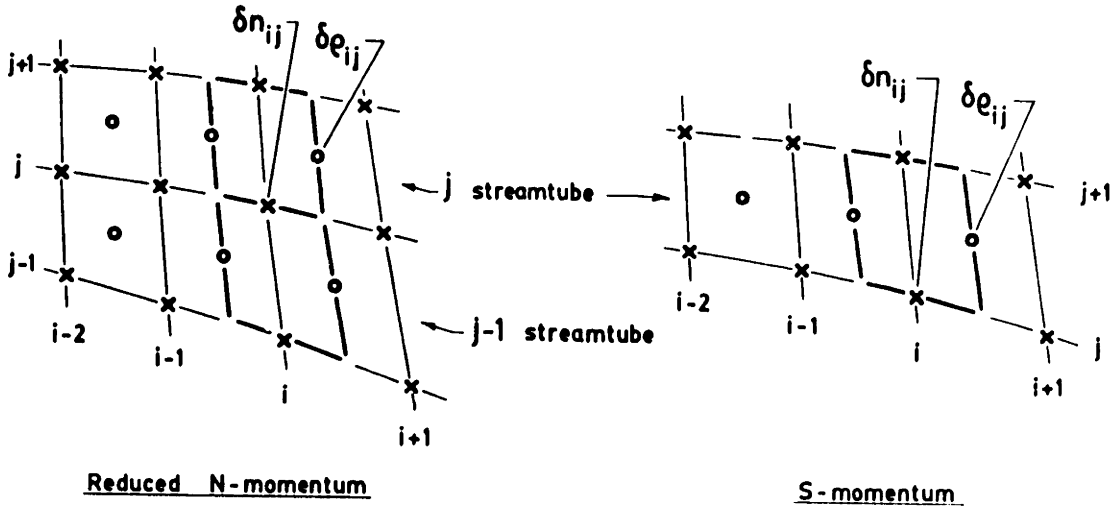

Figure 4.1 Zones of dependence of discrete Euler equations

When Newton's method is applied to these discrete equations, the linear system which results involves a block matrix with four block diagonals, plus a separate block column for the global variable entries and separate block row for the global equations. The structure of this linear Newton system is shown below.

$$
\begin{bmatrix}
\bar{\bar{A}}_1 & \bar{\bar{C}}_1 & & & & & & & \vdots & \bar{\bar{U}}_1 \\
\bar{\bar{B}}_2 & \bar{\bar{A}}_2 & \bar{\bar{C}}_2 & & & & & & \vdots & \bar{\bar{U}}_2 \\
\bar{\bar{Z}}_3 & \bar{\bar{B}}_3 & \bar{\bar{A}}_3 & \bar{\bar{C}}_3 & & & & & \vdots & \bar{\bar{U}}_3 \\
 & \cdot & \cdot & \cdot & \cdot & & & & \vdots & \cdot \\
 & & \bar{\bar{Z}}_i & \bar{\bar{B}}_i & \bar{\bar{A}}_i & \bar{\bar{C}}_i & & & \vdots & \bar{\bar{U}}_i \\
 & & & \cdot & \cdot & \cdot & \cdot & & \vdots & \cdot \\
 & & & & \bar{\bar{Z}} & \bar{\bar{B}} & \bar{\bar{A}} & \bar{\bar{C}} & \vdots & \bar{\bar{U}} \\
 & & & & & \bar{\bar{Z}} & \bar{\bar{B}} & \bar{\bar{A}} & \vdots & \bar{\bar{U}} \\
 & & & & & & \bar{\bar{Z}}_I & \bar{\bar{B}}_I & \bar{\bar{A}}_I & \vdots & \bar{\bar{U}}_I \\
\bar{\bar{G}}_1 & \bar{\bar{G}}_2 & \bar{\bar{G}}_3 & \cdot & \bar{\bar{G}}_i & \cdot & \cdot & \cdot & \bar{\bar{G}}_I & \vdots & \bar{\bar{G}}_g
\end{bmatrix}
\times
\begin{bmatrix} \bar{\delta}_1 \\ \bar{\delta}_2 \\ \bar{\delta}_3 \\ \cdot \\ \bar{\delta}_i \\ \cdot \\ \bar{\delta} \\ \bar{\delta} \\ \bar{\delta}_I \\ \bar{\Delta}_g \end{bmatrix}
=
\begin{bmatrix} \bar{R}_1 \\ \bar{R}_2 \\ \bar{R}_3 \\ \cdot \\ \bar{R}_i \\ \cdot \\ \bar{R} \\ \bar{R} \\ \bar{R}_I \\ \bar{R}_g \end{bmatrix}
\qquad (4.16)
$$

Here, $\bar{\delta}_i$ denotes the vector of the unknowns δn and $\delta\rho$ at streamwise station i, and $\bar{\Delta}_g$ denotes the vector of global unknowns such as $\delta\Gamma$ and $\delta\alpha$ which are not associated with individual nodes. The vector $\bar{R}_i$ contains the negated residuals of the S-momentum and reduced N-momentum equations and boundary conditions for streamwise station i, evaluated at the current solution. The vector $\bar{R}_g$ contains negated global equation (such as the Kutta condition or prescribed-lift condition) residuals evaluated at the current solution. All the block elements making up the large Jacobian coefficient matrix in (4.16) contain the derivatives of the residuals on the righthand side, again evaluated at the current solution. The block matrices $\bar{\bar{Z}}_i$, $\bar{\bar{B}}_i$, $\bar{\bar{A}}_i$, $\bar{\bar{C}}_i$, contain the corresponding Jacobian entries for δn and $\delta\rho$ (i.e. the residual derivatives with respect to n and ρ), and the $\bar{\bar{U}}_i$ block contains the Jacobian entries for global unknowns such as $\delta\Gamma$ and $\delta\alpha$ which typically appear in the boundary conditions. The $\bar{\bar{G}}_i$ blocks contain the global equation Jacobian entries for δn and $\delta\rho$, and the $\bar{\bar{G}}_g$ block contains the global equation entries for the global variables.

The structure of each block line in (4.16) reflects the molecules of the individual S-momentum, reduced N-momentum, and boundary condition equations. Figure 4.2 shows how the individual molecule nodes are divided between the $\bar{\bar{Z}}_i$, $\bar{\bar{B}}_i$, $\bar{\bar{A}}_i$, and $\bar{\bar{C}}_i$ blocks.

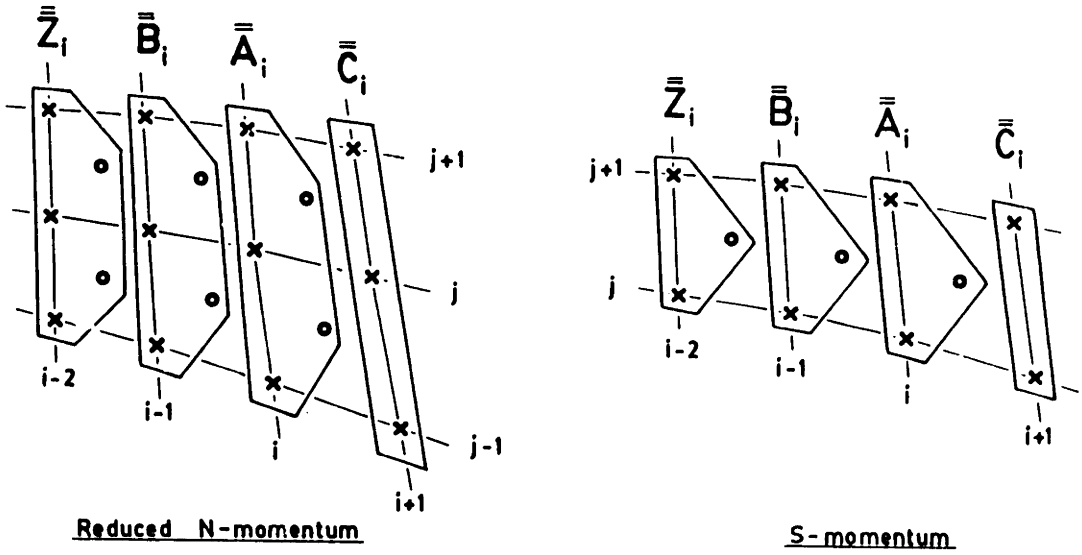

Figure 4.2 Division of variables between Jacobian matrix blocks

The linearized reduced N-momentum equations and periodicity boundary conditions are grouped in the top half of each block line, and the linearized S-momentum equations are grouped in the bottom half. This produces the block structure shown in Figures 4.3 and 4.4. The δn entries are denoted by $\times$, and the $\delta\rho$ entries are denoted by o.

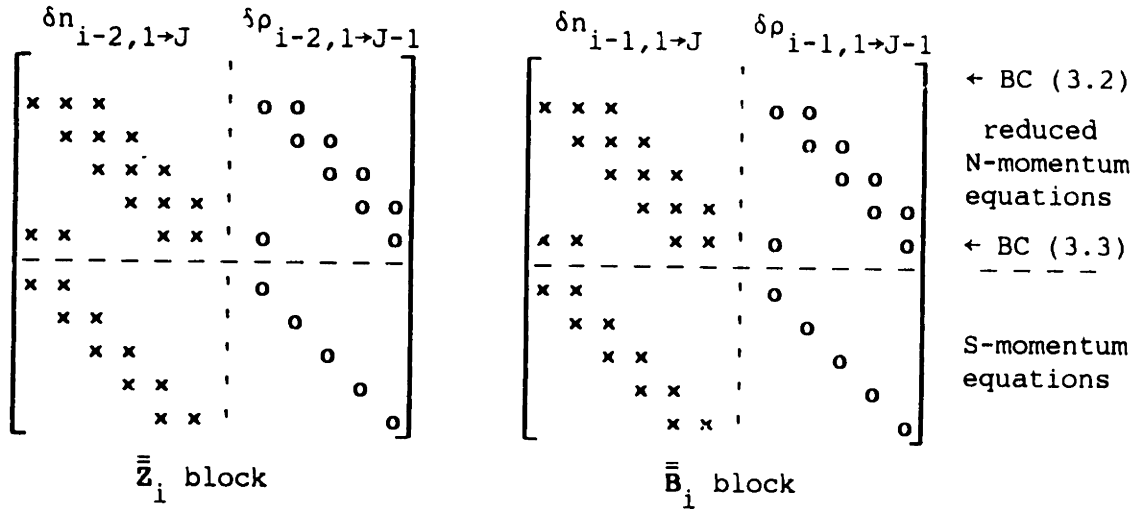

Figure 4.3 $\bar{\bar{Z}}_i$ and $\bar{\bar{B}}_i$ block structure ($2 \leq i \leq I-1$)

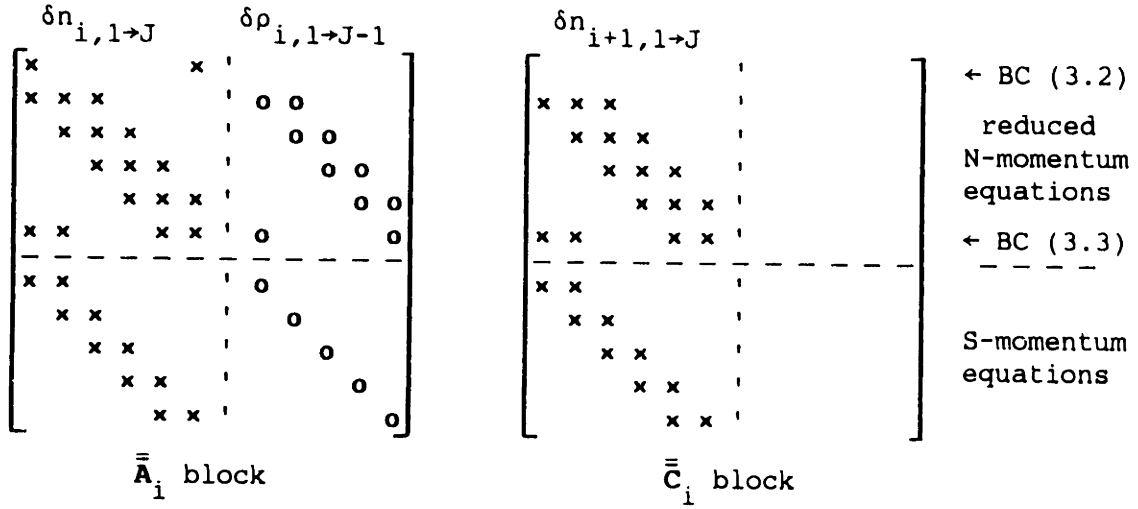

Figure 4.4 $\bar{\bar{A}}_i$ and $\bar{\bar{C}}_i$ block structure ($2 \leq i \leq I-1$)

Note that the row containing the linearized geometry continuity boundary condition (3.2) is empty except for the two δn entries in the $\bar{\bar{A}}_i$ block. The row containing the linearized pressure continuity boundary condition (3.3) has extra entries since equation (3.3) spans cells in the 1'st and J-1'th streamtubes. At a streamwise station where the 1'st and J-1'th streamtubes adjoin a solid surface, such as in a cas-

cade passage or at an airfoil surface location, the fixed-streamline boundary conditions (3.1a) and (3.1b) replace geometry and pressure continuity conditions. This will result in the rows labeled "BC (3.2)" and "BC (3.3)" in Figures 4.3 and 4.4 above to be totally devoid of entries except for one on the main diagonal of the $\bar{\bar{\mathbf{A}}}_i$ block.

The block structure shown in Figures 4.3 and 4.4 is misleading for an isolated airfoil case, since it does not indicate the far-field boundary conditions for an airfoil. In the isolated airfoil case, the j_∞'th and j_∞+1'th lines of each block do not contain the reduced N-momentum equations, but the linearized far field conditions (3.11a) and (3.11b) instead. These conditions will still result in the j_∞'th and j_∞+1'th lines having the same form as the reduced N-momentum equation.

At the inlet and outlet planes, which correspond to the first and last block rows of the Newton system (4.16), the block structure is also different from that shown in Figures 4.3 and 4.4.

<u>At the inlet</u> (i=1), the $\bar{\bar{\mathbf{Z}}}_i$ and $\bar{\bar{\mathbf{B}}}_i$ blocks do not exist. The upper halves of the $\bar{\bar{\mathbf{A}}}_i$ and $\bar{\bar{\mathbf{C}}}_i$ blocks contain either the linearized inlet slope conditions (3.6) for the cascade case, or the linearized flow angle conditions (3.19) for the airfoil case. The lower halves of the $\bar{\bar{\mathbf{A}}}_i$ and $\bar{\bar{\mathbf{C}}}_i$ blocks contain the linearized inlet stagnation density condition (2.29). Figure 4.5 shows this block structure.

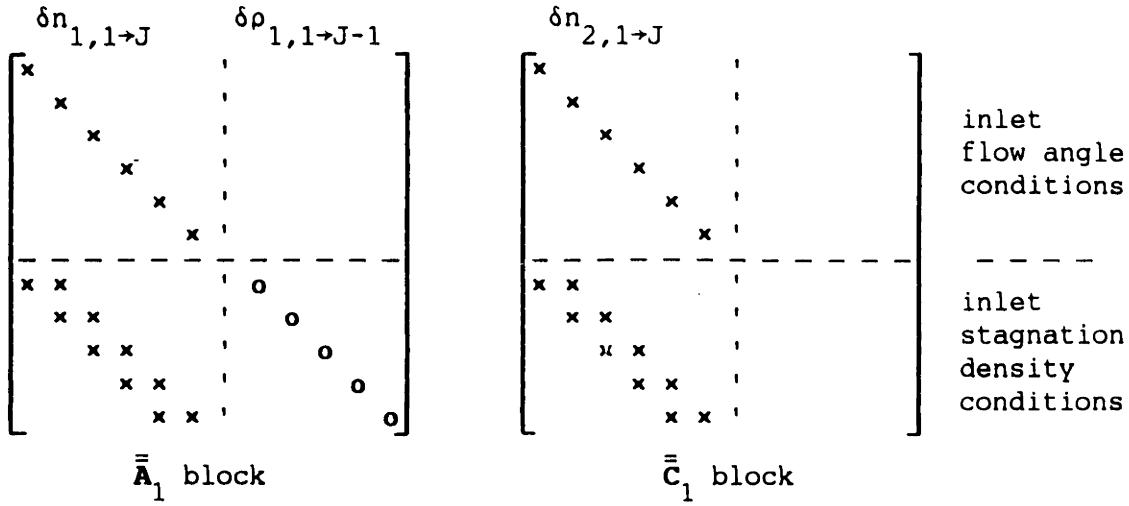

Figure 4.5 $\bar{\bar{A}}_1$ and $\bar{\bar{C}}_1$ block structure

At the outlet (i=I), the $\bar{\bar{C}}_i$ block does not exist. The $\bar{\bar{Z}}_i$ block is usually all zeroes, although it doesn't have to be. The upper halves of of the $\bar{\bar{B}}_i$ and $\bar{\bar{A}}_i$ blocks contain the same flow angle conditions as at the inlet. The lower halves of the $\bar{\bar{B}}_i$ and $\bar{\bar{A}}_i$ blocks contain only dummy equations since the variables $\delta\rho$ do not exist for i=I. This block structure is shown in Figure 4.6.

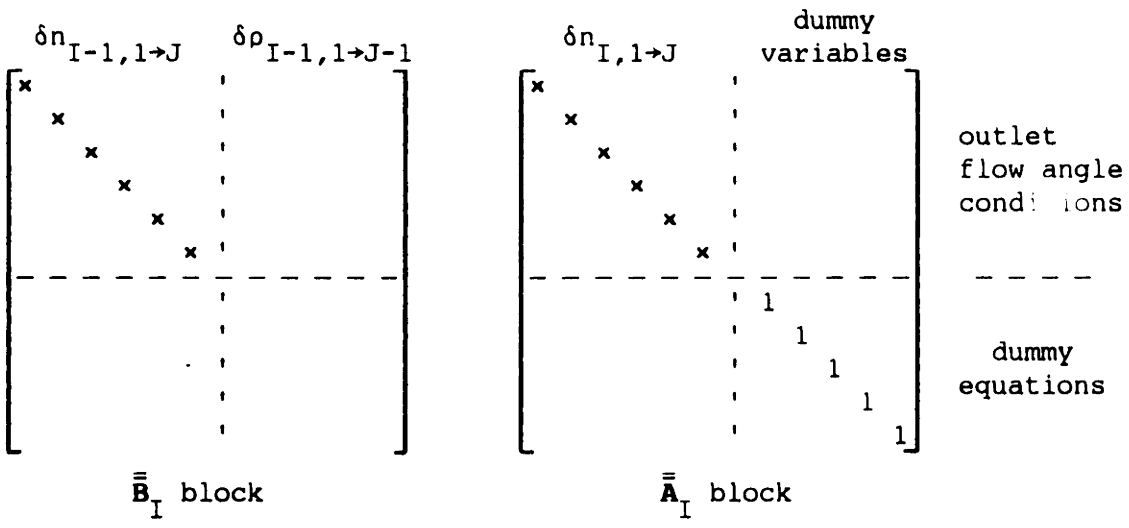

Figure 4.6 $\bar{\bar{Z}}_I$ and $\bar{\bar{B}}_I$ block structure

4.4 Discrete system linearization

In the program, the general linearization procedure is to sequentially sweep down each streamtube, calculating and storing the various residuals and Jacobian entries for each streamwise location. When the program visits a particular cell, it can calculate all the entries for the S-momentum equation, since the S-momentum equation spans only that one cell. This is not possible for the reduced N-momentum equation, since it spans two cells in two adjacent streamtubes. Sweeping down two streamtubes simultaneously would be computationally inefficient and a poor solution to the problem. The procedure adopted is to add on to the Jacobian elements the current cell's contribution to the two reduced N-momentum equations it influences. After the Jacobian entries of the interior equations are stored, the boundary condition entries are calculated and stored.

4.4.1 Interior Euler equations

At the beginning of iteration ν, ρ^{ν}, x^{ν}, y^{ν} at all grid nodes are known. For the sake of clarity, the iteration index "ν" will be omitted from all quantities, unless otherwise stated. For each streamtube, all the geometric quantities are evaluated using equations (2.4-2.8), and also equations (2.19a-b) and (2.21a-b). In general, the Cartesian displacements δx and δy of each node are expressed in terms of a local movement δn along a predefined direction vector $\hat{\mathbf{n}}$ perpendicular to the local streamline, plus a movement proportional to δs_{LE} along another predefined direction. As described in Chapter 3, δs_{LE} is the movement of the stagnation point grid node at a blunt leading edge. For the sake of clarity, the grid node position dependence on δs_{LE} will be ignored until the end of this chapter. The consequences of this dependence will then be discussed.

Because each node is defined to move a distance δn along the predefined direction vector $\hat{\mathbf{n}}$, the Cartesian variations δx and δy can be

trivially related to δn when needed. Hence, all geometric quantities are first linearized in terms of the variations δx and δy.

The streamwise vector $\vec{s}_2$ variation $\delta\vec{s}_2$ is easily related to δx and δy by inspection of its definition (2.7a-b).

$$\delta\vec{s}_2 = \frac{1}{2}\left(\delta x_3^+ + \delta x_3^- - \delta x_2^+ - \delta x_2^- \ , \ \delta y_3^+ + \delta y_3^- - \delta y_2^+ - \delta y_2^- \right) \qquad (4.17)$$

The variation $\delta\vec{s}_1$ is similarly expressed in terms of δx and δy. In practice, only variables subscripted by "$_2$" need to be calculated, since the "$_1$" quantities were calculated and stored for the upstream cell and hence are already available.

The variation δs_2 (s_2 being the modulus of $\vec{s}_2$) is expanded in terms of δx and δy as follows.

$$\delta s_2 = \frac{1}{s_2}\vec{s}_2 \cdot \delta\vec{s}_2 = \frac{\partial s_2}{\partial x_3^+}\delta x_3^+ + \frac{\partial s_2}{\partial x_3^-}\delta x_3^- + \ldots + \frac{\partial s_2}{\partial y_3^+}\delta y_3^+ + \ldots \qquad (4.18)$$

As described in Section 4.2, the horde of sensitivities such as $\partial s_2/\partial x_3^+$ and $\partial s_2/\partial x_2^-$ is calculated and stored. These are as numerous as they are simple and hence are best obtained from the code listing.

As in the case of $\delta\vec{s}_2$ above, the variation $\delta\vec{A}_2$ can be easily obtained in terms of δx and δy from its definition (2.4c-d).

$$\delta\vec{A}_2 = \frac{1}{2}\left(\delta x_3^+ + \delta x_2^+ - \delta x_3^- - \delta x_2^- \ , \ \delta y_3^+ + \delta y_2^+ - \delta y_3^- - \delta y_2^- \right) \qquad (4.19)$$

For instance, $\partial\vec{A}_2/\partial x_3^+ = (1/2 \ , \ 0)$, and $\partial\vec{A}_2/\partial y_2^- = (0 \ , \ -1/2)$.

With $\delta\vec{s}_2$, δs_2, and $\delta\vec{A}_2$ written in terms of δx and δy, the normal area variation δA_{n_2} is expressed in terms of δx and δy as follows.

$$\delta A_{n_2} = \delta\left(\frac{|\vec{s}_2 \times \vec{A}_2|}{s_2}\right) = \frac{1}{s_2}\left(|\vec{s}_2 \times \delta\vec{A}_2| - |\vec{A}_2 \times \delta\vec{s}_2|\right) - \frac{A_{n_2}}{s_2}\,\delta s_2 \qquad (4.20)$$

As described in Section 4.2, sensitivities such as $\partial A_{n_2}/\partial x_3^+$ which are needed to relate δA_{n_2} and δx_3^+ are obtained by substituting expressions for $\delta\vec{A}_2$, $\delta\vec{s}_2$, and δs_2 into (4.20). At the Fortran level, this only involves a chain rule multiplication sequence as illustrated earlier in Section 4.2.

$$\frac{\partial A_{n_2}}{\partial x_3^+} = \frac{\partial A_{n_2}}{\partial A_{x_2}}\frac{\partial A_{x_2}}{\partial x_3^+} + \frac{\partial A_{n_2}}{\partial s_{x_2}}\frac{\partial s_{x_2}}{\partial x_3^+} + \frac{\partial A_{n_2}}{\partial s_2}\frac{\partial s_2}{\partial x_3^+} \qquad (4.21)$$

Expressing the variations of all the other geometric quantities like $\delta|\vec{S}\times\vec{N}|$ follows naturally. The basic procedure is to expand the variations of cross and dot-products, such as

$$\delta|\vec{S}\times\vec{N}| = |\vec{S}\times\delta\vec{N}| - |\vec{N}\times\delta\vec{S}| \quad , \quad \delta(\vec{s}_2\cdot\vec{S}) = \vec{s}_2\cdot\delta\vec{S} + \vec{S}\cdot\delta\vec{s}_2 \qquad (4.22,23)$$

from which sensitivities such as $\partial|\vec{S}\times\vec{N}|/\partial x$ are formed using the chain rule. The nitty-gritty details are best obtained from the code listing.

The remainder of the linearization process deals primarily with the thermodynamic variables. The mass equation

$$m = \rho_2 q_2 A_{n_2} \qquad (2.9)$$

is used to calculate q and to express δq in terms of $\delta\rho$ and δA_n.

$$q_2 = q_2(\rho_2, A_{n_2}) = \frac{m}{\rho_2 A_{n_2}} \quad \rightarrow \quad \delta q_2 = \frac{\partial q_2}{\partial \rho_2}\,\delta\rho_2 + \frac{\partial q_2}{\partial A_{n_2}}\,\delta A_{n_2} \qquad (4.24a\text{-}b)$$

The following sensitivities are evaluated and stored:

$$\frac{\partial q_2}{\partial \rho_2} = -\frac{q_2}{\rho_2} \qquad \frac{\partial q_2}{\partial A_{n_2}} = -\frac{q_2}{A_{n_2}} \tag{4.25a-b}$$

Next, p is calculated as a function of ρ and q using the energy equation,

$$h_t = \frac{\gamma}{\gamma-1}\frac{p_2}{\rho_2} + \frac{1}{2}q_2^2 \tag{2.12}$$

which implies,

$$p_2 = p_2(\rho_2, q_2) = \frac{\gamma-1}{\gamma}\rho_2\left(h_t - \frac{1}{2}q_2^2\right) \quad , \quad \delta p_2 = \frac{\partial p_2}{\partial \rho_2}\delta\rho_2 + \frac{\partial p_2}{\partial q_2}\delta q_2 \tag{4.26a-b}$$

where

$$\frac{\partial p_2}{\partial \rho_2} = \frac{p_2}{\rho_2} \qquad \frac{\partial p_2}{\partial q_2} = -\frac{\gamma-1}{\gamma}\rho_2 q_2 \tag{4.27a-b}$$

The artificial bulk viscosity coefficient

$$\lambda_2 = \frac{1}{\gamma}\max\left(0\ ,\ 1 - \frac{M_c^2}{M^2}\right) \quad , \quad M^2 = \max(M_1^2, M_2^2) \tag{2.25}$$

is linearized by straightforward differentiation. Using the relation $1/M^2 = (\gamma-1)(h_t/q^2 - 1/2)$, the following sensitivities are obtained.

$$\frac{\partial \lambda_2}{\partial q_1} = 2M_c^2\frac{\gamma-1}{\gamma}\frac{h_t}{q_1^3} \quad , \quad \frac{\partial \lambda_2}{\partial q_2} = 0 \qquad \text{if } q_1 > q_2 \tag{4.28a}$$

$$\frac{\partial \lambda_2}{\partial q_1} = 0 \quad , \quad \frac{\partial \lambda_2}{\partial q_2} = 2M_c^2\frac{\gamma-1}{\gamma}\frac{h_t}{q_2^3} \qquad \text{if } q_1 < q_2 \tag{4.28b}$$

Of course, both $\partial\lambda_2/\partial q_1$ and $\partial\lambda_2/\partial q_2$ are zero if λ_2 is zero.

The upwinded speed $\bar{q}_2 = (1-\lambda_2)q_2 + \lambda_2 q_1$ is linearized as follows.

$$\frac{\partial \bar{q}_2}{\partial q_1} = \lambda_2 + (q_2 - q_1)\frac{\partial \lambda_2}{\partial q_1} \quad , \quad \frac{\partial \bar{q}_2}{\partial q_2} = 1 - \lambda_2 + (q_2 - q_1)\frac{\partial \lambda_2}{\partial q_2} \qquad (4.29a\text{-}b)$$

At this point, the S-momentum equation residual R_S defined by

$$R_S \equiv m\bar{q}_1 f_1 - m\bar{q}_2 f_2 + p_1 - p_2 + P_C \frac{|\vec{B}^- \times \vec{B}^+|}{|\vec{S} \times \vec{N}|} = 0 \qquad (2.22)$$

can be linearized in a more or less straightforward fashion.

$$\delta R_S = m\bar{q}_1 \delta f_1 - m\bar{q}_2 \delta f_2 + m f_1 \delta \bar{q}_1 - m f_2 \delta \bar{q}_2 + \delta p_1 - \delta p_2$$

$$+ \frac{|\vec{B}^- \times \vec{B}^+|}{|\vec{S} \times \vec{N}|} \delta P_C + P_C \frac{1}{|\vec{S} \times \vec{N}|} \delta |\vec{B}^- \times \vec{B}^+| - P_C \frac{|\vec{B}^- \times \vec{B}^+|}{|\vec{S} \times \vec{N}|^2} \delta |\vec{S} \times \vec{N}| \qquad (4.30)$$

As described in Section 2.2, all of the variations in (4.30) such as δf, δp, δP_C, are expressed in terms of the primitive variables $\delta\rho$ and δn by using previously calculated sensitivities such as $\partial p/\partial \rho$, $\partial p/\partial A_n$, $\partial A_n/\partial x$, etc.

The reduced N-momentum equation is simply the difference between the two Π pressures

$$2\Pi^+_{i,j-1} - 2\Pi^-_{i,j} = 0 \qquad (2.28)$$

where

$$2\Pi^-_{i,j} \equiv - \left(m\bar{q}_1 g_1 - m\bar{q}_2 g_2 - p_1 - p_2 + P_C \frac{|\vec{A}_1 \times \vec{A}_2|}{|\vec{S} \times \vec{N}|} - 2P_C \right)_j \qquad (2.26)$$

and

$$2\Pi^+_{i,j-1} \equiv \left(m\bar{q}_1 g_1 - m\bar{q}_2 g_2 + p_1 + p_2 + P_C \frac{|\vec{A}_1 \times \vec{A}_2|}{|\vec{S} \times \vec{N}|} + 2P_C \right)_{j-1} \qquad (2.27)$$

Equation (2.28) linearizes to

$$2\,\delta\Pi^+_{i,j-1} - 2\,\delta\Pi^-_{i,j} = 2\Pi^-_{i,j} - 2\Pi^+_{i,j-1} \qquad (4.31)$$

As mentioned earlier, the contributions from the j'th and j-1'th

streamtubes are added onto the appropriate Jacobian entries separately for efficiency. The linearization of the contribution Π^- of the j'th streamtube is very similar to that of the S-momentum equation.

$$2\,\delta\Pi^-_{i,j} = -m\bar{q}_1\delta g_1 + m\bar{q}_2\delta g_2 - mg_1\delta\bar{q}_1 + mg_2\delta\bar{q}_2 + \delta p_1 + \delta p_2$$

$$+ \left(\frac{|\vec{A}_1\times\vec{A}_2|}{|\vec{S}\times\vec{N}|} - 2 \right) \delta P_c + P_c \frac{1}{|\vec{S}\times\vec{N}|}\,\delta|\vec{A}_1\times\vec{A}_2| - P_c \frac{|\vec{A}_1\times\vec{A}_2|}{|\vec{S}\times\vec{N}|^2}\,\delta|\vec{S}\times\vec{N}| \qquad (4.32)$$

The $\Pi^+_{i,j-1}$ residual contribution from the neighboring cell got added on when the program swept through the j-1'th streamtube.

4.4.2 Boundary conditions

The linearized form of the inlet stagnation density condition,

$$\rho_t \equiv \rho_1\left(1 - \frac{1}{2h_t}\,q_1^2\right)^{-1/(\gamma-1)} = \left(\rho_t\right)_{spec} \qquad (2.29)$$

is

$$\frac{\rho_t}{\rho_1}\,\delta\rho_1 + \frac{q_1\rho_t}{(\gamma-1)(h_t-q_1^2/2)}\,\delta q_1 = \left(\rho_t\right)_{spec} - \rho_t \qquad (4.33)$$

As usual, the δq variation is expressed in terms of $\delta\rho$ and δn and the resulting coefficients are stored in the Jacobian matrix.

The linearized form of the solid wall boundary conditions (3.1a-b) is simply

$$\delta n_{i,1} = -\Delta n_{i,1} \qquad (4.34a)$$

$$\delta n_{i,J} = \Delta n_{i,J} \qquad (4.34b)$$

which drives the gap Δn_i between the wall and the wall streamline to zero. The geometry continuity condition (3.2) is very similar to the solid wall and in linearized form is

$$\delta n_{i,1} - \delta n_{i,J} = -\Delta n_i \tag{4.35}$$

where Δn_i is the gap between the 1'st and J'th streamlines as shown in Figures 3.2 and 3.3.

The linearized streamline pressure continuity condition (3.3) is the same as the reduced N-momentum equation (4.31)

$$\delta \Pi^-_{i,1} - \delta \Pi^+_{i,J-1} = \Pi^+_{i,J-1} - \Pi^-_{i,1} \tag{4.36}$$

except that (4.36) straddles the 1'st and J-1'th streamtubes in "wrap around" fashion. The $\delta\Pi$ variations are expressed in terms of only $\delta\rho$ and δn in the same manner as in the reduced N-momentum equation.

The cascade inlet slope constraint

$$\frac{y_{2,j} - y_{1,j}}{x_{2,j} - x_{1,j}} = S_{inl} \tag{3.4}$$

easily linearizes to

$$\delta y_{2,j} - \delta y_{1,j} - S_{inl}\left(\delta x_{2,j} - \delta x_{1,j}\right) - \left(x_{2,j} - x_{1,j}\right) \delta S_{inl}$$

$$= S_{inl}\left(x_{2,j} - x_{1,j}\right) + y_{1,j} - y_{2,j} \tag{4.37}$$

This linearized equation is distinguished from all the previous ones in that it contains the global variable variation δS_{inl}. The coefficient $(x_{1,j} - x_{2,j})$ will therefore appear in the $\bar{\bar{U}}_1$ block in equation (4.16). The linearization of oulet slope condition (3.5), which contains δS_{out}, will likewise have an entry in block $\bar{\bar{U}}_I$.

The airfoil inlet, outlet, and far-field boundary conditions (3.19), (3.20), (3.11), and (3.12) are linearized in more or less the same manner as the cascade inlet and outlet slope constraints. Instead of δS_{inl} and δS_{out}, however, the variations $\delta\Gamma$ and $\delta\alpha$ will appear. These will result in entries in all the $\bar{\bar{U}}_i$ blocks in the system (4.16).

As mentioned at the beginning of Section 4.4.1, the Cartesian displacements δx and δy of each grid node will in general depend on the global variable δs_{LE} as well as the local displacement δn. The only consequence of this dependence is the appearance of a Jacobian entry for δs_{LE} in each linearized equation which involves δx and δy.

4.4.3 Global equations

At this point, the only equations which still need to be linearized are the global equations which have residuals and Jacobian entries in the bottom part of the Newton system (4.16). The procedure used to linearize global equations is identical to the chain rule process used for the interior equations and boundary conditions in the two previous sections. For example, the lift constraint

$$R_L \equiv L_{spec} - \frac{\beta}{2} \sum_{i=i_{LE}}^{i_{TE}} (\bar{x}_{i+1,J}-\bar{x}_{i-1,J})\Pi^{+}_{i,J-1} - (\bar{x}_{i+1,1}-\bar{x}_{i-1,1})\Pi^{-}_{i,1} = 0 \qquad (3.16)$$

linearizes to

$$-\frac{\beta}{2} \sum_{i=i_{LE}}^{i_{TE}} \Big((\bar{x}_{i+1,J}-\bar{x}_{i-1,J})\, \delta\Pi^{+}_{i,J-1} - (\bar{x}_{i+1,1}-\bar{x}_{i-1,1})\, \delta\Pi^{-}_{i,1}$$

$$+ (\delta\bar{x}_{i+1,J}-\delta\bar{x}_{i-1,J})\Pi^{+}_{i,J-1} - (\delta\bar{x}_{i+1,1}-\delta\bar{x}_{i-1,1})\Pi^{-}_{i,1} \Big) = -R_L \qquad (4.38)$$

The variations $\delta\bar{x}$ and $\delta\bar{y}$ are related to δx, δy, and $\delta\alpha$ through the $\bar{x}$ and $\bar{y}$ definitions (3.14a-b). Equation (4.38) will result in Jacobian entries occurring in the $\bar{\bar{G}}_i$ blocks for $i_{LE} \le i \le i_{TE}$ and also in the $\bar{\bar{G}}_g$ block because of the $\delta\alpha$ dependence.

Other global equations are linearized in the same manner. The details are best obtained from the code listing. Once this is accomplished, the linear Newton system is complete, and is solved by the procedure described next.

4.5 Gaussian elimination block solver

The linearized Newton system as it is given by (4.16) is not in the most convenient form for solution. In particular, the global equations and the global variable Jacobian entries disturb the system's block structure. To simplify the solution procedure, system (4.16) is rewritten as the two separate systems (4.39) and (4.40) shown below.

$$\begin{bmatrix} \bar{\bar{A}}_1 & \bar{\bar{C}}_1 & & & & & & & \\ \bar{\bar{B}}_2 & \bar{\bar{A}}_2 & \bar{\bar{C}}_2 & & & & & & \\ \bar{\bar{Z}}_3 & \bar{\bar{B}}_3 & \bar{\bar{A}}_3 & \bar{\bar{C}}_3 & & & & & \\ & . & . & . & . & & & & \\ & & \bar{\bar{Z}}_i & \bar{\bar{B}}_i & \bar{\bar{A}}_i & \bar{\bar{C}}_i & & & \\ & & & . & . & . & . & & \\ & & & & \bar{\bar{Z}} & \bar{\bar{B}} & \bar{\bar{A}} & \bar{\bar{C}} & \\ & & & & & \bar{\bar{Z}} & \bar{\bar{B}} & \bar{\bar{A}} & \bar{\bar{C}} \\ & & & & & & \bar{\bar{Z}}_I & \bar{\bar{B}}_I & \bar{\bar{A}}_I \end{bmatrix} \times \begin{bmatrix} \bar{\delta}_1 \\ \bar{\delta}_2 \\ \bar{\delta}_3 \\ . \\ \bar{\delta}_i \\ . \\ \bar{\delta} \\ \bar{\delta} \\ \bar{\delta}_I \end{bmatrix} = \begin{bmatrix} \bar{R}_1 \\ \bar{R}_2 \\ \bar{R}_3 \\ . \\ \bar{R}_i \\ . \\ \bar{R} \\ \bar{R} \\ \bar{R}_I \end{bmatrix} - \begin{bmatrix} \bar{\bar{U}}_1 \\ \bar{\bar{U}}_2 \\ \bar{\bar{U}}_3 \\ . \\ \bar{\bar{U}}_i \\ . \\ \bar{\bar{U}} \\ \bar{\bar{U}} \\ \bar{\bar{U}}_I \end{bmatrix} \bar{\Delta}_g \qquad (4.39)$$

$$\bar{\bar{G}}_1 \bar{\delta}_1 + \quad \ldots \quad + \bar{\bar{G}}_i \bar{\delta}_i + \quad \ldots \quad + \bar{\bar{G}}_I \bar{\delta}_I + \bar{\bar{G}}_g \bar{\Delta}_g = \bar{R}_g \qquad (4.40)$$

Equation (4.39) is now a "standard" block system with multiple right-hand sides, which is readily solved by a standard block-elimination algorithm, such as the one described in detail by Giles [19]. The basic solution procedure is to first sweep down from the first row, eliminating the $\bar{\bar{B}}$ and $\bar{\bar{Z}}$ blocks and thereby modifying the $\bar{\bar{C}}$ blocks. The modified $\bar{\bar{C}}$ blocks are then eliminated in a backward sweep from the I'th line. The resulting solution has the form

$$\bar{\delta}_i = \bar{r}_i - \bar{\bar{u}}_i \bar{\Delta}_g \qquad , \quad 1 \le i \le I \qquad (4.41)$$

By substituting this into the linearized global equation system (4.40),

a system which involves only the global unknowns is obtained.

$$\left[\bar{\bar{G}}_g - \bar{\bar{G}}_1\bar{\bar{u}}_1 - \ldots - \bar{\bar{G}}_i\bar{\bar{u}}_i - \ldots - \bar{\bar{G}}_I\bar{\bar{u}}_I\right]\bar{\Delta}_g$$

$$= \left\{\bar{R}_g - \bar{\bar{G}}_1\bar{r}_1 - \ldots - \bar{\bar{G}}_i\bar{r}_i - \ldots - \bar{\bar{G}}_I\bar{r}_I\right\} \qquad (4.42)$$

This small (usually 6×6 at most) linear system is easily solved to obtain the global variable vector $\bar{\Delta}_g$, which in turn is substituted back into (4.41) to obtain the local variable solution vector $\bar{\delta}_i$ ($1 \leq i \leq I$).

4.6 Updating the solution

Usually, the updating of the solution consists of simply adding on the density and geometry changes.

$$\rho_{i,j}^{\nu+1} = \rho_{i,j}^{\nu} + r\,\delta\rho_{i,j} \qquad (4.43a)$$

$$x_{i,j}^{\nu+1} = x_{i,j}^{\nu} + r\left(\hat{n}_{x_{i,j}}\delta n_{i,j} + \hat{n}'_{x_{i,j}}\delta s_{LE}\right) \qquad (4.43b)$$

$$y_{i,j}^{\nu+1} = y_{i,j}^{\nu} + r\left(\hat{n}_{y_{i,j}}\delta n_{i,j} + \hat{n}'_{y_{i,j}}\delta s_{LE}\right) \qquad (4.43c)$$

Here, $\hat{n}'$ denotes the direction vector (not a unit vector) along which a grid node moves in response to the stagnation grid point movement. The quantity r is an under-relaxation factor which is usually set to unity, giving the standard Newton method. For the first few Newton iterations, however, it is necessary to use $r < 1$ to prevent non-physical situations such as negative densities from occurring. The value r is chosen so that the density never changes by more than a factor of 2. This rather arbitrary clamp gives robust convergence even with very strong initial transients.

5. INVERSE PROBLEM

5.1 Full inverse formulation

The boundary conditions presented in Chapter 3 have dealt with the direct problem. A body geometry was prescribed, and the flow field and surface pressures were a result of a calculation. An alternative to this procedure is the inverse problem, where surface pressures are prescribed and geometry is calculated as a result. A straightforward implementation of this idea is to replace the fixed-wall boundary condition (3.25) with the condition that the wall pressure at each grid node on the body surface equal some specified value.

$$\Pi^-_{i,1} = \Pi^-_{i_{spec}} \quad , \qquad i_{LE} \leq i \leq i_{TE} \tag{5.1a}$$

$$\Pi^+_{i,J-1} = \Pi^+_{i_{spec}} \quad , \qquad i_{LE} \leq i \leq i_{TE} \tag{5.1b}$$

The inverse problem is not quite that simple, however. Since the grid nodes on the suction and pressure surfaces at the leading and trailing edge stations $i=i_{LE}$ and $i=i_{TE}$ are free to move, there is no guarantee that the resulting body will be closed there. Hence, two requirements which must be imposed on the equations are that the leading and trailing edge gaps be zero, as is illustrated in Figure 5.1.

$$\Delta n_{i_{LE}} = 0 \tag{5.2a}$$

$$\Delta n_{i_{TE}} = 0 \tag{5.2b}$$

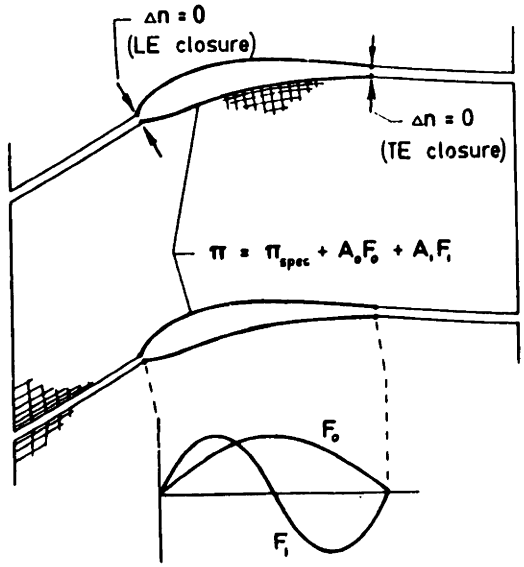

Figure 5.1 Full inverse boundary conditions

The problem with the closure constraints (5.2a-b) is that they are two new equations which have been introduced into the overall equation set, while introducing no new unknowns. Hence the inverse problem as posed above is overconstrained. This impasse can be resolved by considering the work of Lighthill [32], [33], who formulated an exact solution to the inverse problem for airfoils and cascades in incompressible potential flow using conformal mappings between the physical and circle plane domains. Perhaps his most significant result is the proof that the speed (or equivalently, the pressure) distribution on the body cannot be prescribed arbitrarily. If ω is the angular coordinate in the circle plane into which the airfoil is transformed, $q(\omega)$ is the speed on the airfoil surface, and q_∞ is the freestream speed, then the following three integral constraints must hold for the inverse problem to be well-posed and for the airfoil to be closed.

$$\int_0^{2\pi} \ln \frac{q(\omega)}{q_\infty} \begin{pmatrix} 1 \\ \cos\ \omega \\ \sin\ \omega \end{pmatrix} d\omega \;=\; 0 \qquad (5.3a\text{-}c)$$

For compressible flow, constraints such as (5.3a-c) cannot be written down, although it is safe to assume that they exist.

Volpe and Melnik [51] have formulated what can be considered a compressible extension of Lighthill's formulation. Instead of the incompressible conformal mapping techniques, they resort to finite volume full-potential solutions with Dirichlet boundary conditions and a geometry updating procedure based on the resulting transpiration velocity. To make sure that the compressible equivalents of constraints (5.3a-c) can be satisfied, Volpe and Melnik [51] use a prescribed speed distribution of the form

$$q(\omega) \;=\; q_\infty \left(F_0(s(\omega)/s_{max}) \;+\; P_1 F_1(\omega) \;+\; P_2 F_2(\omega) \right) \qquad (5.4)$$

where s is the arc length along the airfoil. F_0, F_1 and F_2 are given shape functions and P_1, P_2, and q_∞ are parameters determined as part of the inverse solution to obtain leading and trailing edge closure, and to enforce consistency between the freestream and surface speeds.

In the present inverse formulation, only two additional free parameters appear to be necessary, since there are only the two closure constraints (5.2a-b) to be satisfied. This paradox is illuminated somewhat by noting the way in which Volpe and Melnik prescribe the surface speed. Their equation (5.4) fixes the fractional arc length position of the stagnation point on the airfoil, or at least ties it to two of the free parameters. In the present scheme, the relative arc lengths of the pressure and suction surfaces are not constrained by the prescribed-pressure conditions (5.1a-b). Hence, the position of the stagnation point on the fractional arc length around the airfoil can be considered as the "missing" degree of freedom which is actually impli-

citly contained in the present formulation.

To include the required two degrees of freedom in the present scheme, equations (5.1a-b) have been modified into a form similar to equation (5.4).

$$\Pi^{-}_{i,1} = \Pi^{-}_{i_{spec}} + A_1 F_{1_i} + A_2 F_{2_i} \qquad (5.5a)$$

$$\Pi^{+}_{i,J-1} = \Pi^{+}_{i_{spec}} + A_1 F_{1_i} + A_2 F_{2_i} \qquad (5.5b)$$

A_1, A_2 are two unknowns which, together with the closure conditions (5.2a-b), result in a well-posed inverse problem. F_1 and F_2 are somewhat arbitrary shape functions of position on the airfoil. Here they are chosen to be simple sine loops, as shown in Figure 5.1.

$$F_{1_i} = \sin(\pi\sigma_i) \qquad F_{2_i} = \sin(2\pi\sigma_i) \qquad (5.6a\text{-}b)$$

σ_i is the fractional arc length from the leading to the trailing edge.

The free parameters included in (5.5a,b) represent an "error" in the prescribed pressure distribution which must be accepted. Perhaps a more lighthearted view might be that they are automatic adjustments made by the solver to the aerodynamic specifications to make sure the airfoil can be manufactured. In either view, the effect of the free parameters can be restricted to limited regions on the surface by appropriately setting the weighting shape functions F_1 and F_2.

The full-inverse problem as formulated above is not well-posed without some constraint on the rigid-body motion of the whole grid and airfoil. In the present scheme, this rigid-body motion is eliminated by simply fixing the leading edge point in space.

$$\delta n_{i_{LE},1} = 0 \qquad (5.7)$$

The additional free parameter in the system is either the outlet slope S_{out} in the cascade case, or the circulation Γ in the airfoil case.

These quantities, which are related to the total lift on the airfoil, must be left as unknowns since they cannot be determined beforehand from the specified surface pressures (5.5a,b). The free parameter terms and geometry which are known only after the calculation are also needed. If the lift is to be prescribed exactly, another free parameter and shape function must be added to (5.5a,b).

5.2 Mixed inverse formulation

In addition to the full-inverse formulation described above, the program implementing the algorithms described in this thesis also handles the mixed-inverse formulation, where the pressure is prescribed on part of the airfoil, and the geometry is prescribed on the rest. This can in fact be considered a generalization of both the direct and full-inverse formulations, since either the prescribed-pressure or the prescribed-geometry parts can in principle encompass the whole airfoil. The ability to mix the two formulations in arbitrary proportions is an extremely useful feature which gives the designer much more overall control over the both the aerodynamic and geometric properties of the airfoil than is present with either formulation alone. The mixed-inverse formulation implemented in the computer program permits the prescribed-pressure part to be on one side of the airfoil at any one time. This restriction, which was made for the sake of simplicity, does not significantly impair the capabilities of the method. This is because the two airfoil sides are usually tailored separately at different operating points.

The portion of the airfoil which has a prescribed-pressure condition imposed on it is termed the "freewall segment." If the endpoint indices of the freewall segment are denoted by i_1 and i_2, then the mixed inverse boundary conditions are expressed as

$$\Pi^{\pm}_{i,j_s} = \Pi^{\pm}_{i_{spec}} + A_1 F_{1_i} + A_2 F_{2_i} \quad , \quad i_1 \le i \le i_2 \qquad (5.8a)$$

$$\Delta n_{i,j} = 0 \quad , \quad \text{elsewhere on airfoil} \qquad (5.8b)$$

The subscript j_s is either 1 or J-1 depending on whether the freewall segment is on the suction or pressure side, respectively. The free parameters A_1 and A_2 have been included in (5.8a) to allow the imposition of geometry continuity conditions at the freewall segment endpoints. These are analogous to the leading and trailing edge closure conditions (5 2a-b) for the full-inverse problem described above. Referring to Figure 5.2, these continuity constraints are

$$\Delta n_{i_1,j_s} = 0 \qquad \Delta n_{i_2,j_s} = 0 \qquad (5.9a\text{-}b)$$

Again, the shape functions F_1 and F_2 are quite arbitrary, and here they are chosen to be simple linear functions over the freewall segment as indicated in Figure 5.2.

$$F_{1_i} = (\sigma_i - \sigma_1) / (\sigma_2 - \sigma_1) \qquad (5.10a)$$

$$F_{2_i} = (\sigma_i - \sigma_2) / (\sigma_2 - \sigma_1) \qquad (5.10b)$$

σ_1 and σ_2 denote the values of σ at i_1 and i_2.

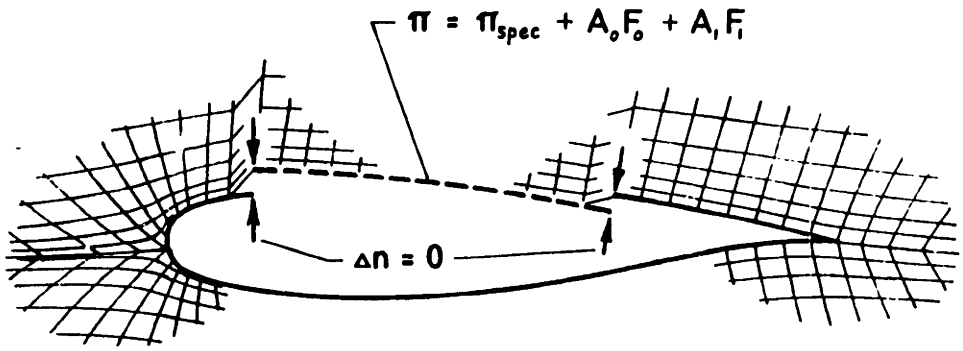

Figure 5.2 Mixed inverse geometry continuity conditions

As formulated, the closure constraints (5.9a-b) enforce geometric continuity at the freewall segment but not slope continuity. In practice this is not a problem, since any slope discontinuities which might app ~ are either not noticable or small enough to be ignored. Nevertheless, it is desirable to have the option of an explicit slope-continuity constraint imposed at the freewall segment endpoints. The simplest approach is to fix the points immediately inside the freewall segment endpoints in addition to fixing the endpoints themselves.

$$\Delta n_{i_1+1,j_s} = 0 \qquad\qquad \Delta n_{i_2-1,j_s} = 0 \qquad\qquad (5.11a\text{-}b)$$

As before, two additional degrees of freedom must also be introduced, otherwise the problem will be overconstrained. This is accomplished by adding more terms to the prescribed-pressure condition (5.6).

$$\Pi^{\pm}_{i,j_s} = \Pi^{\pm}_{i_{spec}} + A_1 F_{1_i} + A_2 F_{2_i} + A_3 F_{3_i} + A_4 F_{4_i} \quad , \; i_1 \leq i \leq i_2 \qquad (5.12)$$

The new shape functions F_3 and F_4 are again arbitrary, but they must be sufficiently different from the other shape functions to keep the influence of the four free parameters $A_1 \ldots A_4$ distinct enough for a well-posed problem. A good choice for F_3 and F_4 but by no means the only one is

$$F_{3_i} = \exp(3F_{2_i}) \qquad F_{4_i} = \exp(3F_{1_i}) \qquad (5.13a\text{-}b)$$

where F_1 and F_2 are defined by (5.10a-b).

The situation where a slope constraint is most likely to be necessary is when a freewall segment endpoint is very close to a stagnation point at the leading edge, say within three nodes or so. Near stagnation points, the geometry tends to be very sensitive to the prescribed pressure, and most full-inverse formulations in literature use some sort of smoothing or a prescribed-curvature constraint at the stagnation point. This geometry sensitivity can also lead to an ill-conditioned mixed-inverse problem if the local leading edge geometry is not sufficiently constrained. Fixing the slope at such an endpoint helps the situation considerably. This is not without negative side effects, however, as the extra terms in the prescribed pressure expression (5.12) usually result in a larger discrepancy between the specified and resultant pressure distributions. It is useful to note that it is perfectly acceptable to use only one of the rightmost free parameter terms in (5.12) and only one of the slope constraints (5.11a-b), thus keeping the number of "error" terms in (5.12) to a minimum.

5.3 Inverse problem Newton solution

The interior S and reduced N-momentum equations in the inverse problem are identical to those in the direct problem. The only differences arise in the boundary conditions. In particular, the block structure shown in Figures 4.3 and 4.4 will only differ in the lines labeled "BC (3.2)" and "BC (3.3)". In these two lines, the prescribed pressure conditions (5.5) or (5.12) replace the fixed-wall condition (3.2). In the mixed inverse case, the fixed-wall condition is replaced only in the block lines corresponding to the freewall segment stations. The linearized specified-pressure boundary condition (5.5a) is

$$\delta\bar{\Pi}_{i,1} - \delta A_1 F_{1_i} - \delta A_2 F_{2_i} = \bar{\Pi}_{i_{spec}} + A_1 F_{1_i} + A_2 F_{2_i} - \bar{\Pi}_{i,1} \qquad (5.14)$$

The $\delta\bar{\Pi}$ variation is readily expressed in terms of the primitive variables $\delta\rho$ and δn as described in Chapter 4. The δA_1 and δA_2 variations are global unknowns whose Jacobian entries are placed in the $\bar{\bar{U}}_i$ blocks in the Newton system (4.16).

The closure constraint (5.2a) in linearized form is

$$\delta n_{i_{LE},1} - \delta n_{i_{LE},J} = -\Delta n_{i_{LE}} \qquad (5.14)$$

This is a global equation and hence its Jacobian entries are placed in the $\bar{\bar{G}}_{i_{LE}}$ block in the system (4.16).

6. BOUNDARY LAYER COUPLING

In this chapter, the integral compressible boundary layer equations used in the viscous/inviscid coupling mode of the solver are derived. Also, the coupling relations and modified Euler boundary conditions through which the boundary layer and wake affect the inviscid flow are presented. A fundamental assumption used in this formulation is that the only effect of the boundary layer and wake is to displace the inviscid flow away from the physical body to create an effective "displacement body." The accuracy of this assumption was investigated by Lighthill [34], who showed it to be accurate provided the ratio of boundary layer thickness to streamline radius of curvature is small. For most aerodynamic flows of interest, this assumption is valid virtually everywhere, with the possible exception of the trailing edge region. A related source of error is the breakdown of the boundary layer approximation itself, caused by a significant normal pressure gradient in the boundary layer. This normal pressure gradient can be caused by streamline curvature at the trailing edge, and also by shock wave impingement. Melnik [38] has developed higher-order corrections for these problem areas which appear to improve accuracy. In this thesis these additional corrections will not be considered, since the development of the basic integral closure formulation and the coupling formulation are the primary goals here. Even without the corrections, the results agree well with experiment as will be demonstrated later.

6.1 The integral boundary layer equations

The starting point of any boundary layer calculation method is the Prandtl boundary layer equations:

mass:
$$\frac{\partial(\rho u)}{\partial \xi} + \frac{\partial(\rho v)}{\partial \eta} = 0 \tag{6.1}$$

momentum:
$$\rho u \frac{\partial u}{\partial \xi} + \rho v \frac{\partial u}{\partial \eta} = \rho_e u_e \frac{du_e}{d\xi} + \frac{\partial \tau}{\partial \eta} \tag{6.2a}$$

$$\tau = \mu \frac{\partial u}{\partial \eta} - \rho\overline{u'v'} \tag{6.2b}$$

enthalpy:
$$\rho u \frac{\partial h_t}{\partial \xi} + \rho v \frac{\partial h_t}{\partial \eta} = \frac{\partial Q}{\partial \eta} \tag{6.3a}$$

$$Q = \frac{\mu}{Pr} \frac{\partial h_t}{\partial \eta} + \mu\left(1 - \frac{1}{Pr}\right) u \frac{\partial u}{\partial \eta} - \rho\overline{h'v'} \tag{6.3b}$$

These equations are expressed in local streamwise and normal wall coordinates ξ,η. The streamwise and normal velocity components are u,v, τ denotes the total shearing plus Reynolds stress, and Q denotes an enthalpy flux. Edge quantities are denoted by the subscript "e". Modern finite-difference techniques can rapidly solve these equations provided appropriate models for the Reynolds stress and the Reynolds heat transport are introduced. In this thesis, the older integral approach to solving these equations will be taken. The only reason for this is that the large number of unknowns introduced by the finite difference approach would make simultaneous solution of the boundary layer equations and inviscid flow field by the Newton method prohibitively expensive. Only adiabatic flows with near-unity Prandtl numbers will be considered. This restriction permits the enthalpy profile to be fairly accurately related to only the velocity profile and the temperature recovery factor. As a result, the enthalpy equation (6.3) can be dropped.

The equations which will be tackled by the integral approach are readily derived from the Prandtl equations (6.1-3). By formally integrating equation (6.2) across the boundary layer, the well-known von Karman momentum integral equation results.

$$\frac{\xi}{\theta}\frac{d\theta}{d\xi} = \frac{\xi}{\theta}\frac{C_f}{2} - \left(\frac{\delta^*}{\theta} + 2 - M_e^2\right)\frac{\xi}{u_e}\frac{du_e}{d\xi} \tag{6.4}$$

The momentum and displacement thicknesses θ and δ^*, and skin friction coefficient C_f are defined as follows.

$$\theta = \int_0^\infty \left(1-\frac{u}{u_e}\right)\frac{\rho u}{\rho u_e}\,d\eta \qquad \delta^* = \int_0^\infty \left(1-\frac{\rho u}{\rho u_e}\right)d\eta \qquad C_f = \frac{2}{\rho_e u_e^2}\,\tau_w \qquad (6.5a\text{-}c)$$

If equation (6.2) is first multiplied through by u and then integrated, the kinetic energy integral equation results:

$$\frac{\xi}{\theta^*}\frac{d\theta^*}{d\xi} = \frac{\xi}{\theta^*}2C_D - \left(\frac{2\delta^{**}}{\theta^*} + 3 - M_e^2\right)\frac{\xi}{u_e}\frac{du_e}{d\xi} \qquad (6.6)$$

The kinetic energy and density thicknesses θ^* and δ^{**}, and dissipation coefficient C_D are defined by

$$\theta^* = \int_0^\infty \left(1-\left(\frac{u}{u_e}\right)^2\right)\frac{\rho u}{\rho u_e}\,d\eta \qquad \delta^{**} = \int_0^\infty \left(1-\frac{\rho}{\rho_e}\right)\frac{u}{u_e}\,d\eta \qquad C_D = \frac{1}{\rho_e u_e^3}\int_0^\infty \tau\,\frac{\partial u}{\partial \eta}\,d\eta \qquad (6.7a\text{-}c)$$

It is useful at this point to define the following three shape parameters:

$$H = \frac{\delta^*}{\theta} \qquad H^* = \frac{\theta^*}{\theta} \qquad H^{**} = \frac{\delta^{**}}{\theta} \qquad (6.8a\text{-}c)$$

By using these shape parameter definitions, and subtracting off equation (6.4) from equation (6.6), the momentum and kinetic energy equations can be written as

$$\frac{\xi}{\theta}\frac{d\theta}{d\xi} = \frac{\xi}{\theta}\frac{C_f}{2} - \left(H + 2 - M_e^2\right)\frac{\xi}{u_e}\frac{du_e}{d\xi} \qquad (6.9)$$

$$\frac{\xi}{H^*}\frac{dH^*}{d\xi} = \frac{\xi}{\theta}\frac{2C_D}{H^*} - \frac{\xi}{\theta}\frac{C_f}{2} - \left(\frac{2H^{**}}{H^*} + 1 - H\right)\frac{\xi}{u_e}\frac{du_e}{d\xi} \qquad (6.10)$$

Equation (6.10) above will now be referred to as the shape parameter equation.

6.2 Laminar closure

The momentum and shape parameter equations (6.9) and (6.10) are valid for both laminar and turbulent boundary layers, as well as for free wakes. The fundamental difficulty with them is that they contain

more than two independent variables and hence some assumptions about the additional unknowns will have to be made if any discernable progress toward their solution is to ensue. Primarily through the personal preference of the author, the two dependent variables are defined to be the momentum and displacement thicknesses θ and δ^*. The edge velocity u_e and edge Mach number M_e can be related to the inviscid flow, and hence do not constitute additional unknowns. A simple count shows that four undefined variables remain: C_f, C_D, H^*, and H^{**}.

For compressible, adiabatic flow, the following assumptions about functional dependencies will be made:

$$H^* = H^*(H_k, M_e, Re_\theta) \qquad H^{**} = H^{**}(H_k, M_e) \qquad (6.11a\text{-}b)$$

$$C_f = C_f(H_k, M_e, Re_\theta) \qquad C_D = C_D(H_k, M_e, Re_\theta) \qquad (6.11c\text{-}d)$$

Here H_k is the kinematic shape parameter, which is defined with the density across the boundary layer assumed constant. It is well known that compressible and incompressible velocity profiles have very nearly the same shapes. This naturally suggests that in compressible flow the above relations should be based on the kinematic shape parameter, which depends solely on the velocity profile. Whitfield [53] has developed an empirical expression for H_k in terms of the conventional shape parameter and edge Mach number:

$$H_k \equiv \frac{\int_0^\infty \left(1-\frac{u}{u_e}\right) d\eta}{\int_0^\infty \left(1-\frac{u}{u_e}\right)\frac{u}{u_e} d\eta} = \frac{H - 0.290\, M_e^2}{1 + 0.113\, M_e^2} \qquad (6.12)$$

This expression assumes adiabatic flow and non-unity Prandtl number (of air), and in reference [53] is shown to be quite accurate up to $M_e = 3$. Here it used for both laminar and turbulent flows.

To deduce the relationships (6.11a-d), some velocity profile family of one or more parameters must be assumed to represent all flows to be computed. For the laminar case, the most obvious choice is the

Falkner-Skan one-parameter family of profiles. By solving the Falkner-Skan equation with prescribed shape parameter by the finite difference method described in Drela [13], the following curve fits have been obtained:

$$H_k^* = \begin{cases} 1.515 + 0.076 \dfrac{(H_k-4)^2}{H_k} & , \quad H_k < 4 \\ 1.515 + 0.040 \dfrac{(H_k-4)^2}{H_k} & , \quad H_k > 4 \end{cases} \tag{6.13a}$$

$$\text{and} \quad H^* = (H_k^* + 0.028M_e^2) \; / \; (1 + 0.014M_e^2) \tag{6.13b}$$

$$Re_\theta \frac{C_f}{2} = \begin{cases} -.067 + 0.01977 \dfrac{(7.4-H_k)^2}{H_k-1} & , \quad H_k < 7.4 \\ -.067 + 0.022 \left(1 - \dfrac{1.4}{H_k-6}\right)^2 & , \quad H_k > 7.4 \end{cases} \tag{6.14}$$

$$Re_\theta \frac{2C_D}{H^*} = \begin{cases} 0.207 + 0.00205 \, (4-H_k)^{5.5} & , \quad H_k < 4 \\ 0.207 - 0.003 \, (H_k-4)^2 & , \quad H_k > 4 \end{cases} \tag{6.15}$$

The additional small compressibility correction in the energy shape parameter relation (6.13b) was obtained from Whitfield [54]. Whitfield's compressibility corrections for the skin friction coefficient and dissipation coefficient, based on Coles' law of corresponding stastations (reference [11]), drop out for the laminar case. Hence, relations (6.14) and (6.15) have no compressibility corrections other than those for H_k.

The expression for the density thickness shape parameter H^{**} which will be used here is one developed by Whitfield [54].

$$H^{**} = \left(\frac{0.064}{H_k - 0.8} + 0.251\right) M_e^2 \tag{6.16}$$

This shape parameter is negligible for low subsonic flows, and has only

a small effect in typical transonic flows. The above expression will be used for both turbulent and laminar flows.

The laminar closure relations (6.13-15) are plotted in Figure 6.1.

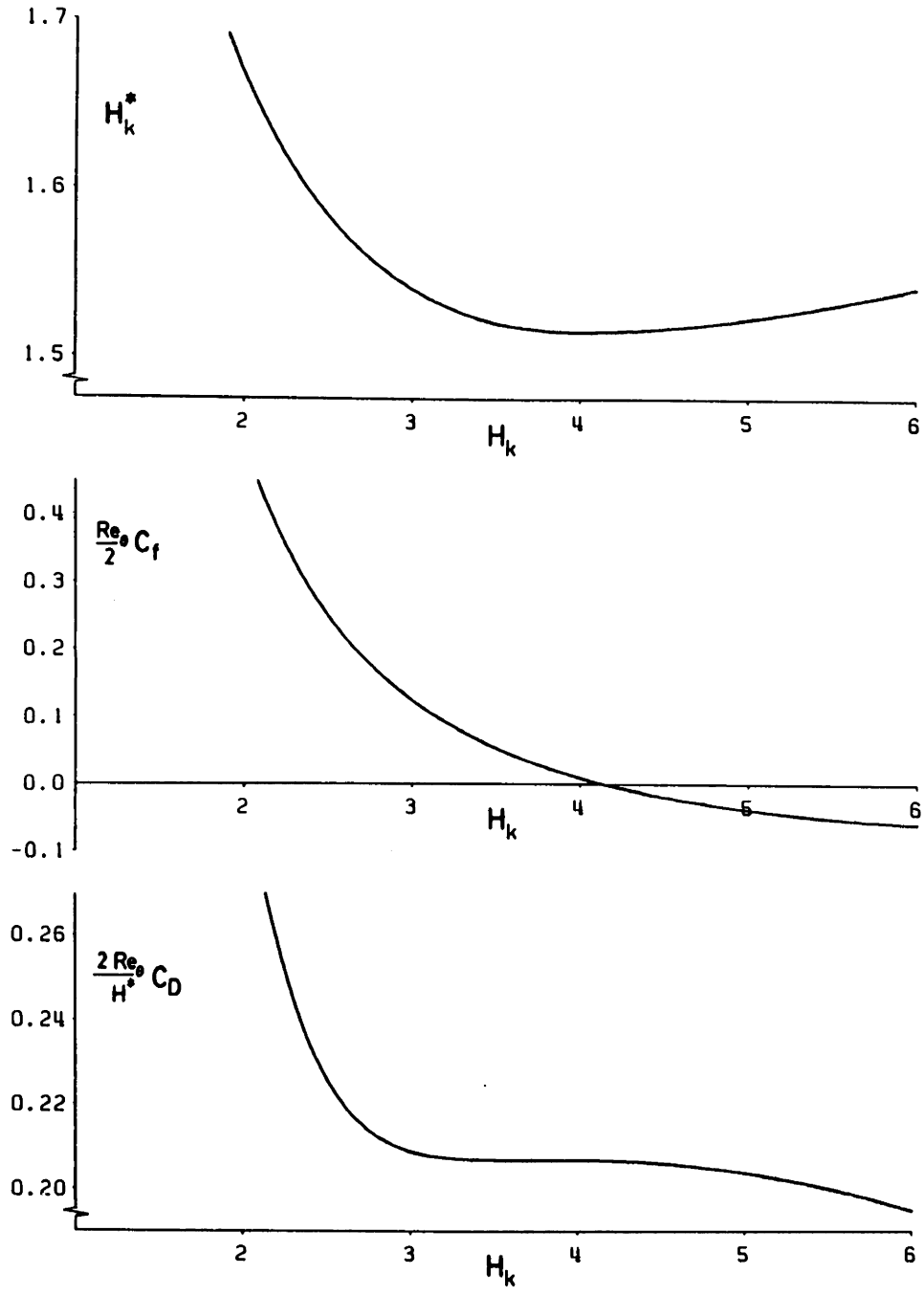

Figure 6.1 Laminar closure relations

When substituted into equations (6.9) and (6.10), a system of two ODE's in the three variables θ, δ^*, and u_e results. If u_e is prescribed, then a so-called direct boundary layer problem for θ and δ^* results. If δ^* is prescribed, an inverse problem for θ and u_e results. Incompressible calculations of both types have been performed for arbitrary u_e and δ^* distributions and compared with the results of the corresponding finite difference calculation and also the well-known one-equation Thwaites' method [7]. One sample comparison is shown in Figure 6.2.

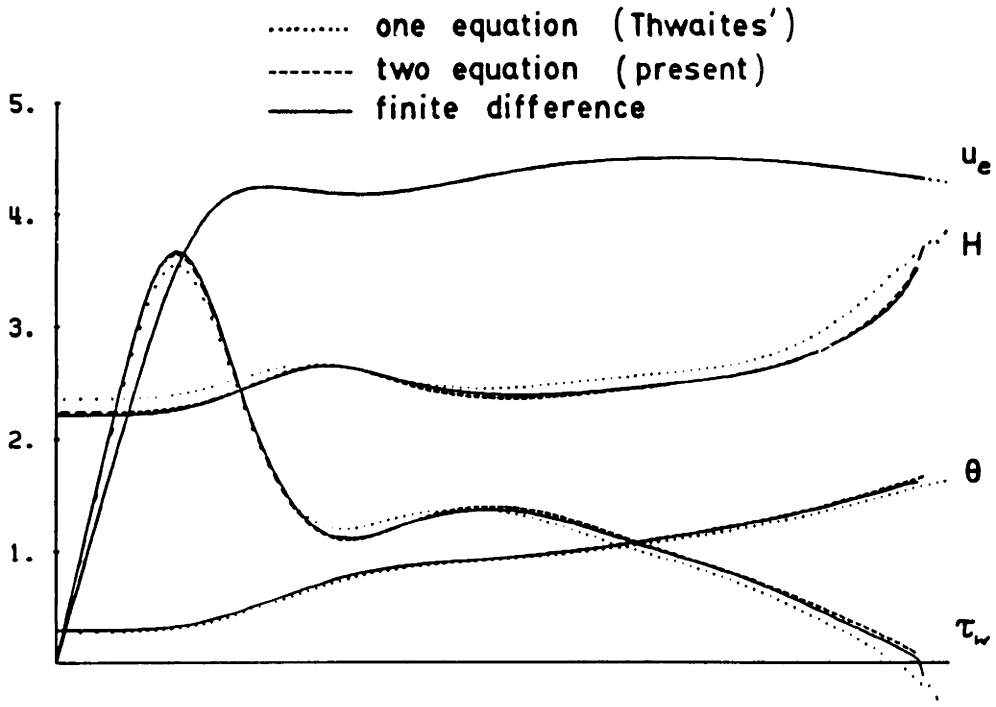

Figure 6.2 Comparison of present formulation, finite difference, and Thwaites' methods for incompressible laminar flow

The present and finite difference results are essentially within plotting accuracy. This level of accuracy can be attributed to two factors. Firstly, almost any laminar velocity profile which can be computed or measured is very nearly the same as a Falkner-Skan profile

with the same shape parameter. This makes the empirical relations (6.13-15) very accurate for all flows (at least in the incompressible case). Secondly, the use of two differential equations rather than one permits the renouncing of any local-similarity assumption in the sense that the local shape parameter and wall shear do not exclusively depend on the local pressure gradient or some transformed equivalent. Thwaites' method, which uses only one equation and hence must assume some sort of local similarity, cannot compare to the accuracy of the two-equation formulation, as Figure 6.2 shows. In particular, the two-equation method has the proper singular behavior at separation and is exact (to within the accuracy of the correlations) for similar flows, whereas Thwaites' method has neither of these features.

6.3 Turbulent closure

For turbulent flow, the task of obtaining empirical relations similar to (6.13-15) is much more formidable. "Exact" numerical solutions to the boundary layers equations are no longer possible due to the presence of the Reynolds stress in equation (6.2b), which must be empirically related to the mean flow. Compounding the problem is that turbulent boundary layers have a two-layer structure, with the thickness of each layer scaling differently on the local Reynolds number Re_θ. Therefore, a one-parameter velocity profile family cannot adequately describe all turbulent boundary layers. This contrasts with the laminar velocity profiles, which have no Reynolds number dependence and a one-parameter profile family suffices.

To formulate a two-parameter turbulent velocity profile, an empirical relation for the skin friction coefficient is necessary. The reason for this is that in turbulent flow the skin friction is the primary scaling parameter for the wall layer. To date, many skin-friction formulas have been proposed and tested against experimental data. The one employed here is due to Swafford [45].

$$F_c C_f = \frac{0.3\, e^{-1.33H_k}}{\left(\log_{10}\left(\frac{Re_\theta}{F_c}\right)\right)^{1.74+0.31H_k}} + 0.00011\left(\tanh\left(4 - \frac{H_k}{.8715}\right) - 1\right) \qquad (6.17)$$

where $$F_c = \left(1 + 0.2M_e^2\right)^{\frac{1}{2}}$$

This function (for M_e=0) together with the laminar C_f function (6.14) is shown in Figure 6.3 for various Reynolds numbers. It is reassuring to note that the laminar and turbulent curves are very similar near $Re_\theta \approx 400$. This is close to the minimum Reynolds number at which a turbulent boundary layer can exist.

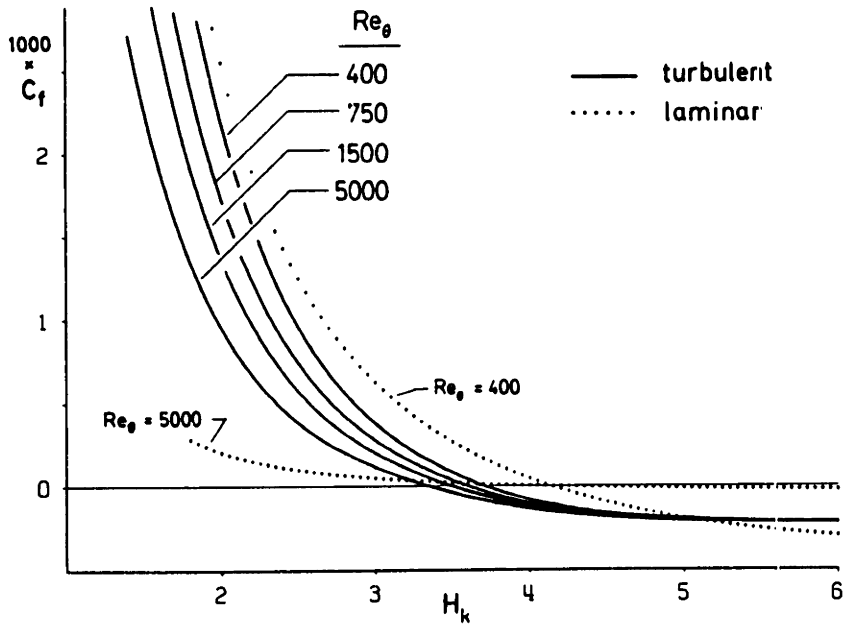

Figure 6.3 Turbulent skin friction correlation

To determine a relation for H^*, an analytic expression for the velocity profile originally derived by Swafford [45] is used. The profile is the sum of two matched asymptotic solutions: an inner solution encompassing the laminar sublayer and the buffer layer, and an outer solution comprising the outer layer, or wake.

$$\frac{u}{u_e} = \frac{u_\tau}{u_e}\frac{s}{.09}\arctan(.09y^+) + \left(1 - \frac{u_\tau}{u_e}\frac{s\pi}{0.18}\right)\tanh^{\frac{1}{2}}\left(a(\eta/\theta)^b\right) \qquad (6.18)$$

where

$$\frac{u_\tau}{u_e} = \left|\frac{C_f}{2}\right|^{\frac{1}{2}} \qquad s = \frac{C_f}{|C_f|} \qquad y^+ = \frac{\rho u_\tau}{\mu}\eta \qquad (6.19a\text{-}c)$$

The two constants a and b can calculated for any given θ and δ^* by using the skin friction formula (6.17) and by substituting the velocity profile expression (6.18) into the θ and δ^* definitions (6.5a,b). This produces a coupled, non-linear 2×2 implicit system for a and b which is solved numerically by the Newton method.

Swafford's velocity profile formula (6.18) has been used by Whitfield [55] and Thomas [46] as a basis for integral boundary layer methods. They assume the limit of infinite Reynolds number ($y^+ \to \infty$) in order to form the H^*-H correlation. In effect, this simplification replaces the inner layer by an equivalent wall slip velocity imposed on the outer layer, which almost completely eliminates the dependence of the H^*-H relation on the Reynolds number. The present author feels this is an unnecessary simplification which tends to produce erratic behavior in transition regions where the Reynolds number Re_θ is usually low. Using the unsimplified equation (6.18), the following expression has been derived for the energy thickness shape parameter H^* after much trial and error:

first define $\qquad H_o = 3.0 + \dfrac{400}{Re_\theta}$, then

$$H_k^* = \begin{cases} 1.505 + \dfrac{4}{Re_\theta} + \left(0.165 - \dfrac{1.6}{\sqrt{Re_\theta}}\right)\dfrac{(H_o - H_k)^{1.6}}{H_k} & , H_k < H_o \\ \\ 1.505 + \dfrac{4}{Re_\theta} + (H_k - H_o)^2\left(\dfrac{.04}{H_k} + .007\,\dfrac{\ln(Re_\theta)}{\left(H_k - H_o + \dfrac{4}{\ln(Re_\theta)}\right)^2}\right) & , H_k > H_o \end{cases} \qquad (6.20)$$

Relation (6.13b) is used to obtain H^* from H_k^*. This rather cumbersome function is plotted in Figure 6.4 for several values of Re_θ, together with the laminar H^* function (6.13). Note that the laminar and turbu-

lent curves nearly coalesce for low Reynolds numbers.

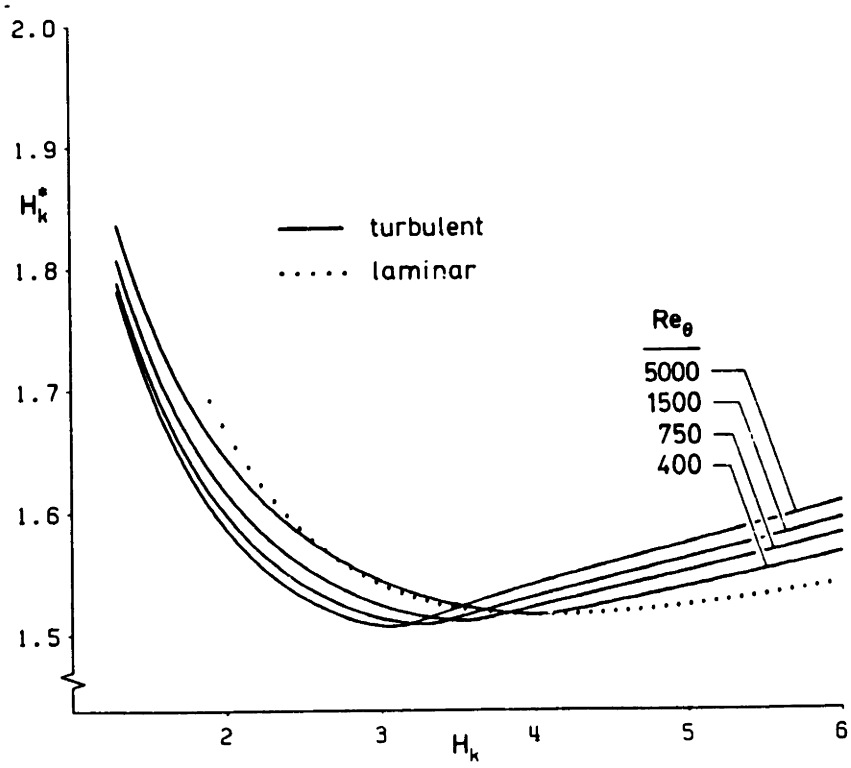

Figure 6.4 Turbulent shape parameter correlation

The most difficult correlation to derive in the turbulent case is for the dissipation coefficient, primarily because it depends the Reynolds stress distribution across the boundary layer. There have been two distinct approaches to determining a disspation coefficient formula. Thomas [46] and Le Balleur [29] have employed the slip velocity concept for the wall layer, together with some eddy viscosity hypothesis for the outer layer. In their approach, the integral in the dissipation coefficient definition (6.7) is broken up into two distinct contributions--one from the wall layer, and one from the outer (wake) layer. As sketched in Figure 6.5, a typical turbulent boundary layer is composed of a wall layer with nearly constant total shear stress and an outer layer where the wake velocity profile and an effective eddy

viscosity are assumed to determine the total shear stress. Assuming the simple half-cosine wake velocity profile of Coles [10],

$$u_{out} = u_s + (u_e - u_s) \sin^2\left(\frac{\pi\eta}{2\eta_e}\right) \qquad \text{(outer layer)} \qquad (6.21)$$

and the eddy viscosity formula of Clauser [9],

$$\mu_t = K \rho u_e \delta^* \quad , \quad K \simeq 0.0168 \qquad \text{(outer layer)} \qquad (6.22)$$

the disspation coefficient integral can be approximated by

$$C_D \equiv \frac{1}{\rho_e u_e^3} \int_0^\infty \tau \frac{\partial u}{\partial \eta} d\eta \simeq \frac{1}{\rho_e u_e^3} \tau_w u_s + \int_0^\infty K u_e \delta^* \left(\frac{\partial u}{\partial \eta}\right)^2_{outer} d\eta \qquad (6.23)$$

where u_s is the slip velocity as shown in Figure 6.5.

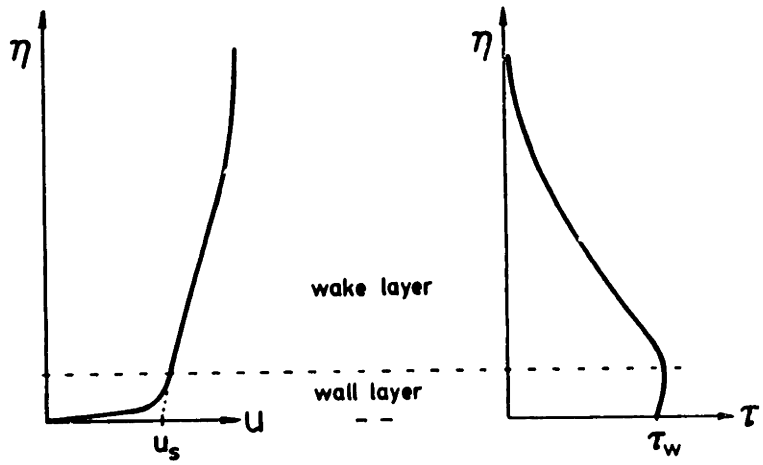

Figure 6.5 Typical turbulent velocity and total shear profiles

The slip velocity is usually deduced from the universal law of the wall and the skin friction coefficient. Assuming that the displacement thickness in the eddy viscosity formula (6.22) is only due to the wake velocity profile, the dissipation coefficient expression (6.23) becomes

$$C_D \simeq \frac{C_f}{2} \frac{u_s}{u_e} + \frac{K\pi^2}{16}\left(1 - \frac{u_s}{u_e}\right)^3 \qquad (6.24)$$

This is the same expression employed by Le Balleur [29].

Another approach to deriving an expression for the dissipation coefficient, and the one adopted in this thesis, is based on the equilibrium boundary layer concept originally postulated and experimentally confirmed by Clauser [9]. As is well known, laminar boundary layers are self-preserving (or similar) if the Falkner-Skan pressure gradient parameter $\xi/u_e\ du_e/d\xi$ is constant everywhere. These special flows were the basis for the laminar closure relations given above. Clauser in his experiments managed to produce turbulent boundary layer flows analogous to the Falkner-Skan family which are self-preserving. In particular, if the pressure gradient parameter β given by

$$\beta \equiv \frac{\delta^* dp}{\tau_w d\xi} = -\frac{2}{C_f}\frac{\delta^* du_e}{u_e d\xi} \tag{6.25}$$

is constant, the modified shape parameter G, defined by

$$G \equiv \frac{H_k - 1}{H_k}\frac{1}{\sqrt{C_f/2}} \tag{6.26}$$

is also constant. Hence, for these special flows, G is only a function of β. An empirical expression for this relationship is

$$G = 6.7\sqrt{1 + 0.75\beta} \tag{6.27}$$

Clauser's experiments were at low Mach numbers, so in the above relations the usual compressibility correction of replacing H by H_k was made. Green et al. [24] used a formula of the same form as (6.27) but with an additional compressibility correction and with slightly different numerical constants to develop an improved version of the well-known Head's entrainment method. Both equation (6.27) and Green's relation are shown in Figure 6.6, which is mostly reproduced from reference [24]. Green's additional compressibility correction lies well within the experimental scatter and is neglected here.

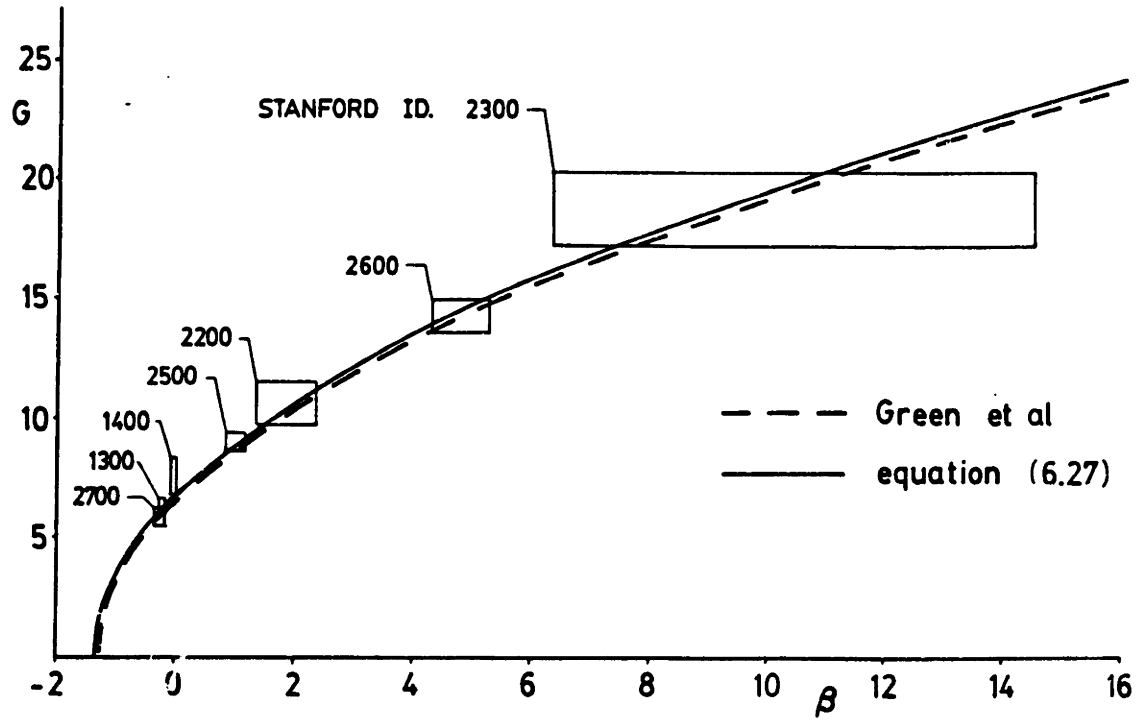

Figure 6.6 Equilibrium G-β locus

Using the definitions of G and β, equation (6.27) can be rearranged to give the equilibrium pressure gradient in terms of the shape parameter and skin friction coefficient.

$$\frac{\delta^* du_e}{u_e d\xi} = \frac{1}{.75}\left(\frac{C_f}{2} - \left(\frac{H_k - 1}{6.7\ H_k}\right)^2\right) \qquad \text{(equilibrium)} \qquad (6.28)$$

To obtain the much sought-after dissipation coefficient formula, the above equilibrium relations are introduced into the shape parameter equation (6.10). First, we note that C_f is primarily a function of H (the dependence on Re_θ is weak). Hence it follows from (6.28) that in equilibrium layers H must be nearly constant. Furthermore, because H^* has already been assumed to be a function of H (again, its dependence on Re_θ is weak), H^* must also be a constant. Noting that $H-2H^{**}/H^* \approx H_k$ and setting the streamwise derivative of H^* to zero in the shape parameter equation (6.10), we have

$$0 = \frac{\xi}{\theta}\frac{2C_D}{H^*} - \frac{\xi}{\theta}\frac{C_f}{2} - \left(1 - H_k\right)\frac{\xi}{u_e}\frac{du_e}{d\xi} \qquad \text{(equilibrium)} \qquad (6.29)$$

Using equation (6.28) to eliminate the velocity gradient, equation (6.29) can be rearranged into

$$\frac{2C_D}{H^*} = \frac{C_f}{2}\left(\frac{4}{H_k} - 1\right)\frac{1}{3} + 0.03\left(\frac{H_k - 1}{H_k}\right)^3 \qquad (6.30)$$

This formula for the dissipation coefficient, despite having been derived solely from a special class of equilibrium flows, is now assumed to apply to all turbulent flows in general. As with the majority of useful statements about turbulent flow, this is mostly a leap of faith, justified primarily by the argument that in the laminar formulation decoupling the local dissipation coefficient from the local pressure gradient led to substantial accuracy gains.

A rather interesting fact is that formula (6.30) for the dissipation coefficient bears a striking resemblance to the slip velocity-based formula (6.24). Perhaps this should not be too surprising, since Clauser's equilibrium flow experiments and the slip velocity concept are the basis of his eddy viscosity expression (6.22), the latter being an essential part of the slip velocity-based formula (6.24). Despite their close resemblance, the author feels that (6.30) is a stronger statement than (6.24), simply because it uses the results of the experimentally derived $G(\beta)$ relation directly, without recourse to any eddy viscosity or slip velocity assumptions. The slip velocity concept will still be used to correct the dissipation coefficient for upstream history in the following section.

6.4 Upstream history: The lag equation

The turbulent dissipation coefficient expression (6.30) as it stands depends only on the shape parameter H and the local Reynolds number Re_θ (H^* and C_f are functions of H and Re_θ). Because the

definition of C_D (6.7c) involves a velocity gradient-weighted integral of the Reynolds stress, expression (6.30) also implies that the Reynolds stresses depend only the local boundary layer parameters. This assumption is quite valid in boundary layers whose turbulence production and dissipation mechanisms are in near equilibrium (Clauser's self-preserving boundary layers are of this type). In fact, nearly all algebraic turbulence models make some such local equilibrium assumption. However, there is abundant experimental evidence (Goldberg [22], Kline et al [28]) that there are significant upstream history effects on Reynolds stresses. These history effects are most important in flows with an adverse pressure gradient increasing in severity downstream, and in "relaxing" flows, where an adverse pressure gradient is suddenly removed. An example of the former flow occurs near the trailing edge of an aft-loaded airfoil. An example of a relaxing flow is the near wake immediately behind the trailing edge.

One of the first attempts to introduce upstream history effects into a boundary layer calculation method was first made by Bradshaw and Ferriss [2,3]. They renounced the usual eddy viscosity assumption by treating the Reynolds stress as an additional unknown and introduced a stress-transport equation of the form

$$u \frac{\partial}{\partial \xi} \frac{(-\overline{u'v'})}{2a_1} + v \frac{\partial}{\partial \eta} \frac{(-\overline{u'v'})}{2a_1} = (-\overline{u'v'}) \frac{\partial u}{\partial \eta} - \frac{(-\overline{u'v'})^{\frac{3}{2}}}{L} - \frac{\partial(\text{diffusion})}{\partial \eta} \qquad (6.31)$$

which is derived from the exact turbulent kinetic energy transport equation with appropriate thin shear layer assumptions and a postulated proportionality between turbulent kinetic energy $\overline{u'^2 + v'^2 + w'^2}$ and Reynolds stress $-\overline{u'v'}$, a_1 being the constant of proportionality. The dissipation length L is equal to $\kappa\eta$ (the mixing length) in the wall layer and roughly 0.075δ in the outer layer, δ being the thickness of the boundary layer.

It is possible to significantly simplify equation (6.31) for use in an integral boundary layer formulation without losing its physical content. Green et al [24] consider the point of maximum Reynolds stress as being representative of the Reynolds stress level for the entire boundary layer. A useful non-dimensional quantity in this context is the shear stress coefficient C_τ:

$$C_\tau = \frac{1}{u_e^2} (-\overline{u'v'})_{max} \tag{6.32}$$

Green assumes that at the maximum shear stress point, L is equal to the conventional mixing length. Hence, at the max shear stress point, the velocity gradient is given by

$$\frac{\partial u}{\partial \eta} = \frac{1}{L} (-\overline{u'v'})^{\frac{1}{2}}_{max} \tag{6.33}$$

Using the above relations for C_τ and $\partial u/\partial\eta$, and neglecting normal convection, the Reynolds stress transport equation (6.31) can be written as

$$\frac{\delta}{C_\tau} \frac{dC_\tau}{d\xi} = 2a_1 \frac{u_e}{u} \frac{\delta}{L} (C_{\tau_{eq}}^{\frac{1}{2}} - C_\tau^{\frac{1}{2}}) - \frac{\partial(\text{diffusion})}{\partial\eta} - \frac{2\delta}{u_e} \frac{du_e}{d\xi} \tag{6.34}$$

where the entire equation is applied at the maximum shear stress point. $(C_\tau)_{eq}$ is the value of shear stress coefficient which would occur if the local boundary layer was part of an equilibrium flow. After obtaining equation (6.34), Green goes on to derive a rather elaborate formulation for the diffusion term. Here, such complications are

avoided by discarding outright the last two terms in equation (6.43), on the grounds that the other two terms generally form the dominant balance in (6.43). Thomas [46] makes the same simplification in his integral formulation. Equation (6.34) thus becomes

$$\frac{\delta}{C_\tau}\frac{dC_\tau}{d\xi} = K_c\,(C_{\tau_{eq}}^{\frac{1}{2}} - C_\tau^{\frac{1}{2}}) \qquad (6.35)$$

Using the commonly accepted values $a_1 = .15$, $u_e/u = 1.5$, and $L/\delta = .08$, Green obtains $K_c = 5.6$. In the present formulation, the value $K_c = 4.2$ was adopted in equation (6.35) since it seemed to produce the best results for virtually nearly all the test cases calculated.

The only task which remains is to relate δ and $(C_\tau)_{eq}$ to the dissipation coefficient and the other boundary layer parameters. An expression for δ was obtained from Green et al [24] and simplified slightly to produce

$$\delta = \theta\left(3.15 + \frac{1.72}{H_k - 1}\right) + \delta^* \qquad (6.36)$$

By invoking the slip-velocity concept, with its distinct wall and wake contributions, the dissipation coefficient formula (6.30) for equilibrium flows is written as

$$\frac{2C_D}{H^*} = \frac{C_f}{2}U_s + C_{\tau_{eq}}(1 - U_s)^3 \qquad (6.37)$$

where the non-dimensional slip velocity $U_s = u_s/u_e$ and the equilibrium shear stress coefficient $(C_\tau)_{eq}$ are now defined by

$$U_s = \frac{H^*}{6}\left(\frac{4}{H_k} - 1\right) \qquad (6.38)$$

and

$$C_{\tau_{eq}} = \frac{H^*}{2}\frac{0.03}{1 - U_s}\left(\frac{H_k - 1}{H_k}\right)^3 \qquad (6.39)$$

These definitions are arrived upon by the simple requirement th[illegible]he two dissipation coefficient formulas (6.30) and (6.37) become ic

in equilibrium flows where $C_\tau = (C_\tau)_{eq}$. The resulting non-equilibrium formula for the dissipation coefficient is finally given by

$$\frac{2C_D}{H^*} = \frac{C_f}{2}\left(\frac{4}{H_k} - 1\right)\frac{1}{3} + \frac{2}{H^*}C_\tau(1 - U_s) \qquad (6.40)$$

where U_s is given by its definition (6.38).

A physical interpretation of (6.40) is as follows. The dissipation coefficient is composed of a wall and a wake contribution, each of which is composed of a shear stress scale and a velocity scale. The wall contribution from the wall layer, given by the term in (6.40) containing the wall shear coefficient C_f, is determined strictly by the local boundary layer parameters, since C_f is a function of Re_θ and H_k. This is consistent with the notion of a universal wall layer, which is known from a preponderence of experimental data to be unaffected by upstream history. The wake contribution, given by the rightmost term in (6.40) does not depend strictly on the local conditions, since C_τ is governed by the rate equation (6.35) and will spatially lag its local equilibrium value $(C_\tau)_{eq}$. This models the relatively slow response of the wake layer Reynolds stresses to the local conditions. However crude this modeling may be, it is still preferable to the local-equilibrium assumption, which was convincingly shown in the 1968 Stanford Conference [28] to give poor results for rapidly changing flows. In slowly changing flows, C_τ closely follows $(C_\tau)_{eq}$ and any inaccuracies in the rate equation (6.35) are irrelevant.

6.5 Wakes

The integral momentum and shape parameter equations (6.9) and (6.10) remain valid for a free wake if the terms containing the wall shear coefficient C_f are discarded. The problem is then reduced to formulating the necessary closure relations (6.11a-d) which are valid for free wakes. For laminar wakes, this problem is resolved by noting that laminar wakes do not occur in aerodynamic flows of interest as a

rule. This is because the inflection velocity profiles invariably present in free wakes make a good habitat for exponentially-growing disturbances which rapidly break down into turbulence. At momentum thickness's Reynolds numbers greater than ~50, this process is extremely rapid, making the concept of a "laminar wake" mostly a contradiction in terms. Clearly, only turbulent free wake closure relations need to be developed.

As it turns out, the turbulent boundary layer closure relations already developed above describe turbulent wakes quite well if the wall shear coefficient C_f is simply set to zero. This is because the "wake" layer of a boundary layer is nearly indistinguishable in its properties from a free wake (hence the name). By setting $C_f = 0$, the wall layer contribution to the dissipation coefficient C_D in equation (6.40) disappears, and what is left adequately describes the dissipation coefficient in a free wake. The turbulent energy thickness shape parameter definition (6.23) is used unchanged for wakes. This is justified on the grounds that a free wake is essentially a turbulent boundary layer sans the wall layer, the latter contributing very little to the H^*-H correlation. A similar argument leads to the the use of the H^{**} definition (6.16) for free wakes without changes.

The lag equation (6.35) should in principle be modified to reflect the more vigorous mixing processes observed in wakes, which tend to increase the dissipation and speed up the rate at which the maximum shear stress coefficient C_τ approaches its equilibrium value. Green makes such a modification to his lag-entrainment method. His argument is that a wake (which is treated as two boundary layers with zero C_f) is roughly twice as thick as its two halves and hence its largest eddies will be twice as large, resulting in increased mixing rates. However, Green's argument holds only for symmetric or nearly-symmetric wakes. In a typical near-wake behind a lifting airfoil, the thicknesses between the upper and lower wakes can differ by more than a factor of ten. In such a situation, the largest eddy scale in the near wake

cannot differ significantly from that in the thicker boundary layer at the trailing edge. Although elaborate correction schemes involving the degree of wake assymetry can be envisioned, this thesis circumvents this quagmire altogether by using the unchanged lag equation (6.35) for all turbulent free wakes. It must be kept in mind that the lag equation is itself a correction to the basic boundary layer formulation, so neglecting to correct a correction can hardly be criticized.

6.6 Transition

The problem of transition is actually composed of two distinct problems: determining the point of the onset of transition, and formulation of the governing boundary layer equations in the transition region itself. To predict the onset of transition, a spatial-amplification theory based on the Orr-Sommerfeld equation is used here (also known in literature as the e^9 method). The boundary layer formulation used in the transition region is derived from simple intermittency-weighted averages of the laminar and turbulent correlations developed above (also known in literature as ad-hoc but workable nevertheless).

The Orr-Sommerfeld equation (derived and discussed extensively in Obremski, Morovkin, and Landahl [40], and in Mack [35]) governs the growth and decay of infinitesimal wave-like disturbances in two or three-dimensional shear layers. Since the unstable growth of disturbances is known to be the precursor of free transition in boundary layers, the calculation of the growth of such disturbances via the Orr-Sommerfeld equation is a fairly sound basis for transition prediction. The procedure in this thesis is to integrate the growth rate of the disturbance with the most unstable frequency downstream from the point of instability to obtain the amplitude of that disturbance. Transition is assumed to occur when the integrated amplitude has grown by more than a factor of e^9 (≈ 8100). This is a wholly empirical assumption and is perhaps the weakest link in the method. The exponent "9" actually can vary between about 7 and 11 depending on quantities

such as free stream turbulence, surface roughness, and background noise level as discussed in Cebeci and Bradshaw [7]. These effects will not be considered here.

Appendix D describes the method used to derive the spatial amplification curve envelopes in H-ωRe_θ parameter space using the Falkner-Skan profile family. As done by Gleyzes et al [21], the envelopes are approximated by straight lines for computational expediency. The equation for a typical amplification ratio envelope is

$$\ln(A/A_0) \equiv \tilde{n} = \frac{dn}{dRe_\theta}(H)\ \{Re_\theta - Re_{\theta_0}(H)\} \qquad (6.41)$$

where the slope $d\tilde{n}/dRe_\theta$ and the critical Reynolds number Re_{θ_0} are given by

$$\frac{d\tilde{n}}{dRe_\theta} = 0.01\left(\left(2.4H - 3.7 + 2.5\tanh[1.5(H-3.1)]\right)^2 + 0.25\right)^{\frac{1}{2}} \qquad (6.42)$$

$$\log_{10}Re_{\theta_0} = \left(\frac{1.415}{H-1} - .489\right)\tanh\left(\frac{20.}{H-1} - 12.9\right) + \frac{3.295}{H-1} + .440 \qquad (6.43)$$

Figure 6.7 shows the envelopes defined by equations (6.41-43) together with the actual amplification curves calculated from the Orr-Sommerfeld equation.

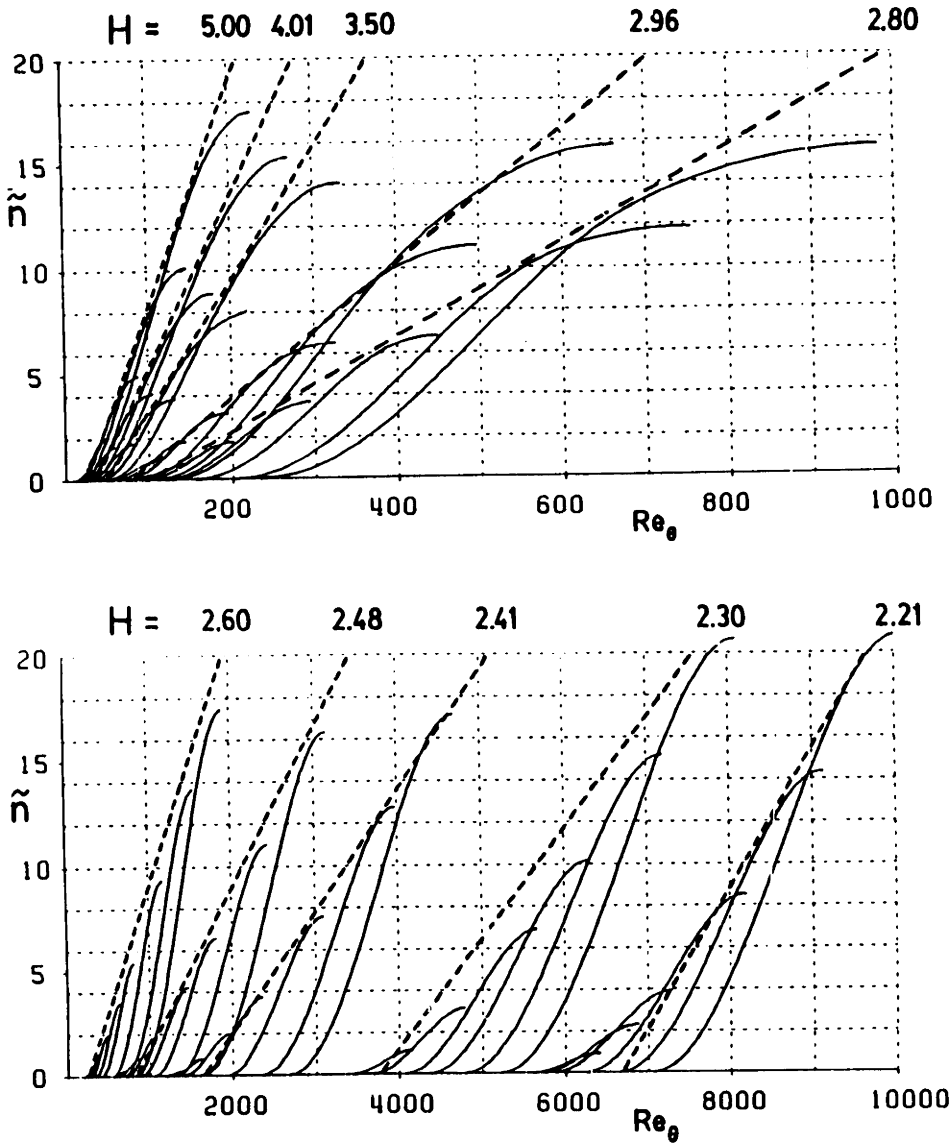

Figure 6.7 Orr-Sommerfeld spatial amplification curves

For similar flows H is constant, and Re_θ is uniquely related to the streamwise coordinate ξ. Hence, equation (6.41) immediately gives the amplitude ratio $\tilde{n}$ as a unique function of ξ. The onset of transition then occurs at the point where $\tilde{n}=9$. For non-similar flows, it is more physically realistic to use ξ as the spatial amplification coordinate rather than Re_θ. Using some basic properties of the Falkner-Skan profile family, the conversion from Re_θ to ξ is accomplished as follows.

$$\frac{d\tilde{n}}{d\xi} = \frac{d\tilde{n}}{dRe_\theta}\frac{dRe_\theta}{d\xi} = \frac{d\tilde{n}}{dRe_\theta}\frac{1}{2}\left(\frac{\xi}{u_e}\frac{du_e}{d\xi} + 1\right)\frac{\rho_e u_e \theta}{\mu_e \xi}^2 \frac{1}{\theta} \tag{6.44}$$

Using the empirical relations

$$\frac{\rho_e u_e \theta}{\mu_e \xi}^2 \equiv \ell(H) = (6.54H - 14.07)/H^2 \tag{6.45}$$

and

$$\frac{\xi}{u_e}\frac{du_e}{d\xi} \equiv m(H) = \left(0.058\frac{(H-4)^2}{H-1} - 0.068\right)\frac{1}{\ell(H)} , \tag{6.46}$$

the spatial amplification rate is expressed as a function of H and θ.

$$\frac{d\tilde{n}}{d\xi}(H,\theta) = \frac{d\tilde{n}}{dRe_\theta}(H)\frac{m(H) + 1}{2}\ell(H)\frac{1}{\theta} \tag{6.47}$$

This amplification rate can then be integrated downstream from the instability point ξ_{cr} (where $Re_\theta = Re_{\theta_o}$).

$$\tilde{n}(\xi) = \int_{\xi_{cr}}^{\xi} \frac{d\tilde{n}}{d\xi}\, d\xi \tag{6.48}$$

Again, the onset of transition occurs at the point where $\tilde{n} = 9$.

In the actual implementation of the present transition criterion, equation (6.48) is not used directly. Instead, the differential amplification equation (6.47) is discretized and solved as part of the global Newton system. The transition onset location can thus be properly linearized. This is a much more robust procedure than if the integral equation (6.48) was used to explicitly set the transition onset location every iteration.

For compressible flows, the only modification is to replace the shape parameter H in equations (6.41-47) by the kinematic shape parameter H_k. This is justified on the grounds that the velocity profile shape is by far the most dominant characteristic which determines the amplification rates.

Although the point of transition onset has been defined, there is

still the problem of formulating the governing equations in the transition region itself. The fundamental problem here is that it is nearly impossible to make useful quantitative statements about transitioning flows. Tried and true principles such as the law of the wall and the law of the wake deal with the class of equilibrium or near-equilibrium layers, to which transitioning flow certainly does not belong.

The simple transition formulation in this thesis hinges on the close similarity of the laminar and turbulent C_f and H^* correlations at the low Reynolds numbers typically found at transition. Because of this close correspondence, the precise manner in which the changeover from the laminar to turbulent correlations is made has been found to have little effect on the overall development of the boundary layer. At the particular streamwise station i_{tr} immediately following transition onset, the actual values of C_f and H^* used in the discrete equations are taken to be weighted averages of the laminar and turbulent values, with weighting factors of $(1-\gamma_{tr})$ and γ_{tr}, respectively. For instance, the actual H^* used in the equations at $i=i_{tr}$ is given by

$$H^* = (1-\gamma_{tr})\, H^*_{laminar} + \gamma_{tr}\, H^*_{turbulent} \qquad (6.49)$$

An analogous expression is used for C_f. The factor γ_{tr} is related to the amplification ratio $\tilde{n}$ at $i=i_{tr}$ by the expression

$$\gamma_{tr} = \frac{\tilde{n}_i - 9}{(dn/d\xi)_i} \frac{1}{\xi_i - \xi_{i-1}} \quad , \quad i = i_{tr} \qquad (6.50)$$

with $\gamma_{tr} = 0$ for $i < i_{tr}$ and $\gamma_{tr}=1$ for $i > i_{tr}$.

In contrast to C_f and H^*, the laminar and turbulent dissipation coefficients differ substantially even at low Reynolds numbers, with the turbulent dissipation coefficient being markedly larger. The turbulent Reynolds stresses (represented by C_τ), which are the cause of the turbulent dissipation being higher than the laminar dissipation, certainly do not develop instantaneously at transition onset, but build up gradually. In the present formulation, this gradual build-up is crude-

ly modeled by the shear coefficient rate equation (6.35). At $i = i_{tr}$, the shear stress coefficient C_τ is taken to be 0.7 times its equilibrium value, and is then allowed to approach its equilibrium value as usual via equation (6.35). No semblance of physical correctness is claimed in this admittedly ad-hoc scheme, since the rate equation (6.35) certainly does not apply to transitioning flows. Most other workers [7,29], model the gradual dissipation build-up by applying the averaging form (6.49) to all relevant quantities, including the dissipation coefficient, and varying γ_{tr} continuously from 0 to 1 in the transition zone according to various empirical formulas. It must be stressed, however, that the exact form of the switch from the laminar to the turbulent correlations does not appear to markedly affect the overall development of the boundary layer, probably because the momentum and shape parameter equations prevent rapid changes in the all-important momentum thickness and shape parameter distributions. In this view, the primary virtues of the present transition formulation are that it produces a reasonable streamwise transition length and that it can be incorporated into the global Newton system.

6.7 Discretization

Figure 6.8 shows the location of the boundary layer variables in relation to the inviscid grid, with the subscript "1" denoting station i-1 and "2" denoting station i. The subscript "a" denotes a simple average between the two stations. For instance,

$$\theta_a = \frac{1}{2}(\theta_1 + \theta_2) \tag{6.51}$$

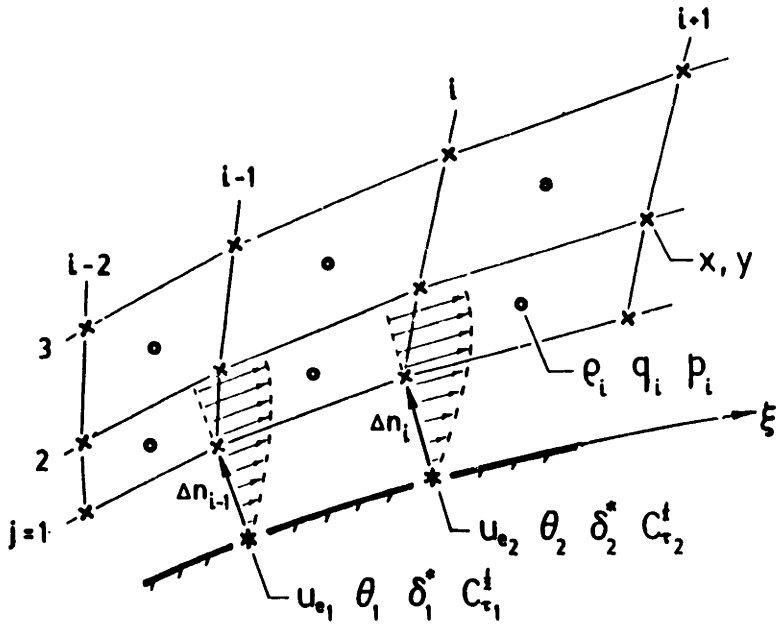

Figure 6.8 Boundary layer variable locations (suction side)

There are three differential equations to be discretized: the momentum equation (6.9), the shape parameter equation (6.10), and the shear stress coefficient lag equation (6.40). The dependent variables are defined to be θ, δ^*, and $\sqrt{C_\tau}$. The edge velocity is also unknown, but as mentioned earlier, it is related to the inviscid variables and is not an additional unknown. In the laminar portions, $i \le i_{tr}$, the amplification rate equation (6.47) replaces the lag equation (6.40), and the amplification ratio $\tilde{n}$ replaces $\sqrt{C_\tau}$ as the dependent variable.

The momentum equation (6.9) is discretized with central two-point differences for accuracy.

$$\frac{\ln(\theta_2/\theta_1)}{\ln(\xi_2/\xi_1)} - \frac{\xi_a}{\theta_a}\frac{C_f}{2} + \left(H_a + 2 - M_{e_a}^2\right)\frac{\ln(u_{e_2}/u_{e_1})}{\ln(\xi_2/\xi_1)} = 0 \qquad (6.52)$$

where $C_f = C_f(H_{k_a}, Re_{\theta_a}, M_{e_a})$ as given by (6.14) and/or (6.17).

Logarithmic differencing of the derivative terms is used because it is exact in similar flows, and thus tends to diminish discretization errors from large $\Delta\xi/\xi$ values which occur near the leading edge. At

the first boundary layer station ($i = i_{LE}+1$), the boundary layer is assumed to be similar and these derivative terms are set to their known values obtained from similar boundary layer theory (Cebeci and Bradshaw [7]). For the particular case of a blunt leading edge with a stagnation point, $\xi/u_e \, du_e/d\xi = 1$ and $\xi/\theta \, d\theta/d\xi = 0$.

In discretizing the shape parameter equation (6.10) it is convenient to define

$$\tilde{C}_D \equiv \frac{2C_D}{H^*} \tag{6.53}$$

Again using central two-point differences for accuracy, the shape parameter equation (6.10) is discretized as

$$\frac{\ln(H_2^*/H_1^*)}{\ln(\xi_2/\xi_1)} + \frac{\xi_a}{\theta_a}\left(\frac{C_f}{2} - \tilde{C}_D\right) + \left(\frac{2H^{**}}{H_a^*} + 1 - H_a\right)\frac{\ln(u_{e_2}/u_{e_1})}{\ln(\xi_2/\xi_1)} = 0 \tag{6.54}$$

where $C_f = C_f(H_{k_a}, Re_{\theta_a}, M_{e_a})$ as given by (6.14) and/or (6.18),

$\tilde{C}_D = \tilde{C}_D(H_{k_a}, Re_{\theta_a}, M_{e_a})$ as given by (6.16) and/or (6.48),

and $H^{**} = H^{**}(H_{k_a}, M_{e_a})$ as given by (6.17)

Special care must be taken in discretizing the shear stress coefficient lag equation. In high Reynolds number flows, the presence of the small quantity δ on the left hand side of equation (6.35) makes it spatially stiff. To avoid any numerical difficulties, it is discretized using Backward Euler where the derivatives are differenced between ξ_1 and ξ_2 as before, but the right hand source term is evaluated at ξ_2 instead of at the midpoint.

$$2\frac{\delta_2 - \delta_1}{C_{\tau_2}^{\frac{1}{2}}}\frac{C_{\tau_2}^{\frac{1}{2}} - C_{\tau_1}^{\frac{1}{2}}}{\xi_2 - \xi_1} - K_c\left(C_{\tau_{eq_2}}^{\frac{1}{2}} - C_{\tau_2}^{\frac{1}{2}}\right) = 0 \tag{6.55}$$

where $\delta_2 = \theta_2\left(3.15 + \frac{1.72}{H_{k_2} - 1}\right) + \delta_2^*$

and $C_{\tau_{eq_2}}^{\frac{1}{2}} = \left(C_{\tau_{eq}}(H_2^*, H_{k_2})\right)^{\frac{1}{2}}$ as given by (6.39).

In the laminar portion ($i \leq i_{tr}$), the above equation is replaced by the discretized amplification equation (6.47).

$$\frac{\tilde{n}_2 - \tilde{n}_1}{\xi_2 - \xi_1} - \frac{d\tilde{n}}{d\xi}(H_{k_2}) \frac{1}{2}\left(m(H_{k_2}) + 1\right) \ell(H_{k_2}) \frac{1}{\theta_2} = 0 \qquad (6.56)$$

6.8 Coupling and boundary conditions

The presence of a boundary layer or wake modifies the solid-wall boundary condition (3.1) which is applied to the inviscid equations. Without the boundary layer, the boundary condition is simply the specification of the surface streamline position. With the boundary layer present, this condition is replaced by a constraint that the inviscid surface streamline is displaced from the solid wall by the distance Δn which is equal to the displacement thickness δ^* (Figure 6.8).

$$\delta_i^* = \Delta n_i \qquad (6.57)$$

In the wake the prescribed conditions are that the wake thickness Δn is equal to the sum of the upper and lower δ^* values (Figure 6.9), and that there is no pressure jump across the wake.

$$\delta_{u_i}^* + \delta_{\ell_i}^* = \Delta n_i \qquad (6.58)$$

$$\Pi_{i,J-1}^{+} - \Pi_{i,1}^{-} = 0 \qquad (6.59)$$

Note that equation (6.59) is merely the same pressure-periodicity boundary condition used in the purely inviscid cascade and airfoil cases as described in Chapter 3. Also, if $\delta^* \equiv 0$, equations (6.58) and (6.59) reduce to the inviscid solid wall and geometry-continuity bound-

ary conditions described in Chapter 3.

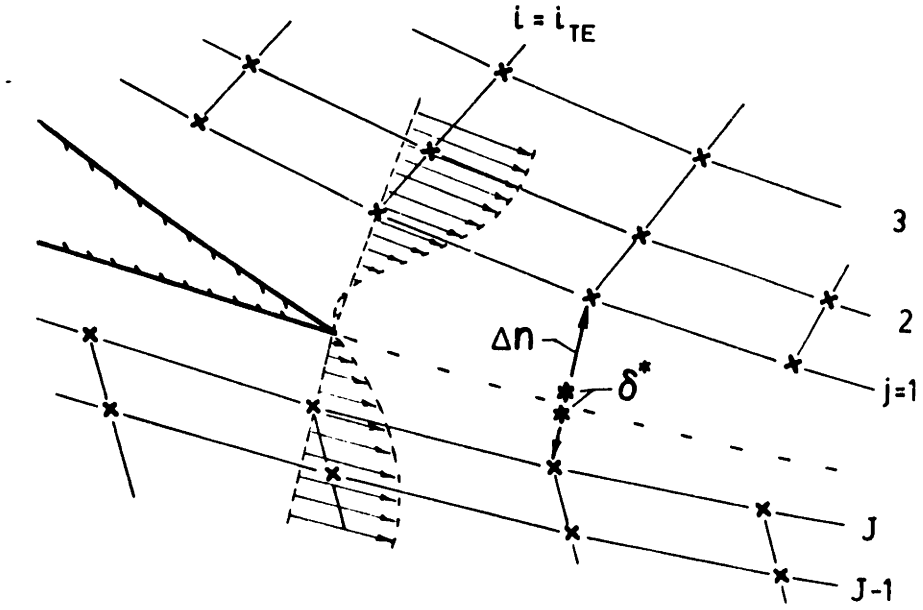

Figure 6.9 Wake displacement thickness

The only remaining coupling condition which must be satisfied is that the boundary layer edge velocity u_e used in the boundary layer equations is equal to the local inviscid velocity q at the edge of the boundary layer. The simplest approach is to take the inviscid velocities from the surface streamtube and average them to the boundary layer station, as shown in Figure 6.8.

$$u_{e_2} = \frac{1}{2}(q_i + q_{i-1}) \tag{6.60}$$

Unfortunately, the above definition for u_e is transparent to the grid sawtooth mode described in Chapter 2, and hence u_e is also transparent to the sawtooth mode in δ^*. One of the features of the boundary layer equations is that at separation they do not constrain perturbations in δ^* (this is the cause of the much-cursed separation singularity). Hence, there is nothing left to constrain the sawtooth mode in δ^* in the vicinity of separation, leading to a very ill-conditioned system of equations complete with attendant numerical instabilities. The cure to

this problem is to correct u_e in equation (6.60) for the sawtooth mode using isentropic velocity-streamtube area relations. This is completely analogous to the pressure correction in equation (2.14) used to correct the Π pressures for the sawtooth grid mode. Here, the u_e definition is modified to

$$u_{e_2} = \frac{1}{2}(q_i + q_{i-1}) + q_c \tag{6.61}$$

where
$$q_c = \begin{cases} k\, q\, M^2(M^2-1)\, \dfrac{|\vec{s}_1^{-}\times\vec{s}_2^{-}| - |\vec{s}_1^{+}\times\vec{s}_2^{+}|}{2\,|\vec{S}\times\vec{N}|} & , \quad M^2 < 1 \\ 0 & , \quad M^2 > 1 \end{cases} \tag{6.62}$$

and $q = \frac{1}{2}(q_i + q_{i-1})$, $M^2 = \frac{1}{2}(M_i^2 + M_{i-1}^2)$, $k \approx 0.2$ (6.63a-c)

The $\vec{s}$ vectors in equation (6.62) are defined by the grid as shown in Figure 2.5.

6.9 Jacobian structure modifications

Because the edge velocity u_e is defined in terms of the inviscid speed q, and the inviscid wall streamline is offset from the wall by the viscous displacement thickness δ^*, the boundary layer equations and the inviscid Euler equations are a fully-coupled system. The procedure to solve this coupled system is to modify the solid-wall boundary conditions (3.1a-b) to account for the viscous displacement, and to linearize the discrete boundary layer equations (6.52), (6.54), (6.55), and include them into the global Newton system. This necessitates modifying the Jacobian block structure described in Chapter 4.

Three discrete boundary layer equations {(6.52), (6.54), (6.55)} are associated with each streamwise node on each of the two airfoil sides. Hence, there are a total of six new equations which have to be included into each block line of the Newton system (4.16). At streamwise stations which do not have boundary layers or a wake present, namely ahead of the leading edge, dummy equations are included to maintain the same block size throughout the domain.

Figure 6.10 shows how all the variables entering the boundary layer equations are divided up between the $\bar{\bar{Z}}_i$, $\bar{\bar{B}}_i$, $\bar{\bar{A}}_i$, and $\bar{\bar{C}}_i$ blocks. In laminar regions, $C_\tau^{\frac{1}{2}}$ is replaced by the amplification ratio $\tilde{n}$.

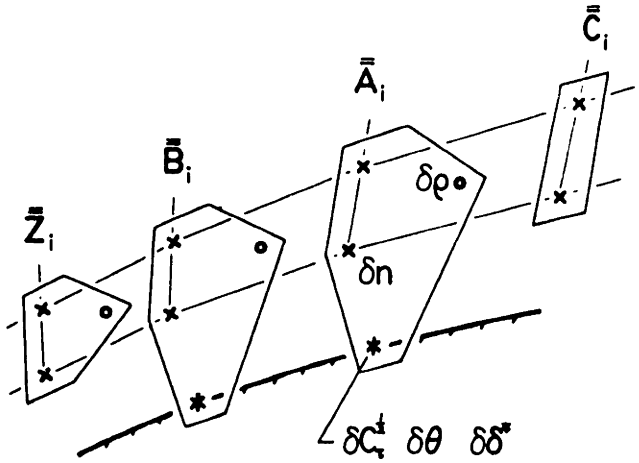

Figure 6.10 Division of boundary layer variables (turbulent) between Jacobian matrix blocks

The following pages are missing from the original

Pg. 104

The inviscid variables $\delta\rho$ and δn enter the equations because u_e is expressed in terms of the inviscid speed q which in turn is expressed in in terms of ρ and the streamline geometry. The six extra equations are placed at the bottom of each block row, and the boundary layer variable columns are placed at the right of each block. For the $\bar{\bar{A}}_i$ block, this gives the structure shown in Figure 6.11. As in Chapter 4, the δn entries are denoted by ×, and the $\delta\rho$ entries are denoted by o. The new boundary layer variable entries are denoted by * .

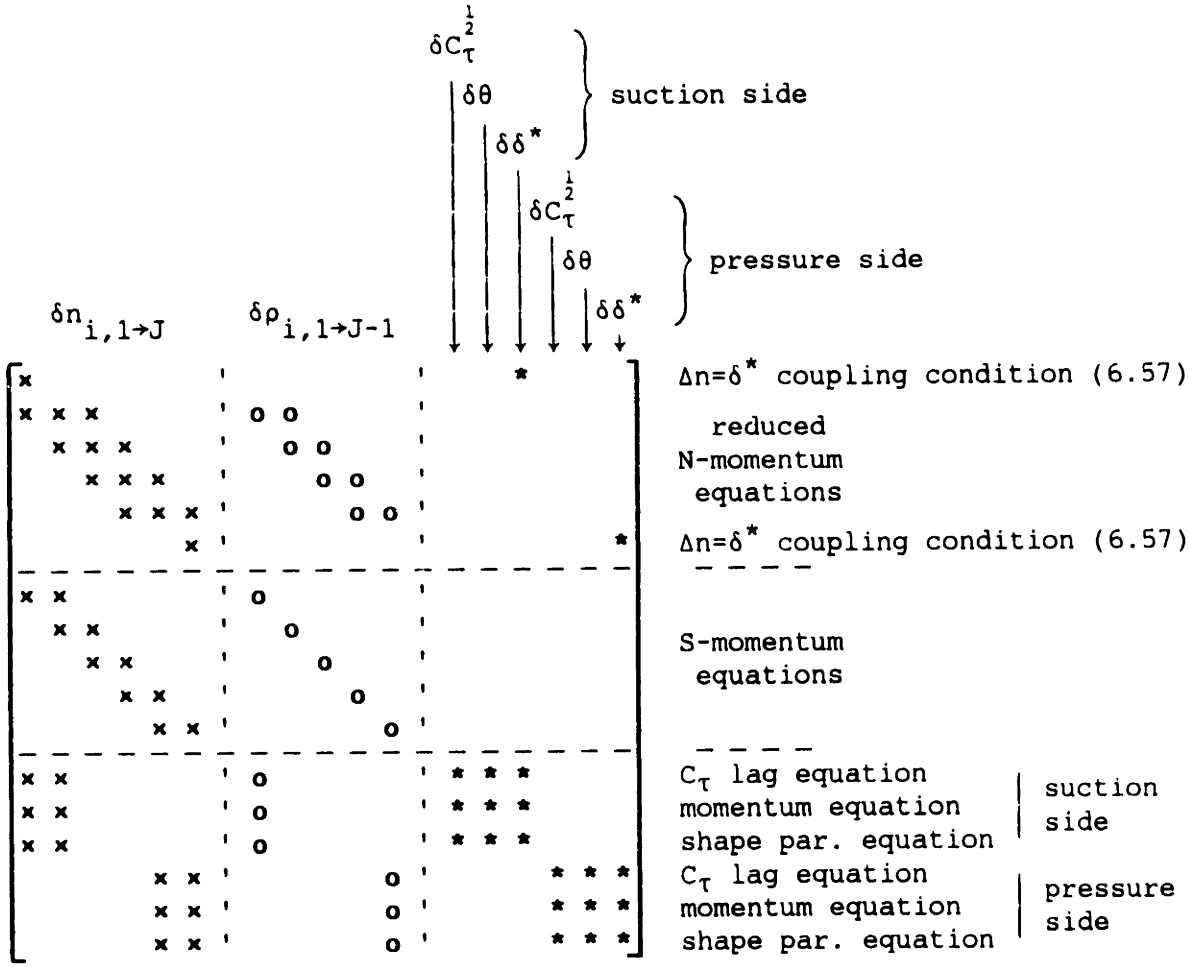

Figure 6.11 Modified $\bar{\bar{A}}_i$ block structure ($i_{LE} < i \leq I-1$)

The structure of the $\bar{\bar{B}}_i$ block is identical to that of the $\bar{\bar{A}}_i$ block shown in Figure 6.9 except for the lines labeled "$\Delta n=\delta^*$ coupling condition" being empty. The $\bar{\bar{Z}}_i$ block, in addition to having the coupling condition lines empty, also has all the boundary layer variable columns empty. The $\bar{\bar{C}}_i$ block differs from its inviscid form shown in Figure 4.4 only in having the δn entries in the additional six bottom lines.

It is important to point out that it is possible to use the boundary layer coupling formulation with the full or mixed-inverse problem. At streamwise stations where the pressure is prescribed, one or both of the linearized $\Delta n=\delta^*$ coupling condition lines in the block shown in Figure 6.11 are replaced by the usual linearized prescribed-pressure boundary condition (5.13).

6.10 Boundary layer equation linearization

The linearization procedure for the discrete boundary layer equations is essentially the same as that for the discrete Euler equations. For example, the momentum equation

$$R_m \equiv \frac{\ln(\theta_2/\theta_1)}{\ln(\xi_2/\xi_1)} - \frac{\xi_a}{\theta_a}\frac{C_f}{2} + \left(H_a + 2 - M_{e_a}^2\right)\frac{\ln(u_{e_2}/u_{e_1})}{\ln(\xi_2/\xi_1)} = 0 \qquad (6.52)$$

linearizes to

$$\left(\frac{\delta\theta_2}{\theta_2} - \frac{\delta\theta_1}{\theta_1}\right)\frac{1}{\ln(\xi_2/\xi_1)} - \frac{\xi_a}{\theta_a}\frac{1}{2}\left(\delta C_f - \frac{C_f}{\theta_a}\delta\theta_a\right) + \left(\delta H_a - \delta M_{e_a}^2\right)\frac{\ln(u_{e_2}/u_{e_1})}{\ln(\xi_2/\xi_1)}$$

$$+ \left(H_a + 2 - M_{e_a}^2\right)\frac{1}{\ln(\xi_2/\xi_1)}\left(\frac{\delta u_{e_2}}{u_{e_2}} - \frac{\delta u_{e_1}}{u_{e_1}}\right) = -R_m \qquad (6.64)$$

Since $C_f = C_f(H_{k_a}, Re_{\theta_a}, M_{e_a}^2)$, the variation δC_f is expressed as

$$\delta C_f = \frac{\partial C_f}{\partial H_k}\delta H_{k_a} + \frac{\partial C_f}{\partial Re_\theta}\delta Re_{\theta_a} + \frac{\partial C_f}{\partial M_e^2}\delta M_{e_a}^2 \qquad (6.65)$$

The variations of H_{k_a}, Re_{θ_a}, and $M^2_{e_a}$, are in turn broken down using their definitions, until only the primitive variables $\delta C_\tau^{\frac{1}{2}}$, $\delta\theta$, $\delta\delta^*$, δn, and $\delta\rho$ remain. As for the discrete Euler equations, this chain rule process is done at the Fortran level, and the details are best obtained from the program listing.

7. RESULTS

The main goal of the test cases presented here is to demonstrate the accuracy of the boundary layer coupling procedure and to prove that the inverse design algorithm works. Giles [19] has already quantitatively demonstrated the second-order accuracy of the streamtube Euler discretization scheme, and the stability and rapid convergence of the Newton solution procedure. Here, only run times will be given instead of detailed convergence histories. A Perkin-Elmer 3242 computer was used for all the calculations. This machine is roughly equivalent in performance to a VAX 11/780. The test cases are summarized below.

The first test case deals with a Joukowsky airfoil for which an exact solution is known in the incompressible limit. This case is intended primarily to investigate the effects of approximating a theoretically infinite domain with a finite computational domain.

Three test cases involve the RAE 2822 supercritical airfoil. Two will be compared with experiment to demonstrate the accuracy of the turbulent integral boundary layer formulation for transonic flow with and without shock-induced separation. The third case will demonstrate the redesign of the suction side of the 2822 airfoil using the mixed-inverse design option. This redesign eliminates wave drag and yields a 21% predicted drag reduction from the original 2822 drag.

A severe test of the performance of the boundary layer and wake formulation is afforded by a NACA 4412 airfoil being operated with substantial trailing edge stall. Comparison with experiment is given in the separated region which extends well into the wake.

The transition prediction algorithm is tested on a low Reynolds number airfoil with large transitional separation bubbles. The length of the bubbles, which critically depends on the location of transition, is compared with experiment.

The full-inverse algorithm is tested in the redesign of an empirically-derived supercritical compressor cascade. A pressure distribution which eliminates the shock is specified and the corresponding geometry is calculated.

7.1 Joukowsky airfoil

The particular Joukowsky airfoil and reference solution used for this case is derived from the incompressible potential flow around the generating circle centered at (-0.1,0.1) in the circle plane with a 4° freestream angle of attack. This configuration is then conformally mapped into the physical domain by the Joukowsky transformation. The resulting airfoil geometry was used in a series of direct Euler calculations at a freestream Mach number of 0.05 and a 4° angle of attack. The compressibility effects are below plotting accuracy, which allows a meaningful comparison with the exact solution. The distance r_∞ to the outer boundary was varied from .75 to 5 airfoil chords, while retaining a 132×32 grid. Farfield representations with and without the doublet terms were used. Five Newton iterations (15 CPU minutes) were required for each point. The resulting calculated lift coefficients are plotted in Figure 7.1.1.

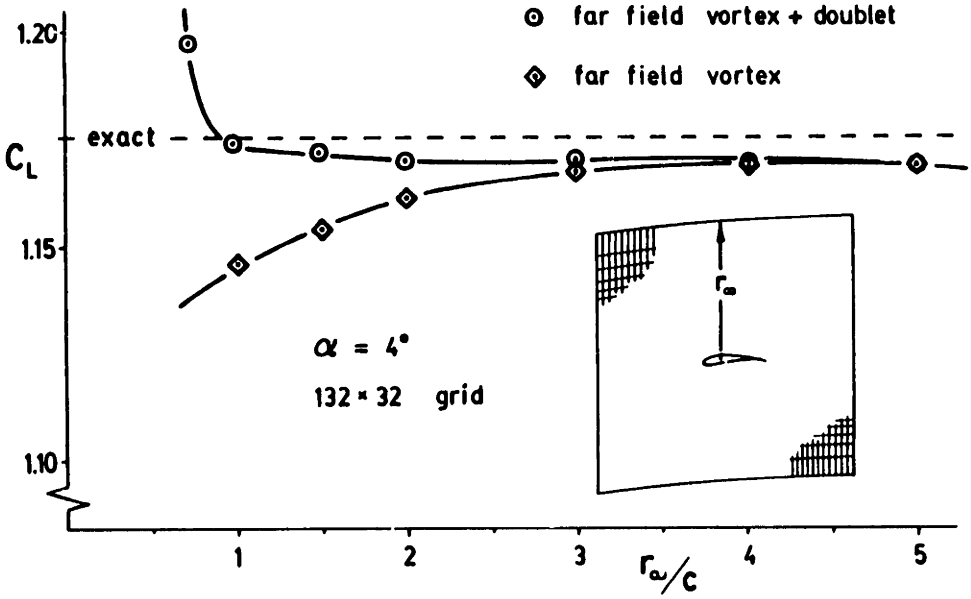

Figure 7.1.1 Effect of domain size for isolated airfoil

For the vortex-only far field representation, the lift quickly asymptotes to a value about 1/3 percent below the exact value as the distance of the outer boundary is increased. The error slowly grows again as the domain size is increased further due to the decrease in

grid resolution. With the doublet terms included, the error in lift is substantially smaller for small domains. This effect is particularly noticable in transonic cases, since the substantial transonic blockage effects are properly represented by the far field doublet. A rapid increase in the lift error occurs for the rather absurdly small domain size of $r_\infty/c < 1$, where modeling the airfoil by point singularities is certainly suspect. For the grid size used here (and the associated computational time and cost), it appears that placing the outer boundary about 2 chords away cetainly gives good accuracy if the the far field doublet is included. The calculated pressure distribution for $r_\infty/c = 2$ with the far field doublet is compared with the exact distribution in Figure 7.1.2.

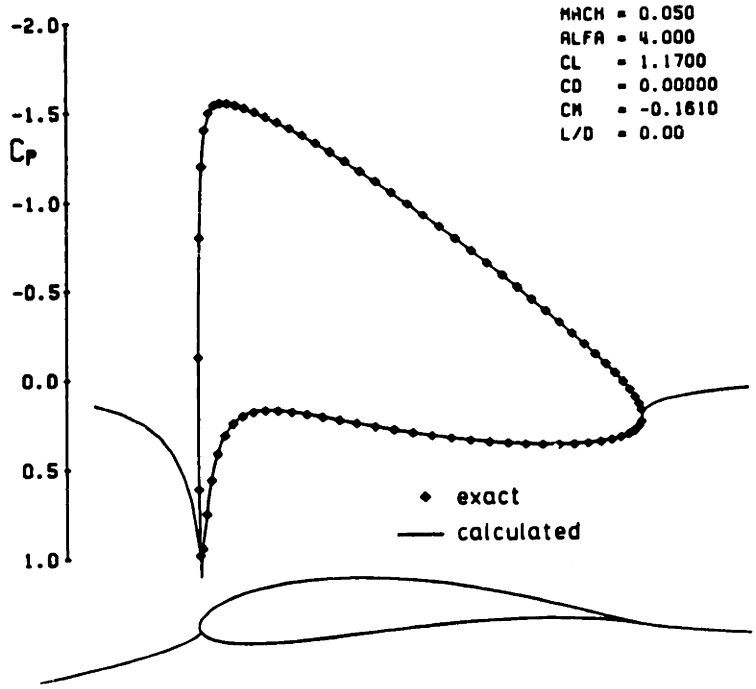

Figure 7.1.2 Calculated and exact C_p distributions for Joukowsky airfoil

The agreement is quite good. The grid near the airfoil is shown in Figure 7.1.3. The square-root pressure singularity at the trailing edge requires the extra grid resolution there. For the other airfoil cases presented here, the inlet and outlet boundaries are placed 1.5 to

2 chords away, and the streamline boundaries are placed $3/\sqrt{1-M_\infty^2}$ chords away in accordance with the Prandtl-Glauert scaling law.

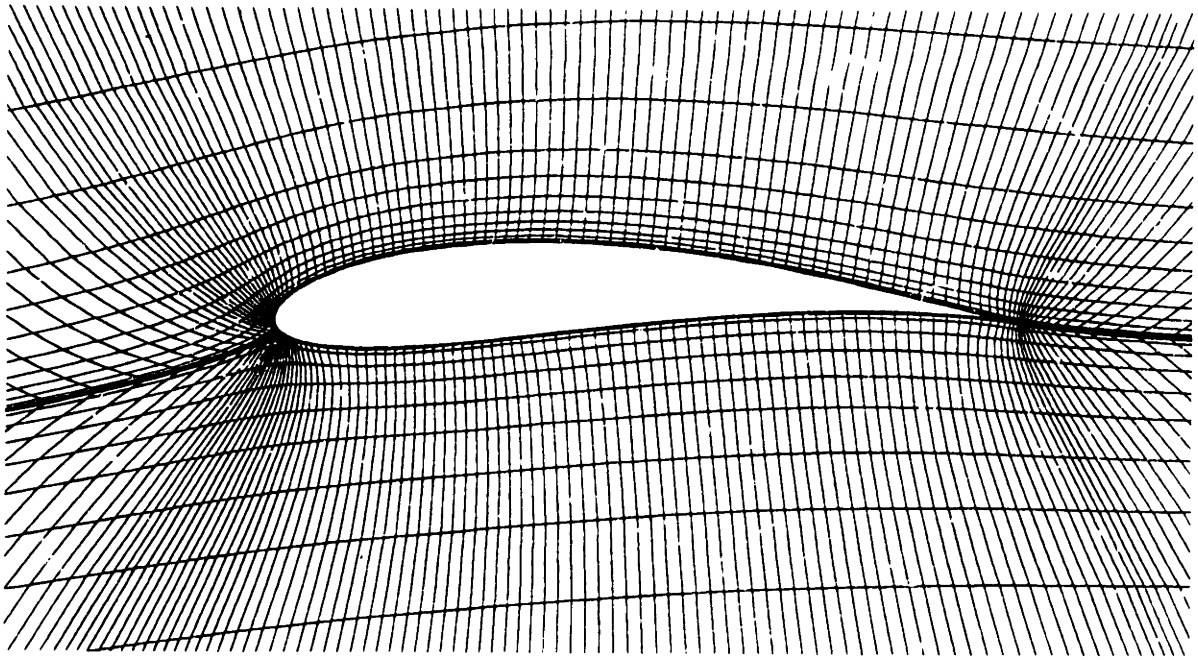

Figure 7.1.3 Converged grid near Joukowsky airfoil

7.2 RAE 2822 supercritical airfoil: fully attached flow

The RAE 2822 is a 12% thick airfoil of moderate camber with subcritical design conditions of M_∞=0.66, C_L=0.56. Experiments performed at substantially higher Mach numbers (documented in reference [12]) produced supercritical flow with a moderate-strength shock wave on the suction surface. The calculation in this example corresponds to Case 6 (M_∞=0.726, C_L=0.743) of reference [12]. Figure 7.2.1 shows the calculated viscous, inviscid, and measured pressure distributions for this case. The comparison is made at the same C_L due to uncertainties in the experimental angle of attack due to ventilated tunnel wall effects. The transition for the viscous calculation was forced at the 3% chord location on both airfoil surfaces as in the experiment.

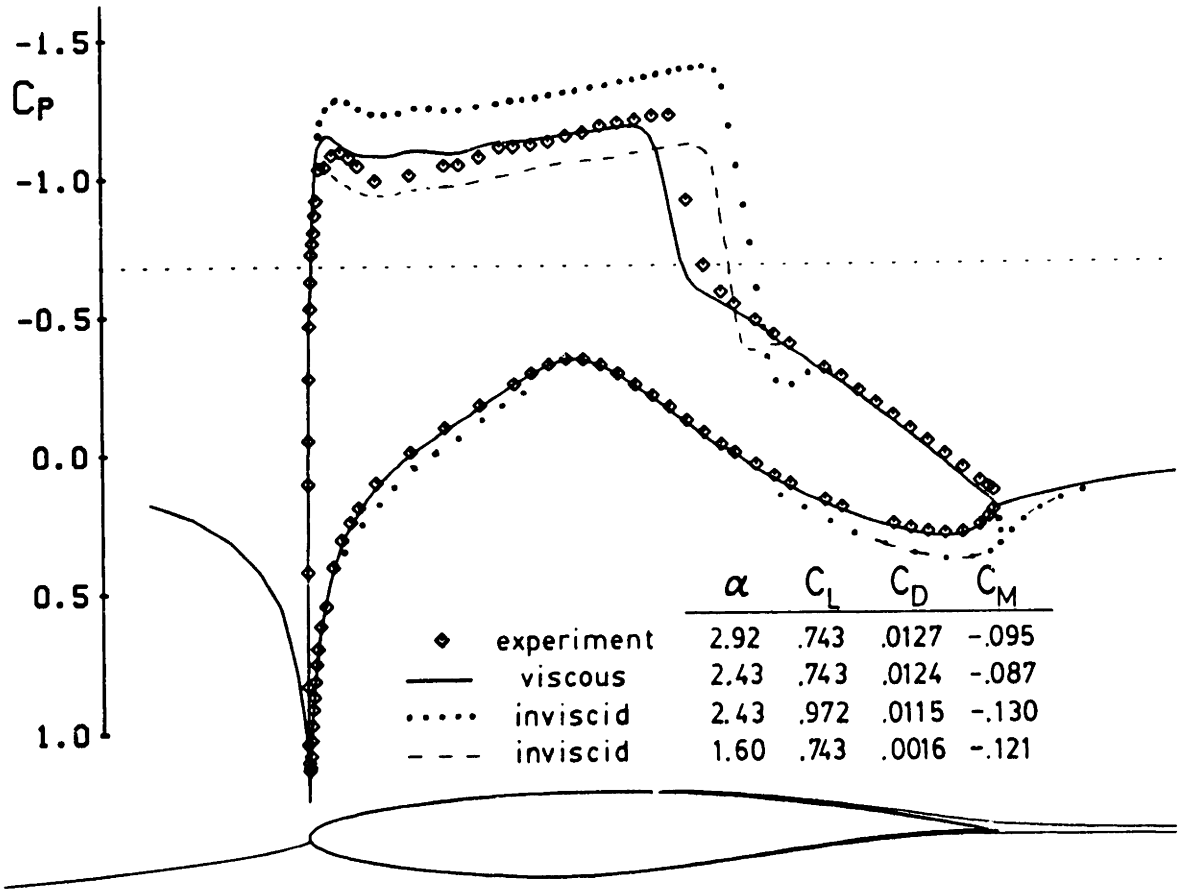

Figure 7.2.1 Calculated and experimental pressure distributions for RAE 2822 airfoil (M_∞ = 0.726 , Re = 6.5e6)

One of the two inviscid pressure distributions in Figure 7.2.1 was obtained by specifing the same C_L as the viscous case, and the other by specifying the same angle of attack as the viscous case. This comparison shows the dramatic effects boundary layers and wakes have on transonic flowfields, even at fairly high Reynolds numbers. Clearly, accounting for viscous effects substantially increases the accuracy of transonic flow predictions. The comparison of the calculated and measured boundary layer parameters is shown in Figures 7.2.2 and 7.2.3. The overall agreement is good. Ten Newton iterations (30 CPU minutes) were required for this calculation, which was performed on a 32×132 grid.

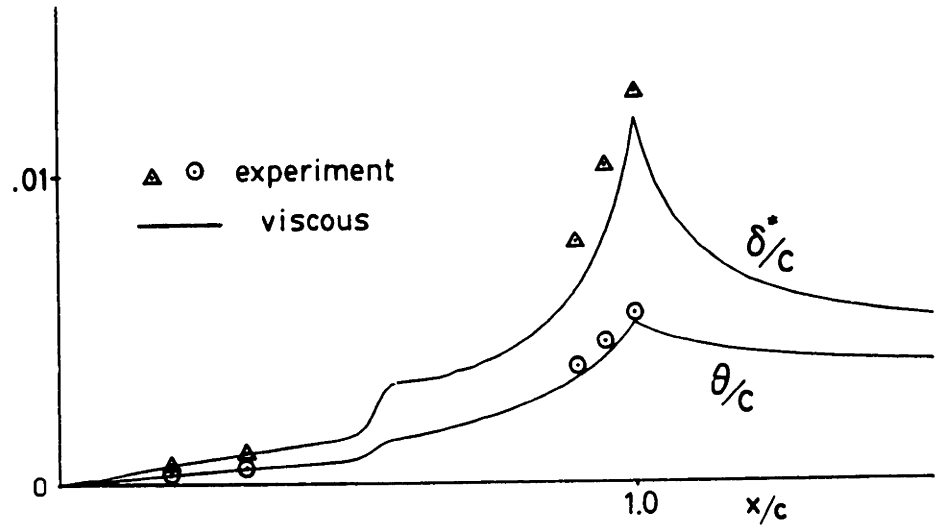

Figure 7.2.2 Measured and calculated suction suface δ^* and θ distributions for RAE 2822 (Case 6 of ref.[12])

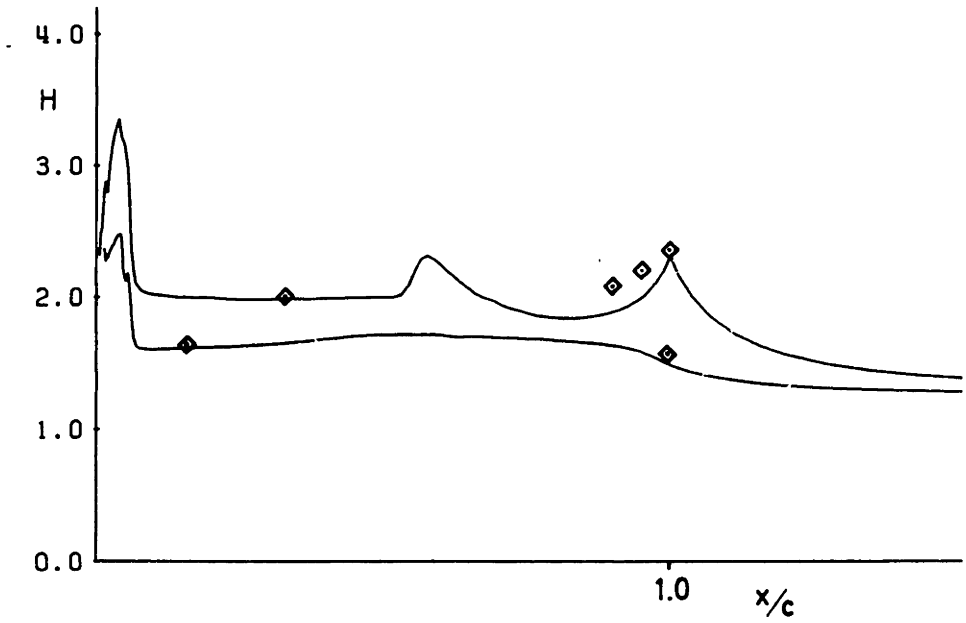

Figure 7.2.3 Measured and calculated suction and pressure surface H distributions for RAE 2822

It must be mentioned that virtually all the discrepancies between the calculations and experiments can be "eliminated" by adjusting the experimental conditions slightly. For instance, increasing M_∞ from 0.726 to 0.728 gives nearly perfect agreement for the shock position, C_D, and C_M. Since the reported uncertainty in the experimental M_∞ is ±0.001, any better comparison would most likely be fortuitous.

7.3 RAE 2822 supercritical airfoil: shock-induced separation

Case 10 of reference [12] was performed on the same experimental setup as Case 6 above. The higher value of M_∞=0.750 produced a limited separation region immediately behind the shock wave with reattachment occurring before the trailing edge. The separation was reportedly visualized by the surface oil-flow technique. Figure 7.3.1 shows the calulated viscous and measured pressure distributions.

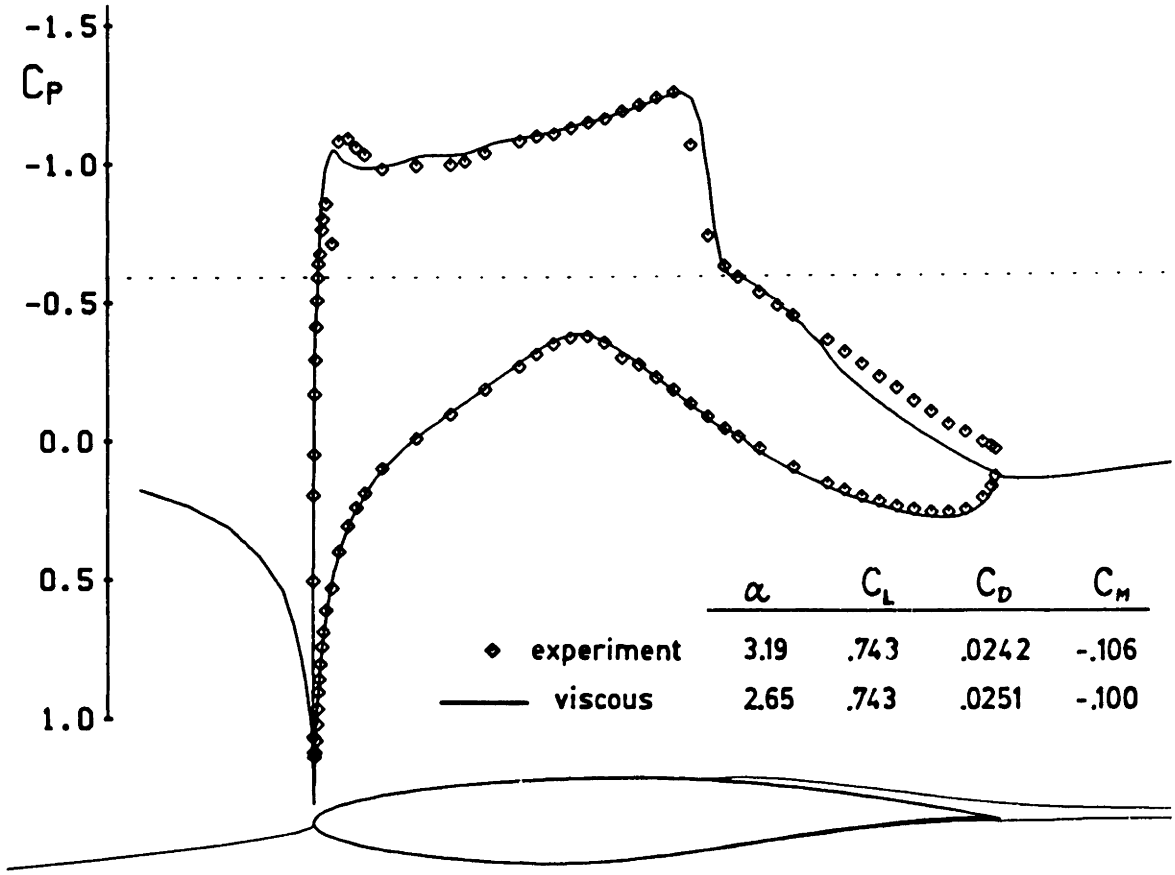

Figure 7.3.1 Calculated and experimental pressure distributions for RAE 2822 airfoil (M_∞ = 0.750 , Re = 6.2e6)

The C_D is about twice that in Case 6, meaning that here the airfoil is well past the drag-divergence Mach number. The comparison between the Case 10 experiment and the viscous calculation is quite reasonable. In particular, the drag, the boundary layer parameters, and the extent of the separation bubble are predicted quite well, as

shown in Figures 7.3.2 and 7.3.3. A close-up of the 132×32 grid (same size as for Case 6 above) is shown in Figure 7.3.4. Eleven Newton iterations (33 CPU minutes) were required for this calulation.

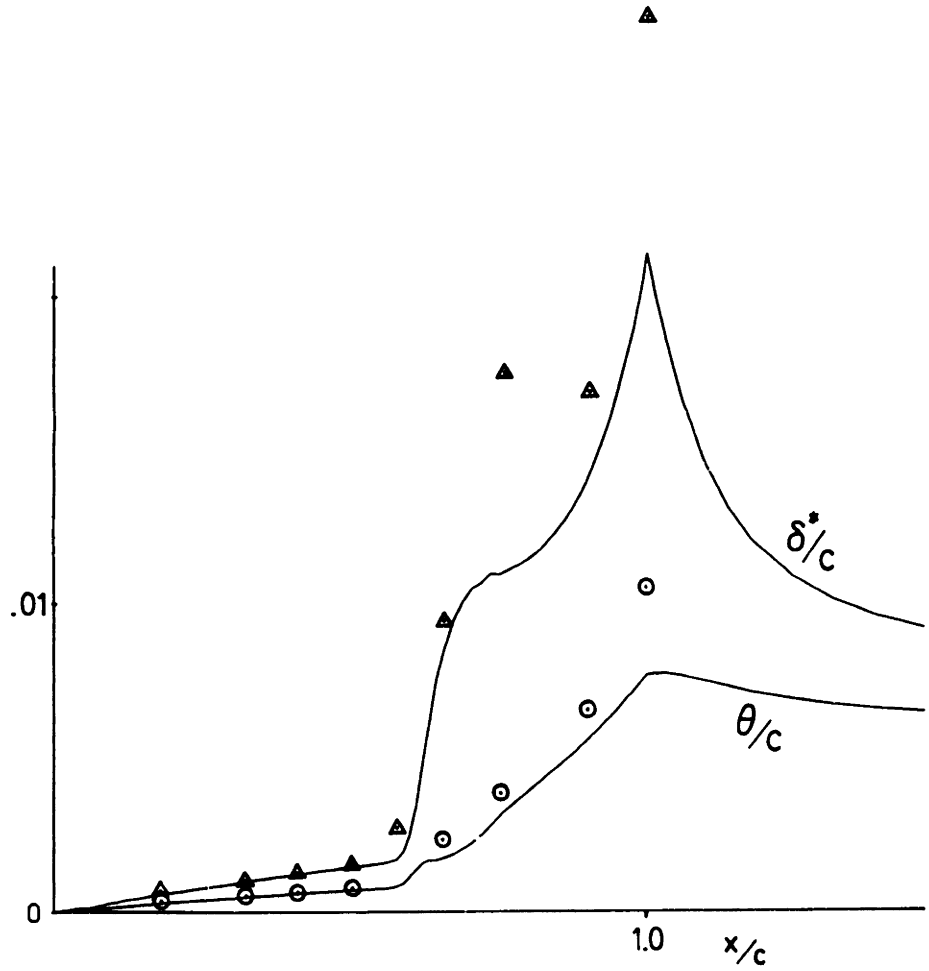

Figure 7.3.2 Measured and calculated suction surface δ^* and θ distributions for RAE 2822 (Case 10 of ref.[12])

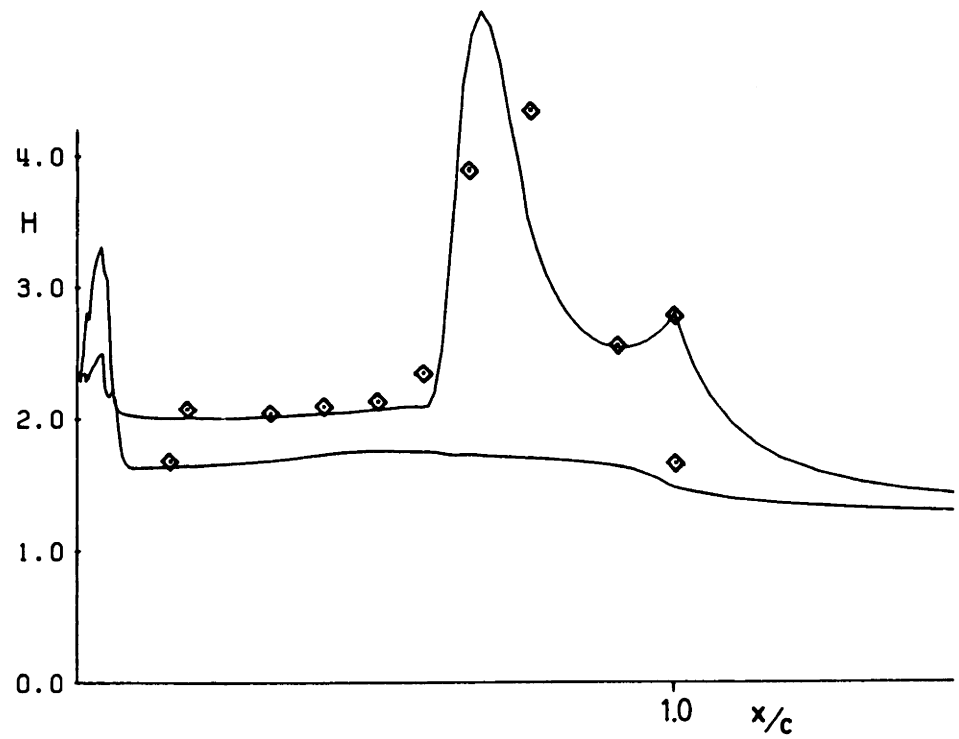

Figure 7.3.3 Measured and calculated suction and pressure surface H distributions for RAE 2822

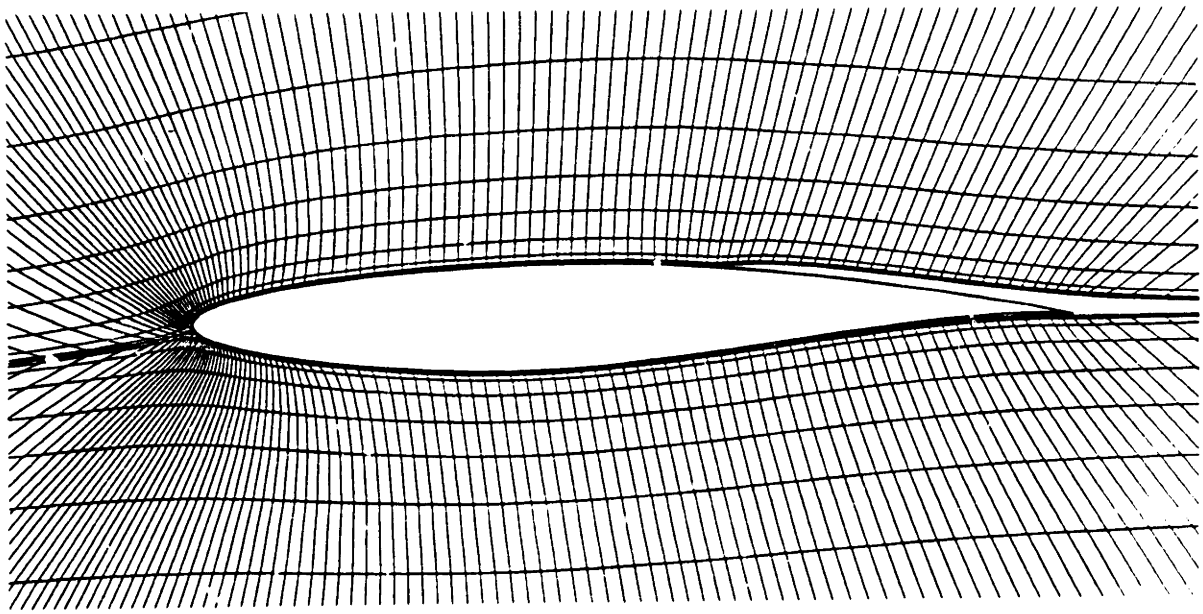

Figure 7.3.4 Converged grid near RAE 2822 airfoil

7.4 Mixed inverse RAE 2822 redesign with boundary layer coupling

To reduce the wave drag on any shocked airfoil, it is of course necessary to weaken or eliminate the shock wave in the flowfield. The RAE 2822 Case 6 was chosen as a good candidate for such a drag reduction. A mixed inverse calculation was performed with the freewall segment encompassing nearly the entire suction surface. Starting with the calculated pressure distribution obtained from Case 6 above, a smoothed-out pressure distribution was somewhat arbitrarily specified over the freewall segment as shown in Figure 7.4.1.

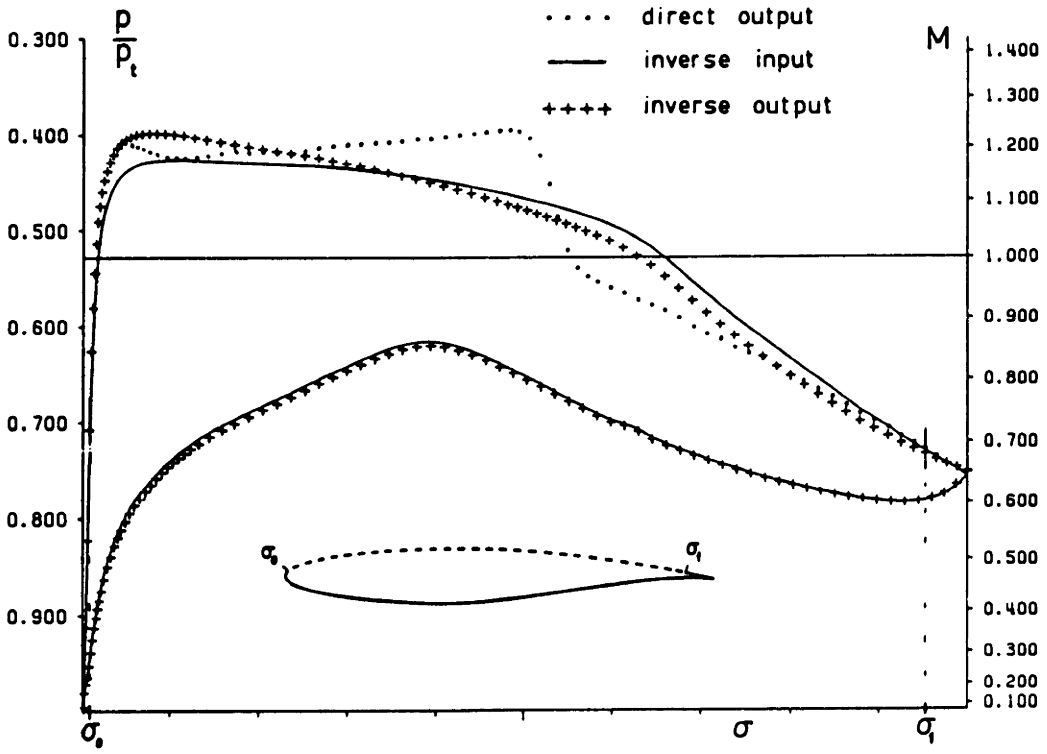

Figure 7.4.1 Pressure distributions for RAE mixed redesign

The mixed inverse calculation was started from the converged Case 6 solution, and required five additional Newton iterations (16 minutes) to converge to machine zero. The boundary layer coupling option was retained for this calculation. The resulting pressure distribution is shown in Figure 7.4.1 together with the direct and specified pressure distributions. The inverse output differs from the inverse input because of the presence of the two degrees of freedom in equation (5.7a),

which automatically modify the input pressure to achieve geometry continuity at the freewall segment enpoints. The shock has indeed been eliminated, resulting in a substantial drag reduction, as shown in Table 7.1. The freestream angle of attack was allowed to float to maintain the original lift coefficient. Figure 7.4.2 shows the geometry comparison between the original and modified airfoils, and Figure 7.4.3 shows the Mach number contours for the original and modified solutions.

Table 7.1

Comparison of original and modified RAE 2822

		Experimental RAE 2822	Computed RAE 2822	Computed modified
alpha		2.92	2.43	2.55
	C_L	.743	.743	.743
	C_M	-.095	-.087	-.086
wave	C_D		.0019	.0001
viscous	C_D		.0105	.0101
Total	C_D	.0127	.0124	.0102

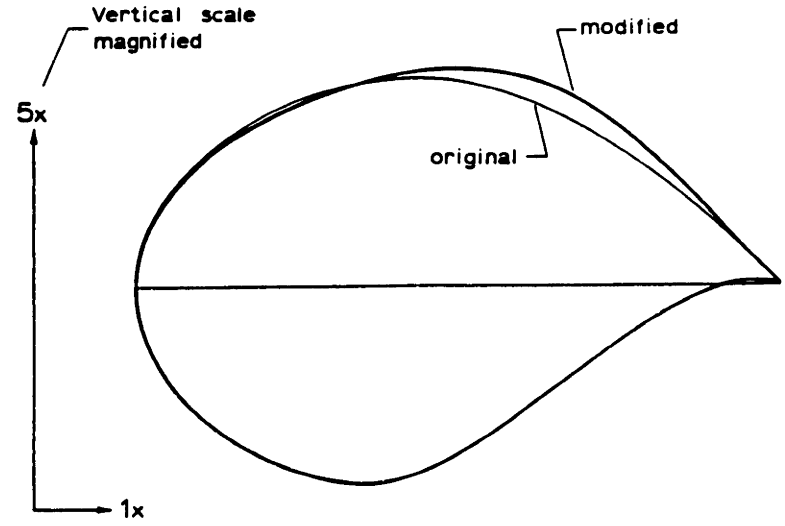

Figure 7.4.2 Comparison of RAE 2822 airfoil geometry before and after mixed redesign

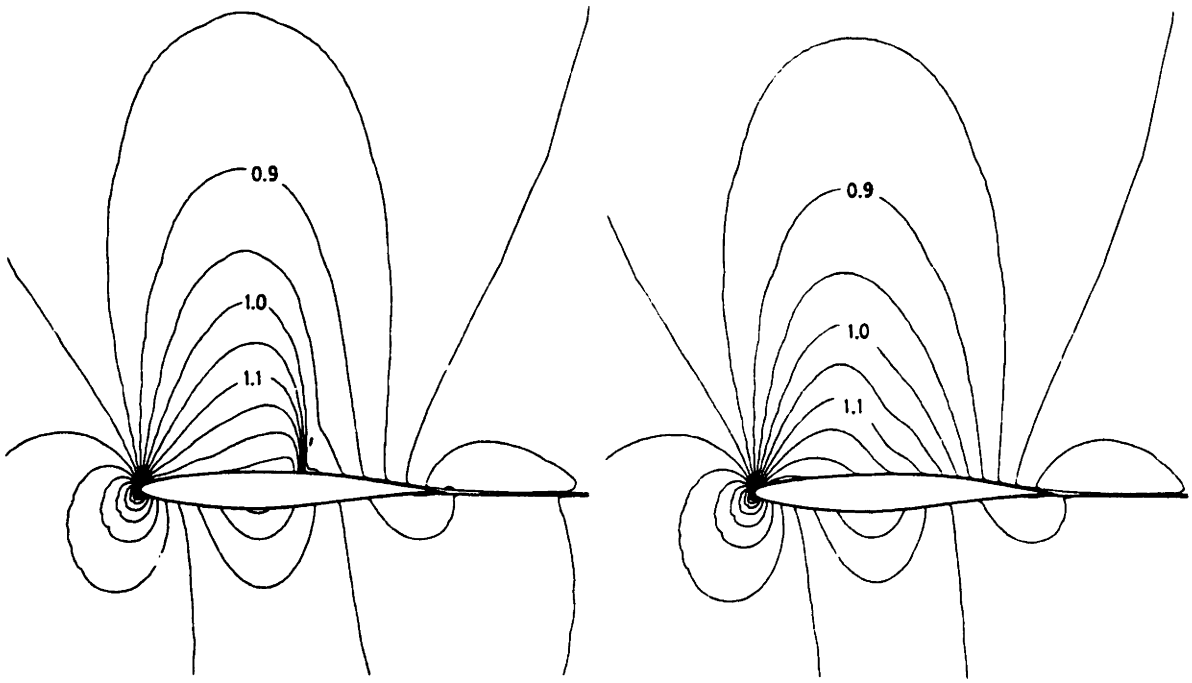

Figure 7.4.3 Mach number contours before and after RAE 2822 mixed redesign

7.5 NACA 4412 airfoil: trailing edge stall

The ability to calculate flowfields with a limited trailing edge separated region is important since as the angle of attack is increased, typical aft-loaded airfoils reach maximum lift coefficient after the trailing edge begins to stall. Reference [25] reports an experiment where detailed measurements were made of the separated boundary layer and wake on a NACA 4412 airfoil at near-maximum C_L conditions. At the experimental angle of attack of 12.15°, separation took place at about the 80% chord position. Since boundary layer parameters are to be compared, the calculation was done at an angle of attack (α = 13.8°) which matched the observed separation point. Figure 7.5.1 shows the calculated pressure distribution.

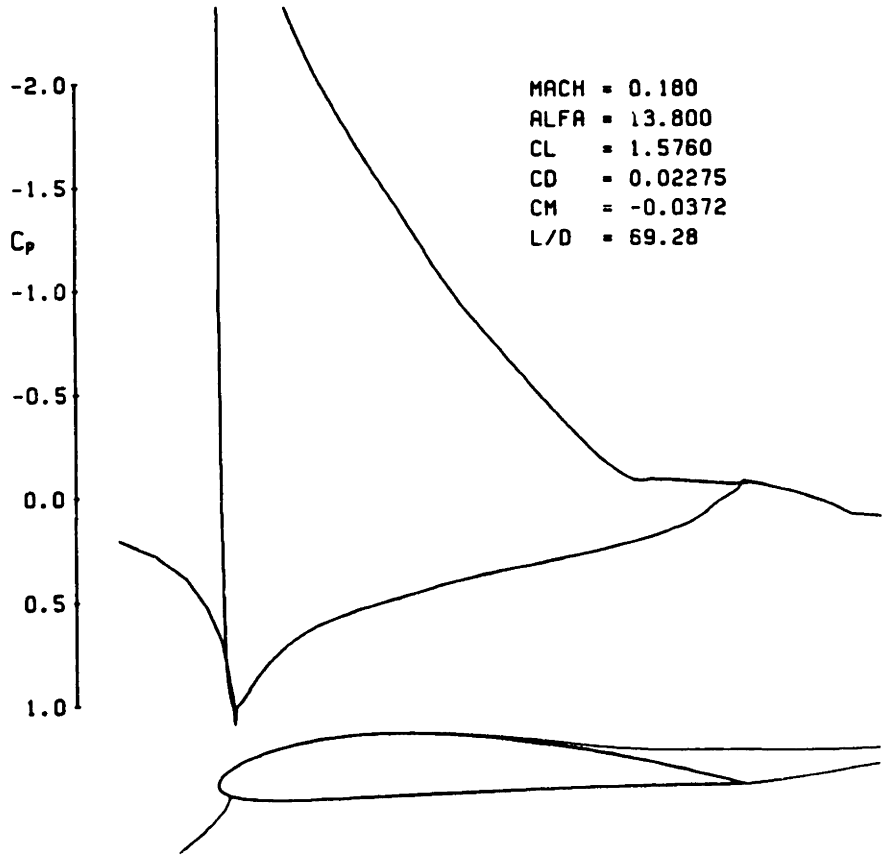

Figure 7.5.1 Computed pressure distribution for NACA 4412 airfoil

Not matching α is further justified on the grounds that separating

flows are very sensitive to disturbances, and that the reported tunnel wall corrections were quite significant. Since the separation position is fairly sensitive to disturbances, the author feels that it is a good parameter to match when making comparisons.

The computed boundary layer parameters are compared to experimental values in Figures 7.5.2 and 7.5.3.

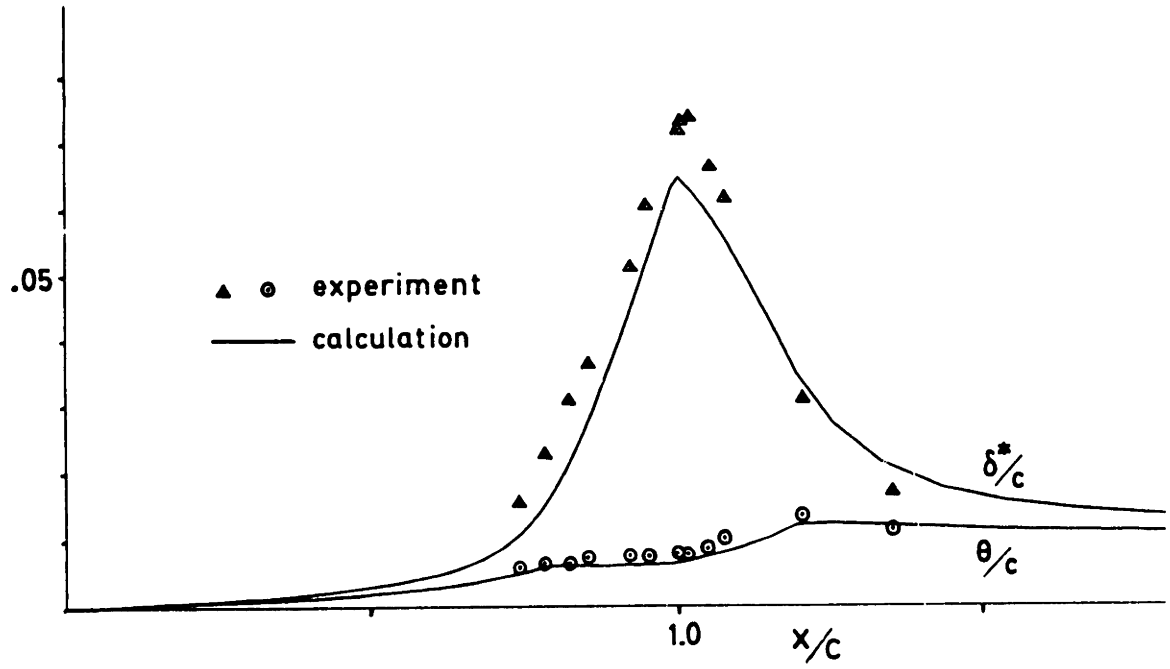

Figure 7.5.2 Calculated and measured 4412 suction surface δ^* and θ

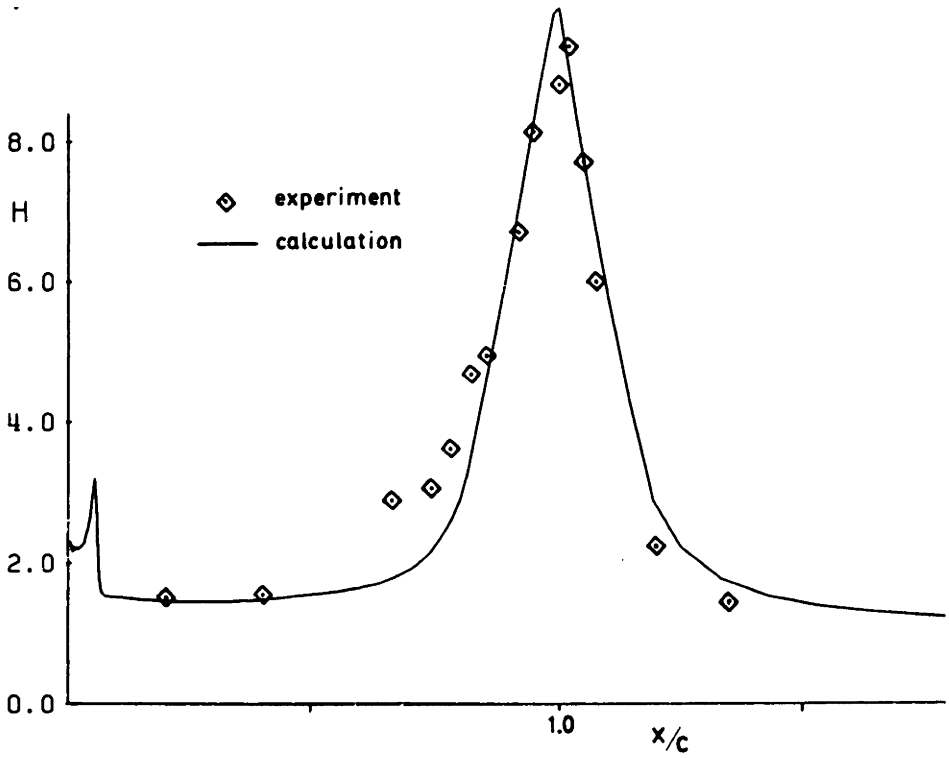

Figure 7.5.3 Calculated and measured 4412 suction surface H

The agreement with experiment is quite good, considering that the usual boundary layer approximations are rather badly strained in the separation region.

The other purpose of this case besides boundary layer verification is to demonstrate that the streamline-based grid itself is capable of accommodating large angles of attack and high leading edge edge suction peaks. Figure 7.5.4 shows the converged streamline grid in the vicinity of the airfoil. Note the large void due to the viscous displacement surface. The leading edge blowup in Figure 7.5.5 shows that the streamlines negotiate the blunt leading edge and suction peak quite well.

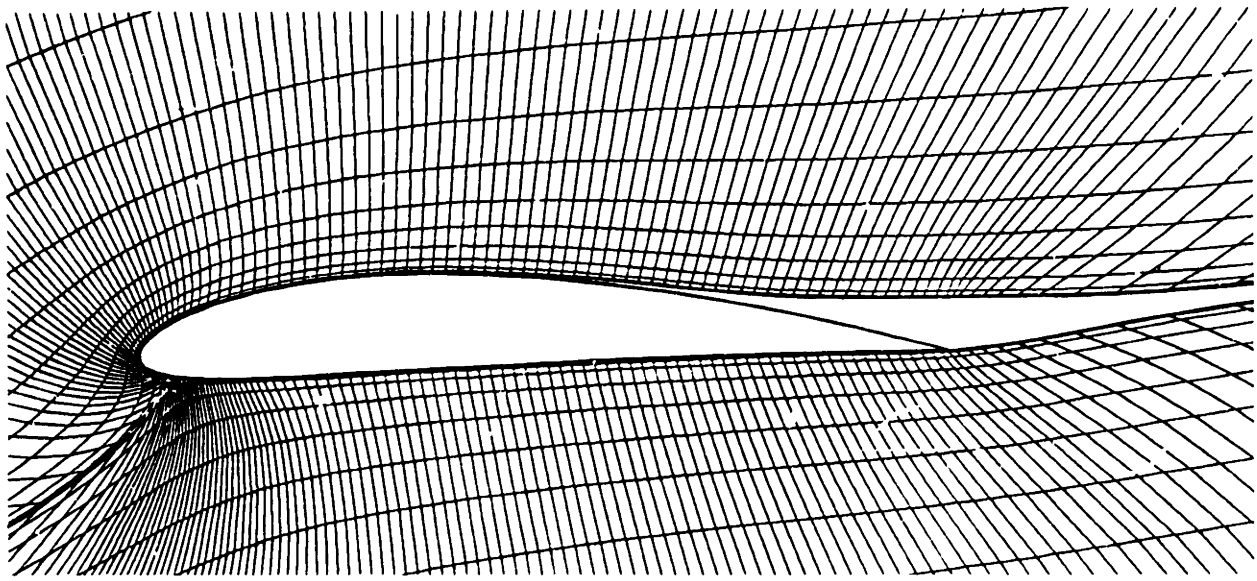

Figure 7.5.4 Converged streamline grid near NACA 4412 airfoil

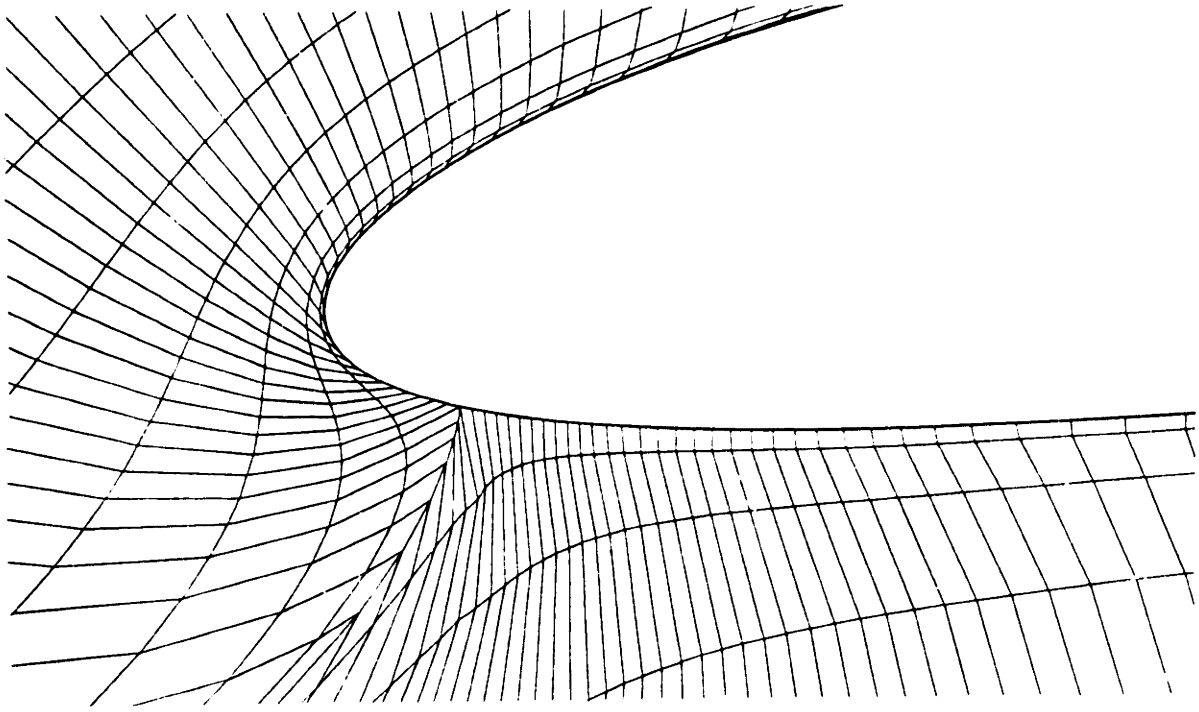

Figure 7.5.5 NACA 4412 leading edge grid detail

7.6 LA203A airfoil: Transitional separation bubbles

The LA203A airfoil is a representative aft-loaded airfoil designed specifically for low Reynolds number applications. Liebeck and Camacho [30] give detailed pressure distributions for this section obtained from an experiment in a low-turbulence wind tunnel. Profile drag was by the usual wake-traverse method. A calculation was performed for one particular experimental run at a chord Reynolds number of 250,000 and a lift coefficient of 1.08. The low Reynolds number resulted in extensive laminar separation bubbles on both sides of the airfoil. A separation bubble is very clearly discernable from a surface pressure distribution since it induces a pressure plateau which is terminated by a very strong adverse pressure gradient region at reattachment. Figure 7.6.1 shows the measured and calculated pressure distributions.

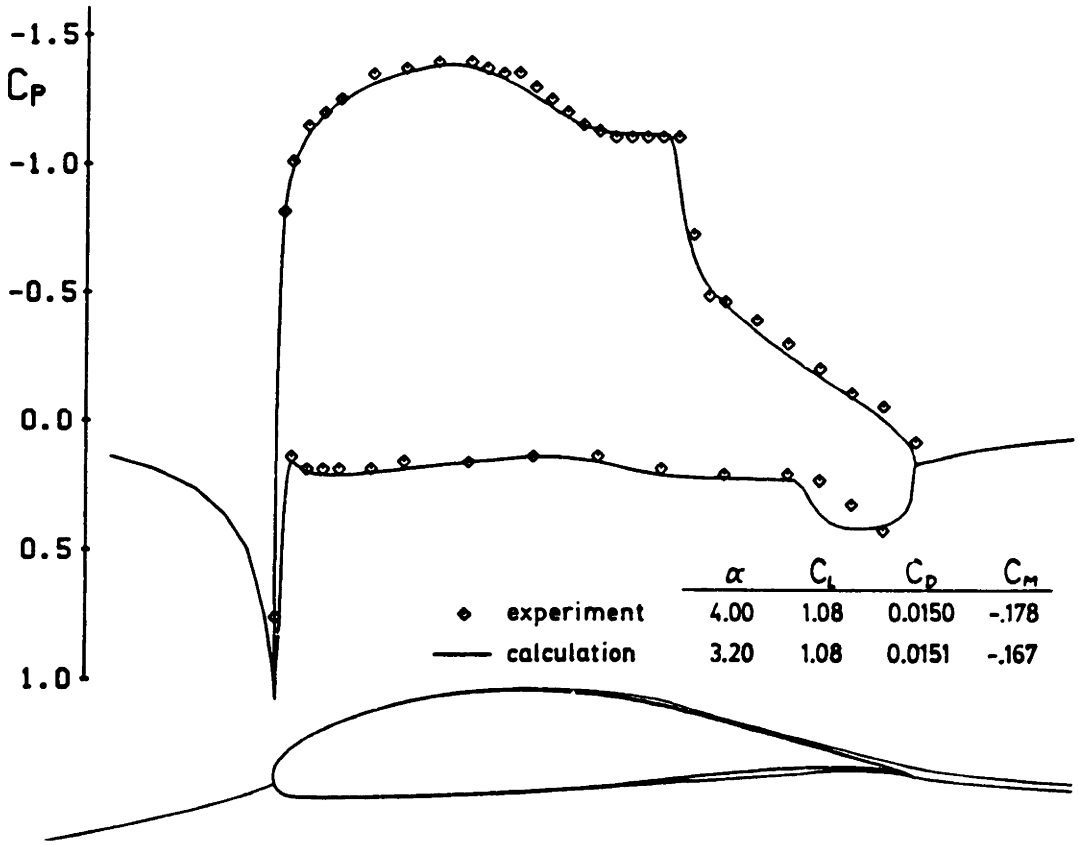

Figure 7.6.1 Calculated and experimental pressure distributions for LA203A airfoil (M_∞ = 0.100 , Re = 250,000)

The transition prediction algorithm determined the point of transition in the calculation. In both the suction and pressure surface boundary layers this occurred at the end of the separation bubbles, quickly forcing reattachment and thus setting the bubble length. As can be seen in Figure 7.6.1, the bubble lengths are predicted quite accurately, in particular on the suction side, implying that the transition location was accurately predicted. Another important point to note is that the drag and moment coefficients are also accurately predicted. The nearly exact agreement of the drag coefficient is better than might be expected, since the very low Reynolds number puts into question the turbulent closure relations presented in Chapter 6.

Entire drag polars at Re = 250,000 and Re = 375,000 were also performed for the LA203A airfoil and compared with experimental polars in Figure 7.6.2. The comparison is quite good, with maximum C_L values being accurately predicted.

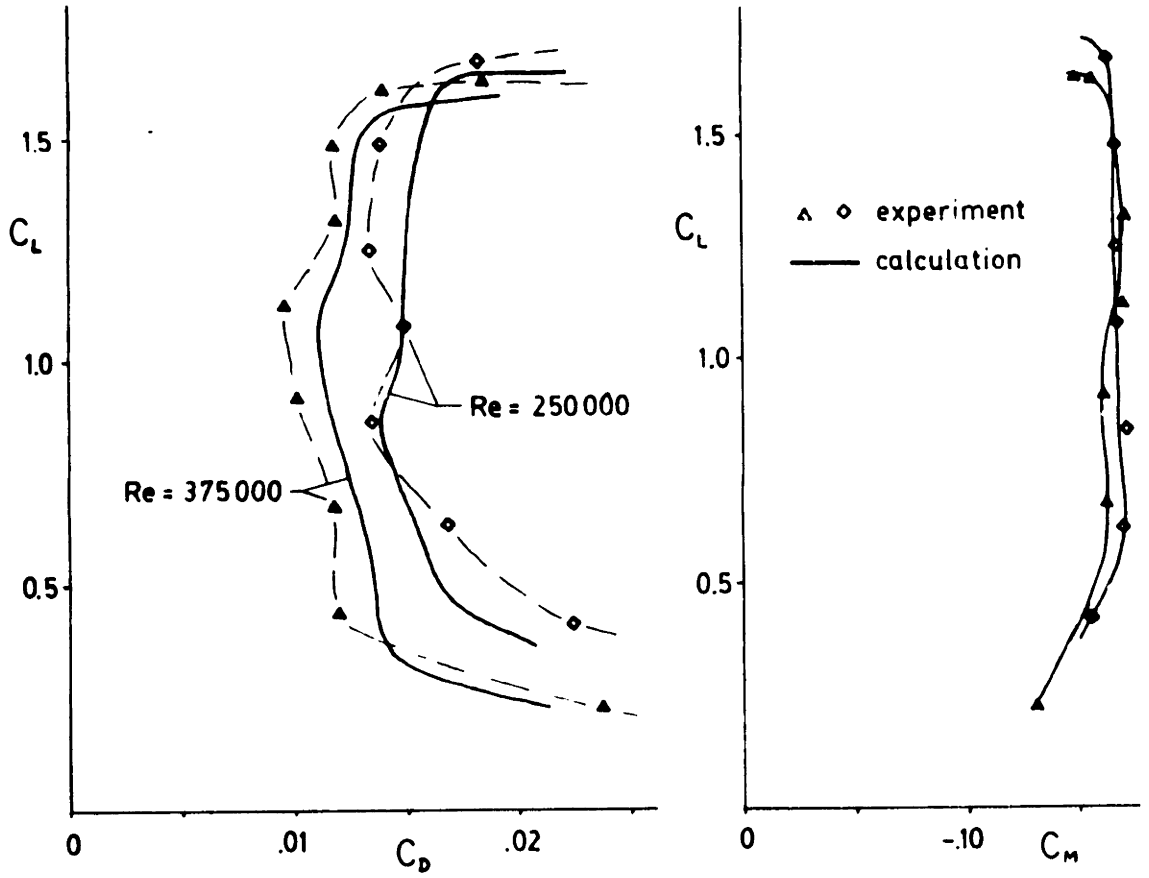

Figure 7.6.2 Calculated and experimental drag polars of LA203A airfoil

7.7 Supercritical cascade: Full-inverse redesign

This case is intended to demonstrate the ability of the full-inverse design option to redesign an originally shocked cascade such that shock-free operation is obtained. The base shocked solution was obtained by first "designing" a reasonable-looking compressor airfoil by the French curve method, and calculating a direct inviscid solution for an inlet Mach number of 0.7. The solution required seven Newton iterations (10 CPU minutes) to converge. Figure 7.7.1 shows part of the 25×122 grid used in the calculation. A supersonic region with a peak Mach number of 1.42 and terminated by a strong shock wave occurred on the suction surface. Figure 7.7.2 shows the calculated Mach number contours.

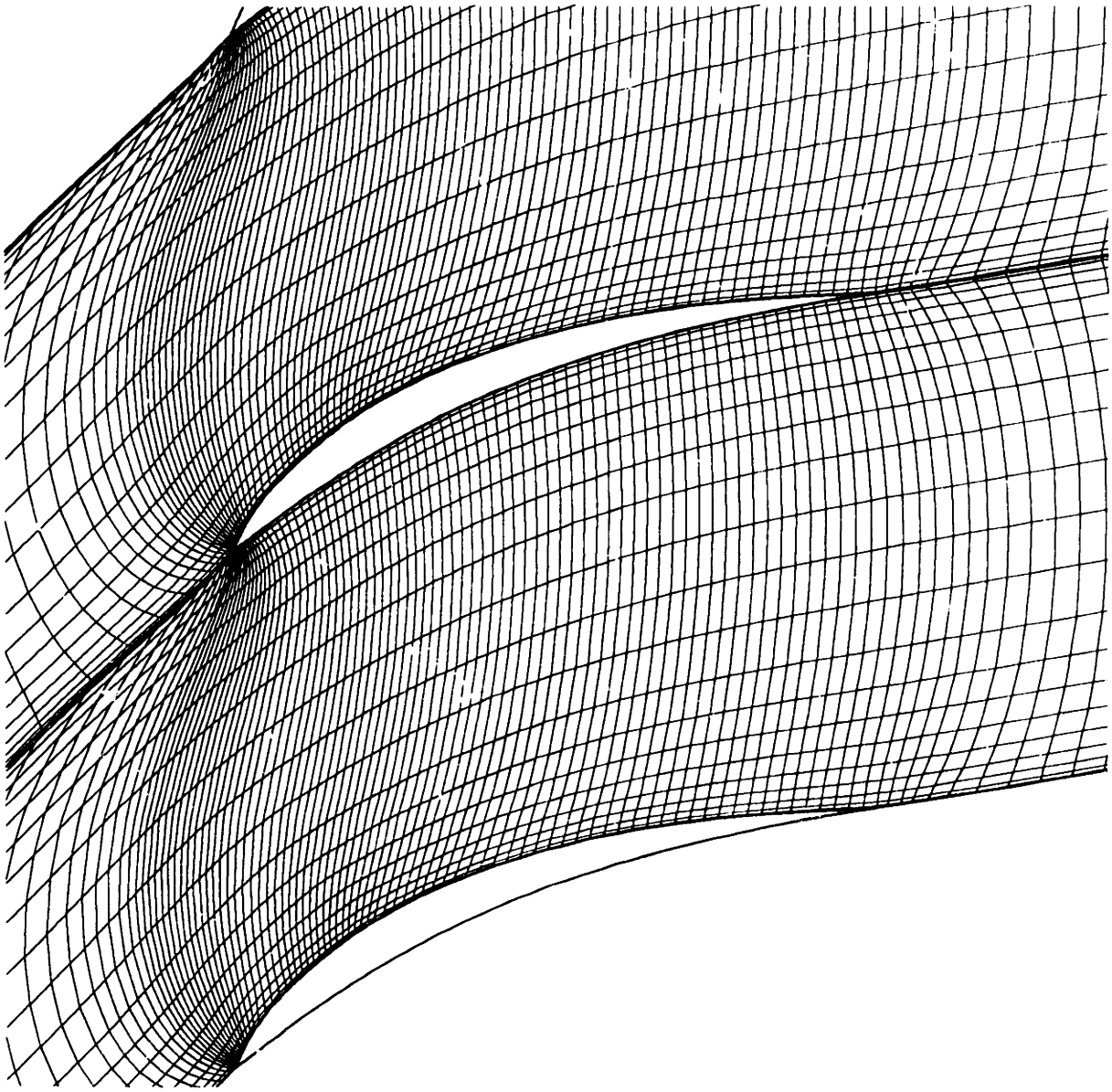

Figure 7.7.1 Grid used for supercritical cascade

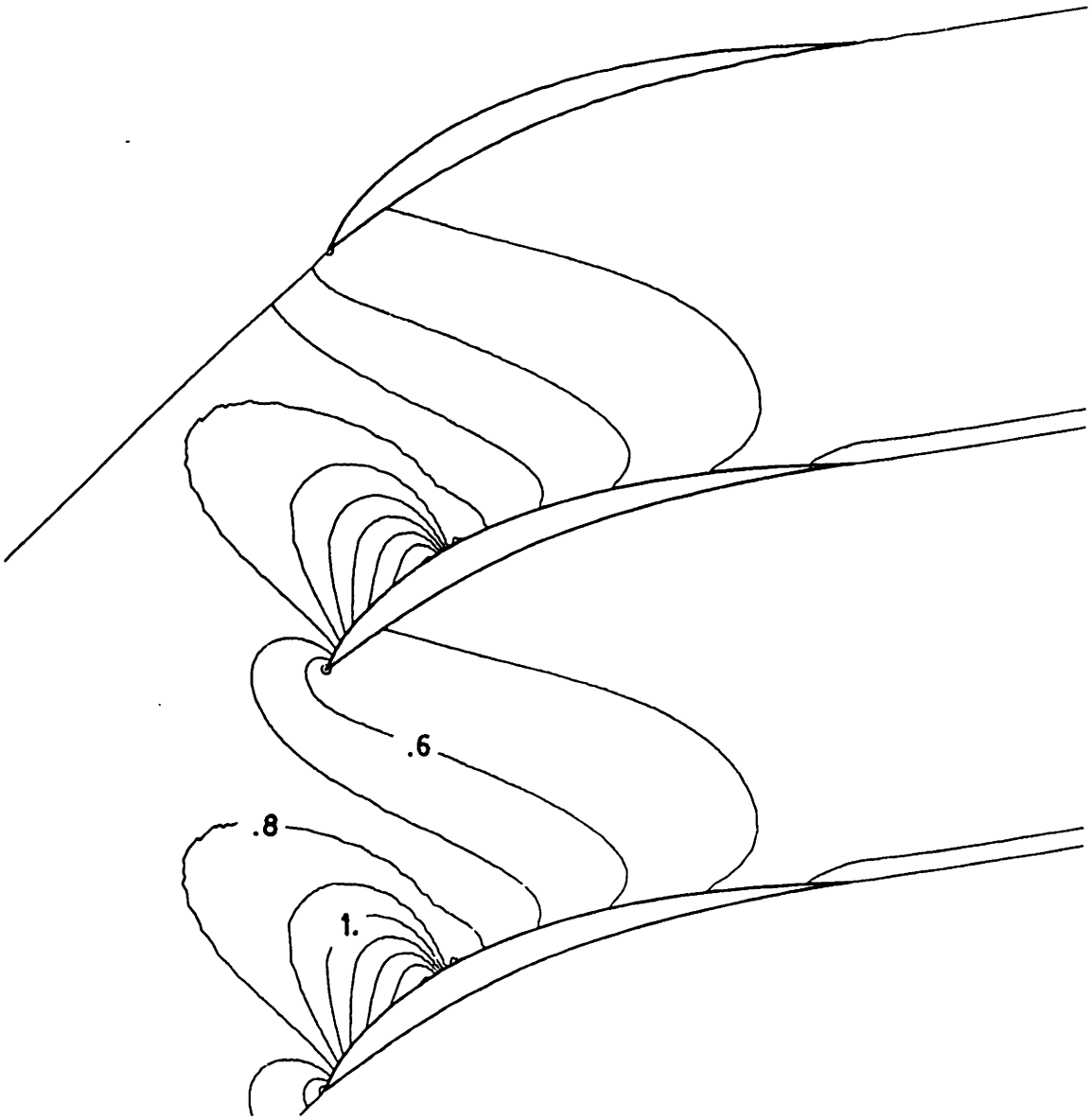

Figure 7.7.2 Mach number contours for direct calculation

To eliminate the shock, a smoothed-out pressure distribution was specified on the suction surface of the cascade airfoil and input into the full-inverse option. The pressure specified on the pressure surface was the same as that resulting from the direct calculation. The inverse input and output distributions are shown in Figure 7.7.3 together with the original direct output distribution. The inverse input and output differ because of the free parameters which were introduced into the specified pressure distribution (5.5a-b) to enforce leading

and trailing edge closure. An additional free parameter was also introduced so that the global constraint of an invariant blade lift (i.e. stage work) could be imposed. The inlet conditions were also held fixed.

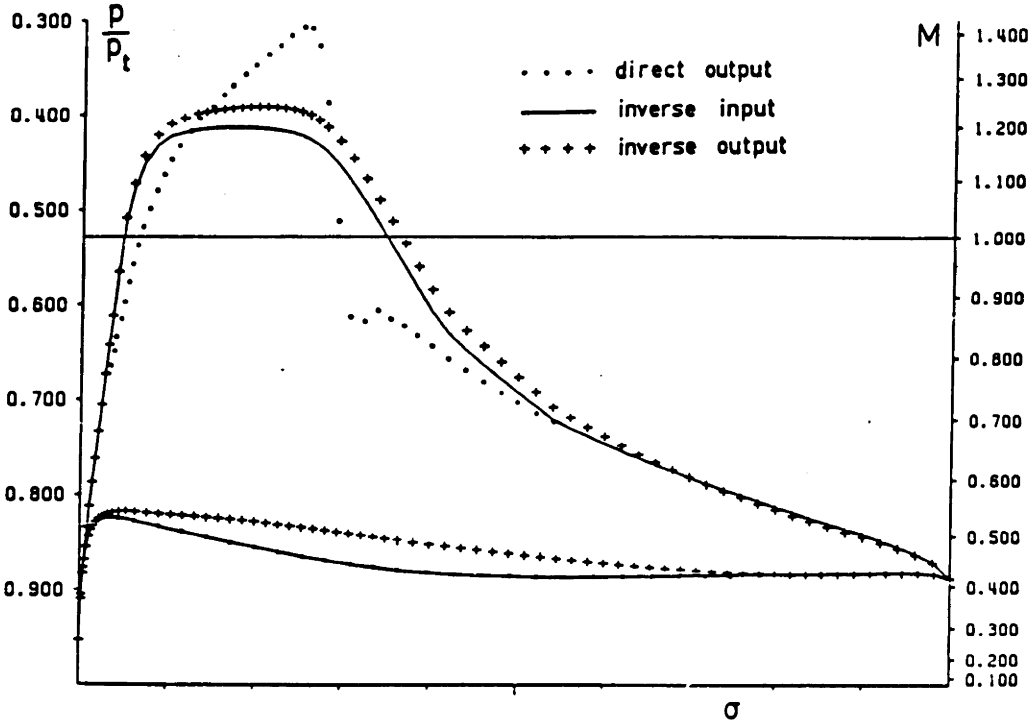

Figure 7.7.3 Pressure distributions for cascade redesign

Figure 7.7.4 shows the new cascade airfoil geometry and computed Mach numbers resulting from the inverse calculation, which was restarted from the direct solution and required four additional Newton iterations (5 CPU minutes) to converge. Note that the shock is completely absent.

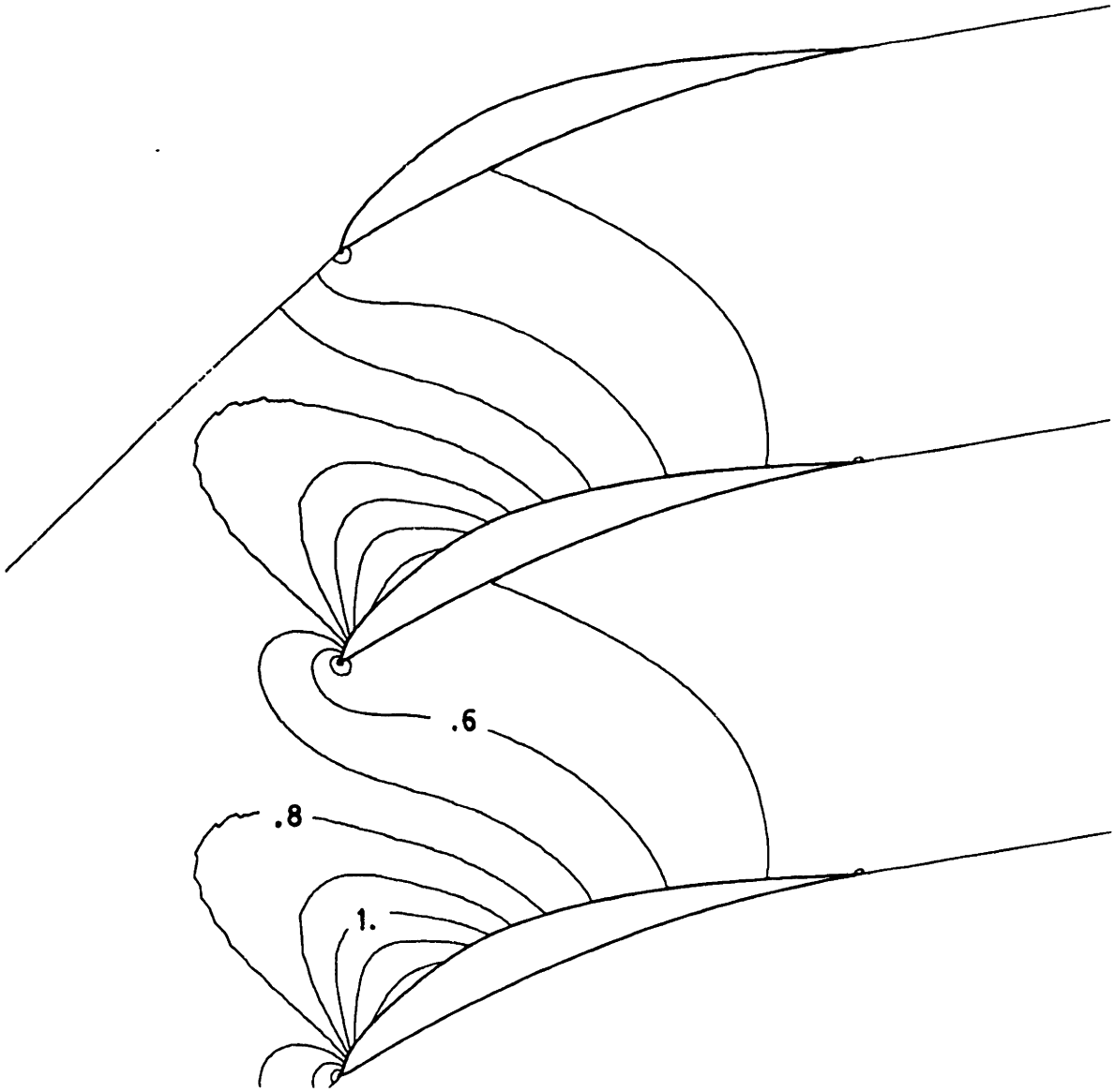

Figure 7.7.4 Mach number contours for redesigned cascade

The original and new cascade airfoil geometries are compared in Figure 7.7.5. An unintentional favorable result of the inverse calculation is that the new blade is substantially thicker than the original, and thus would be more structurally favorable. In principle, a cross-sectional area or bending moment of inertia could be imposed explicitly as a global constraint. Of course, an additional free parameter and shape function would have to be added to the prescribed pressure distribution (5.5a-b) for each new constraint, so that the

resulting inverse problem remains well-posed.

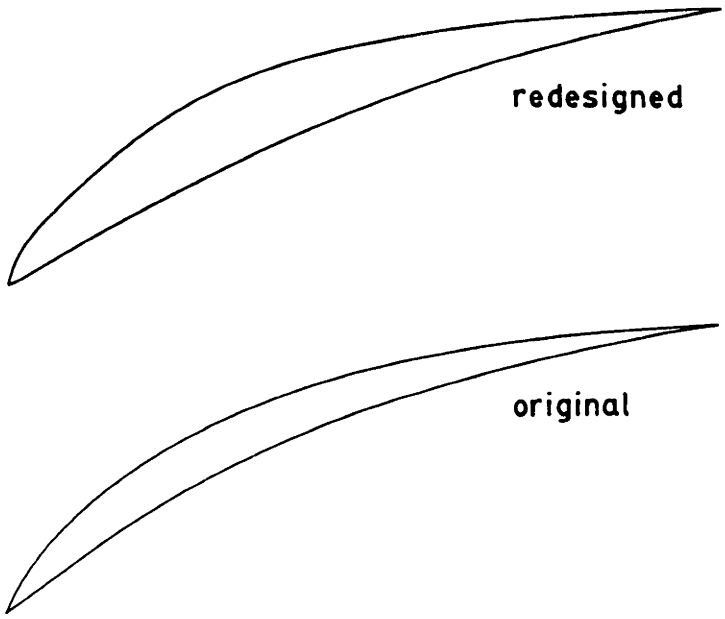

Figure 7.7.5 Original and new cascade airfoil geometries

8. CONCLUSIONS

8.1 Euler equation discretization

This thesis develops a method of discretizing the steady Euler equations on an intrinsic streamline grid. Such a coordinate system has many attractive features not found in conventional fixed grids. The mass and energy equations are replaced by t' mple algebraic conditions of constant mass flux and total enthalpy along each streamtube. Only the momentum equations need to be solved, giving computational economy. Another feature of a streamline coordinate system is that there is no numerical diffusion of entropy or enthalpy; signals propagate between streamtubes only via streamline geometry and the pressure field. Furthermore, only physical boundary conditions are required to close the discrete equation set. Numerical boundary conditions are unnecessary. Streamline coordinates have been employed previously by the streamline curvature methods, which solve the Euler equations in differential form and hence do not treat shocks properly. The present formulation solves the Euler equations in integral form which ensures the proper Rankine-Hugoniot shock jumps in the limit of infinite grid resolution.

8.2 Inverse problem formulation

The present streamline-based discretization of the steady equations permits the usual solid-wall boundary condition to be easily replaced by an inverse boundary condition, where the surface pressure is prescribed instead. The body geometry then deforms to achieve the specified pressure. Closure and geometry continuity constraints are rigorously enforced through the introduction of free parameters into the prescribed pressure distribution. Discrepancies between the specified and calculated pressure distributions resulting from the free parameters are typically sufficiently small so as not to impair the effectiveness of the design algorithm. Both the mixed-inverse and full-inverse problems have been formulated and tested on airfoil and

compressor cascade geometries. The airfoil redesign was aimed at the elimination of shock waves in the flowfield with the lift coefficient and freestream conditions held fixed. This goal which was achieved, resulting in a predicted 21% profile drag reduction. The compressor cascade redesign was also aimed at shock wave elimination under the constraint of fixed stage work. This goal was also achieved, eliminating shock losses and incidentally producing a substantially thicker airfoil.

8.3 Compressible integral boundary layer formulation

The compressible boundary layer formulation developed in this thesis makes use of the standard disspation closure, meaning that the integral momentum and kinetic energy equations are used to describe the streamwise evolution of the boundary layer parameters. The laminar closure relations used in the present formulation are based on the Falkner-Skan family of profiles. For turbulent flow, the very important dissipation coefficient correlation is derived directly from the dissipation equation and the experimental G-β locus. The more common approach of assumed profiles and eddy-viscosity models is not required. It is shown that the resulting dissipation function still has the same form as that derived from assumed profiles. Excellent accuracy of the laminar formulation is demonstrated by comparison with an effectively exact finite difference calculation. The accuracy of the turbulent formulation for attached and separated flows is demonstrated by comparisons with experiments.

The implementation of the present boundary layer formulation uses the common e^9 transition prediction method. Disturbance amplification rates are integrated downstream from the point of instability until some empirically derived critical amplification factor is reached, at which point transition occurs. The amplification rates are integrated with respect to the physical streamwise coordinate. It is argued that this is more physically realistic than the more commonly used integra-

tion with respect to momentum thickness Reynolds number. In the present formulation, the critical Reynolds numbers and amplification rates are derived from finite-difference solutions to the Orr-Sommerfeld equation using the Falkner-Skan profiles. From these solutions, simple algebraic expressions for the critical Reynolds number and amplification rates are obtained. The transition prediction algorithm is tested in a calculation of a low Reynolds number airfoil with large transitional separation bubbles. The bubble lengths, which critically depend on the location of transition, are accurately predicted.

8.4 Boundary layer coupling formulation

The boundary layer formulation derived in this thesis is interacted with the inviscid flow via the displacement thickness using a novel calculation procedure. All other current interaction calculation methods involve iteration between the viscous and inviscid solvers using some approximate model for the viscous flow in the inviscid calculation and vice versa. The present formulation dispenses with such iteration altogether by simply solving the interacted inviscid and viscous equations as a fully-coupled system. This is a robust procedure which permits the calculation of strong interaction problems such as trailing edge stall, shock-induced separation, and transitional separation bubbles. The additional CPU time required for a viscous calculation is only a small fraction of the time required to perform a purely inviscid calculation. Furthermore, the viscous option can be retained with the full-inverse or mixed-inverse boundary conditions, permitting viscous effects to enter into design calculations.

8.5 Newton solution procedure

The discrete steady Euler equations, boundary conditions, discrete boundary layer equations, coupling conditions, and global constraints are all solved simultaneously as a fully-coupled system by the Newton method. This thesis describes a chain-rule-based linearization process which makes solution of such a large and complex system by the Newton

method feasible. The thesis also describes a treatment of the global constraints which preserves the orderly structure of the large Newton system and thus simplifies its solution. The demonstrated speed of the Newton solution procedure makes it at least as fast as state-of-the-art time-marching Euler solvers for airfoils, and substantially faster for cascades. Since the viscous and design options do not significantly add to the computation time, and small input changes yield quadratic convergence, it is felt that the current design/analysis system as a whole is unparalleled in speed. The possibility of rapid interactive execution on a minicomputer, plus the ease of switching between analysis and design modes and enforcement of arbitrary global constraints all significantly add to the effectiveness of a designer.

References

[1] Bauer,F., Garabedian,P., Korn,D., Jameson,A., "Supercritical Wing Sections I, II, III," Lecture Notes in Economics and Mathematical Systems. Volumes 66, 108, 150. (1972, 1975, 1977). Springer-Verlag. Berlin / Heidelberg / New York.

[2] Bradshaw,P., Ferriss,D.H., Atwell,N.P., "Calculation of Boundary-Layer Development Using the Turbulent Energy Equation," Journal of Fluid Mechanics, Vol. 28, part 3, pp. 593-616, 1967.

[3] Bradshaw,P., Ferriss,D.H., "Calculation of Boundary-Layer Development Using the Turbulent Energy Equation: Compressible Flow on Adiabatic Walls," Journal of Fluid Mechanics, Vol. 46, part 1, pp. 83-110, 1970.

[4] Brandt, A., "Multi-Level Adaptive Solutions to Boundary-Value Problems," Math. of Comp., Vol.31, No.138, pp.333-390, April 1977.

[5] Carlson,L.A., "Transonic Airfoil Analysis and Design Using Cartesian Coordinates," Journal of Aircraft, Vol. 13, May 1976.

[6] Carter,J.E., "A New Boundary Layer Inviscid Iteration Technique for Separated Flow," AIAA-79-1450, 1979.

[7] Cebeci,T., Bradshaw,P., Momentum Transfer in Boundary Layers, McGraw-Hill, New York, 1977.

[8] Childs,R.E., Pulliam,T.H., "A Newton Multigrid Method for the Euler Equations" AIAA-84-0430, presented at AIAA 22nd Aerospace Sciences Meeting, January 9-12, 1984.

[9] Clauser,F.H., "Turbulent Boundary Layers in Adverse Pressure Gradients," Journal of Aeronautical Sciences, Vol. 21, No. 2, pp. 91-108, February 1954.

[10] Coles,D.E., "The Law of the Wake in the Turbulent Boundary Layer," Journal of Fluid Mechanics, Vol. 1, part 2, pp. 193-226, 1956.

[11] Coles,D.E., "The Turbulent Boundary Layer in a Compressible Fluid" R-403-PR, September 1962, Rand Corporation, Santa Monica, CA.

[12] Cook,P.H., McDonald,M.A., Firmin,M.C.P., "Aerofoil RAE 2822 Pressure Distributions and Boundary Layer and Wake Measurements," in Experimental Data Base for Computer Program Assessment, AGARD AR-138, 1979.

[13] Drela,M., "A New Transformation and Integration Scheme for the

Compressible Boundary Layer Equations, and Solution Behavior at Separation," MIT Gas Turbine & Plasma Dynamics Laboratory Report No. 172.

[14] Drela,M., Giles,M.B., Thompkins,W.T., "Conservative Streamtube Solution of Steady-State Euler Equations," AIAA-84-1643, presented at AIAA 17th Fluid Dynamics, Plasma Dynamics and Lasers Conference, June 25-27, 1984.

[15] Drela,M., Giles,M.B., Thompkins,W.T., "Newton Solution of Coupled Euler and Boundary Layer Equations," presented at the Third Symposium on Numerical and Physical Aspects of Aerodynamic Flows, Long Beach, California, Jan. 1985.

[16] Eberle,A., "A method of finite volumes for the calculation of transonic potential flow about wings using the minimum pressure integral," translation of MBB-Report UFE 1407(0), Feburary 1978.

[17] Edwards,D.E., Carter,J.E., "A Quasi-Simultaneous Finite Difference Approach for Strongly Interacting Flow," presented at the Third Symposium on Numerical and Physical Aspects of Aerodynamic Flows, Long Beach, California, Jan. 1985.

[18] Fulker,J.L., "Aerodynamic Data for Three Supercritical Aerofoils, RAE(NPL) 9515 and 9530, and RAE 9550," ARC R&M Report No. 3820, HMSO, London, 1978.

[19] Giles,M.B., "Newton Solution of Steady Two-Dimensional Transonic Flow," PhD Thesis, Department of Aeronautics and Astronautics, MIT, June 1985.

[20] Giles,M.B., Drela, M., "Newton Solution of Direct and Inverse Transonic Euler Equations," AIAA-85-1530, presented at the AIAA 7th Computational Fluid Dynamics Conference, Cincinati, Ohio, July 15-17, 1985.

[21] Gleyzes,C., Cousteix,J., Bonnet,J.L., "A Calculation Method of Leading Edge Separation Bubbles," presented at the Second Symposium on Numerical and Physical Aspects of Aerodynamic Flows, Long Beach, California, Jan. 1983.

[22] Goldberg,P., "Upstream History and Apparent Stress in Turbulent Boundary Layers," MIT Gas Turbine Laboratory Report No. 85, 1966.

[23] Green,J.E., "Application of Head's Entrainment Method to the Prediction of Turbulent Boundary Layers and Wakes in Compressible Flow," ARC R&M Report No. 3788, HMSO, London, 1977.

[24] Green,J.E., Weeks, D.J., Brooman, J.W.F. "Prediction of Turbu-

lent Boundary Layers and Wakes in Compressible Flow by a Lag-Entrainment Method," ARC R&M Report No. 3791, HMSO, London, 1977.

[25] Hastings,R.C., Williams,B.R., "Studies of the Flow Field near an NACA 4412 Aerofoil at nearly Maximum Lift," presented at the Third Symposium on Numerical and Physical Aspects of Aerodynamic Flows, Long Beach, California, Jan. 1985.

[26] Hicks,R.M., "Transonic Wing Design Using Potential Flow Codes - Successes and Failures," SAE paper 810565, 1981.

[27] Jespersen,D.C., "Recent Developments in Multigrid Methods for the Steady Euler Equations," Lecture Series on Computational Fluid Dynamics at Von Karman Institute for Fluid Dynamics, March 12-16, 1984.

[28] Kline,S.J., Morovkin,M.V., Sovran,G., Cockrell,D.J., Coles,D.E., Hirst,E.A., (Editors), proceedings of Computation of Turbulent Boundary Layers - 1968 AFOSR-IFP-Stanford Conference, Volumes I and II, Stanford University, CA.

[29] Le Balleur,J.C., "Strong Matching Method for Computing Transonic Viscous Flows Including Wakes and Separations. Lifting Airfoils," La Recherche Aerospatiale, No. 1981-3, English Edition, pp. 21-45, 1981-1983.

[30] Liebeck,R.H., Camacho,P.P., "Airfoil Design at Low Reynolds Number with Constrained Pitching Moment," presented at the Conference on Low Reynolds Number Airfoil Aerodynamics, UNDAS-CP-77B123, University of Notre Dame, June 1985.

[31] Liepmann,H.W., Roshko,A., Elements of Gasdynamics, Wiley, New York, 1957.

[32] Lighthill,M.J., "A New Method of Two-Dimensional Aerodynamic Design," R&M 2112, Aeronautical Research Council, June 1945.

[33] Lighthill,M.J., "A Mathematical Method of Cascade Design," R&M 2104, Aeronautical Research Council, June 1945.

[34] Lighthill,M.J., "On Displacement Thickness," Journal of Fluid Mechanics, Vol. 4, 1958, pp. 383-392.

[35] Mack,L.M., "Transition and Laminar Instability," JPL Publication 77-15, 1977.

[36] Mellor,G.L., Gibson,D.M., "Equilibrium Turbulent Boundary Layers," Journal of Fluid Mechanics, Vol. 24, part 2, pp. 225-253.

[37] Mellor,G.L., "The Effects of Pressure Gradients on Turbulent Flow near a Smooth Wall," Journal of Fluid Mechanics, Vol. 24, part 2, pp. 255-274.

[38] Melnik,R.E., "Turbulent Interactions on Airfoils at Transonic Speeds Recent Developments," in AGARD-CP-291, 1980.

[39] Novak,R.A., "Streamline Curvature Computing Procedures for Fluid-Flow Problems," ASME Paper No.66-WA/GT-3, presented at the Winter Annual Meeting of the American Society of Mechanical Engineers, November 1966.

[40] Obremski,H.J., Morovkin,M.V., Landahl,M.T., "A Portfolio of Stability Characteristics of Incompressible Boundary Layers," AGARD-ograph 134, NATO 1969, Neuilly Sur Seine, France.

[41] Salas,M.D., Jameson,A., Melnik,R.E., " A Comparative Study of the Nonuniquness Problem of the Potential Equation,", AIAA-83-1888, presented at the AIAA 6th CFD Conference at Danvers, Massachusetts, July 13-15, 1983.

[42] Schetz,J.,A., Foundations of Boundary Layer Theory for Momentum, Heat, and Mass Transfer, Prentice-Hall, Englewood Cliffs, New Jersey, 1984.

[43] Sloof,J.W., "A Survey of Computational Methods for Subsonic and Transonic Aerodynamic Design," Proceedings, International Conference on Inverse Design Concepts in Engineering Sciences, 1984.

[44] Stanewsky,E., Puffert,W., Müller,R., Bateman,T.E.B., "Supercritical Airfoil CAST 7 - Surface Pressure, Wake and Boundary Layer Measurements," in Experimental Data Base for Computer Program Assessment, AGARD AR-138, 1979.

[45] Swafford,T.W., "Analytical Approximation of Two-Dimensional Separated Turbulent Boundary-Layer Velocity Profiles," AIAA Journal, Vol. 21, No. 6, pp 923-926.

[46] Thomas,J.L., "Integral Boundary-Layer Models For Turbulent Separated Flows," AIAA-84-1615, presented at AIAA 17th Fluid Dynamics, Plasma Dynamics, and Lasers Conference, June 25-27, 1984.

[47] Thompson,J.F., Thames,F.C., Mastin,C.W , "Automatic Numerical Generation of Body-Fitted Curvilinear Coordinate System for Field Containing Any Number of Arbitrary Two-Dimensional Bodies," Journal of Computational Physics, Vol. 15, pp. 299-319, 1974.

[48] Tranen,T.L., "A Rapid Computer Aided Transonic Airfoil Design Method," AIAA-74-0501, 1974.

[49] Vanderplaats,G.N., "An Efficient Algorithm for Numerical Airfoil Optimization," AIAA-79-0079, 1979.

[50] Veldman,A.E.P., "The Calculation of Incompressible Boundary Layers with Strong Viscous-Inviscid Interaction," in AGARD-CP-291, 1980.

[51] Volpe,G., Melnik,R.E., "The Design of Transonic Airfoils by a Well-Posed Inverse Method," Proceedings, International Conference on Inverse Design Concepts in Engineering Sciences, 1984.

[52] White,F.M., Viscous Fluid Flow, McGraw-Hill, New York, 1974.

[53] Whitfield,D.L., "Analytical Description of the Complete Turbulent Boundary Layer Velocity Profile," AIAA-78-1158, July 1978.

[54] Whitfield,D.L., "Integral Solution of Compressible Turbulent Boundary Layers Using Improved Velocity Profiles," Arnold Air Force Station, AEDC-TR-78-42, 1978.

[55] Whitfield,D.L., Swafford, T.W., Jacocks, J.L., "Calculation of Turbulent Boundary Layers with Separation and Viscous-Inviscid Interaction," AIAA Journal, Vol. 19, No. 10, pp. 1315-1322, October 1981.

[56] Wigton,L.B., Holt,M., "Viscous-Inviscid Interaction in Transonic Flow," AIAA-81-1003, presented at AIAA 5th CFD Conference, June 22-23, 1981.

[57] Wornom,S.F., "Application of two-point difference schemes to the conservative Euler equations for one-dimensional flows," NASA TM-83262, May 1982.

[58] Wortmann,F.X., "Airfoils With High Lift/Drag Ratio at a Reynolds Number of About One Million," Proceedings of the Second International Symposium on the Technology and Science of Motorless Flight, MIT, Cambridge, MA, 1974.

[59] Wu,C.H., "Matrix Solution of Compressible Flow on S Surface Through a Turbomachine Blade Row With Splitter Vanes or Tandem Blades," ASME Paper No.83-GT-10, presented at the 28tn International Gas Turbine Conference and Exhibit, March 27-31,1983.

APPENDIX A

Artificial Bulk Viscosity Stability Analysis

Steady transonic flow calculations require some sort of artificial dissipation primarily to exclude non-physical solutions to the Euler equations in the form of expansion shocks. Artificial dissipation prevents such solutions from appearing by ensuring that entropy will always increase across shock waves. The primary mechanism of entropy production in shock waves, namely bulk viscosity, has been lost in the process of simplifying the Navier-Stokes equations to the Euler equations. The artificial dissipation which is added to the inviscid Euler equations in the present formulation in supersonic regions is qualitatively similar to this "lost" bulk viscosity and thus permits proper calculation of shocked flows. This is analogous to the subsonic Kutta condition, which artificially replaces the "lost" viscous mechanism of circulation establishment via vorticity shedding. The effective bulk viscosity (which is generally much greater than physical bulk viscosity), automatically produces shock waves which are just thick enough to be resolved by the available grid spacing.

Well-established potential flow calculation methods generally employ a different form of artificial dissipation, namely density upwinding (also called "artificial compressibility"). Giles [19] also used density upwinding with the present Euler discretization scheme to obtain stable transonic solutions. The present artificial bulk viscosity formulation was derived by Giles [unpublished] as a more physically realistic alternative to density upwinding. His analysis is presented below.

Consider a uniform compressible flow in a constant area channel. The Euler equations which govern this flow are

$$\rho q \equiv m = \text{constant} \qquad (A.1)$$

$$m\left(q - \lambda\Delta x\frac{dq}{dx}\right) + p = \text{constant} \qquad (A.2)$$

$$\frac{\gamma}{\gamma-1}\frac{p}{\rho} + \frac{1}{2}q^2 = \text{constant} \qquad (A.3)$$

The artificial bulk viscosity is introduced via the derivative term in the momentum equation (A.2). The coefficient λ, whose proper value will be determined shortly is O(1), and Δx is a small length scale which will be set to the local grid spacing in the discrete analysis given later.

Each variable is now expressed as the sum of a base value and a perturbation, denoted by an overbar and an apostrophe, respectively.

$$p = \bar{p}(1+p') \qquad \rho = \bar{\rho}(1+\rho') \qquad q = \bar{q} + \bar{c}q' \qquad (A.4a\text{-}c)$$

where $\bar{c}$ denotes the local speed of sound.

Substituting these variables into equations (A.1-3) and neglecting second order terms, the resulting linearized equations are:

$$M\rho' + q' = 0 \qquad (A.4)$$

$$\gamma M\left(q' - \lambda\Delta x\frac{dq'}{dx}\right) + p' = 0 \qquad (A.5)$$

$$p' - \rho' + (\gamma-1)Mq' = 0 \qquad (A.6)$$

where $M = \bar{q}/\bar{c}$ is the Mach number of the base flow.

Eliminating ρ' and p' between equations (A.4-6) gives a first order ODE for q'.

$$\frac{dq'}{dx} - kq' = 0 \qquad \text{where} \quad k = \frac{1}{\lambda\Delta x\gamma}\left(1 - \frac{1}{M^2}\right) \qquad (A.7)$$

Equation (A.7) has exponential solutions of the form

$$q' \propto e^{kx} \qquad (A.8)$$

The most important characteristic of solution (A.8) is that k changes sign through M=1. In supersonic regions k>0, which means that perturbations decay away exponentially upstream with a length constant of

$O(\Delta x)$. In subsonic regions, such perturbations decay away downstream. This behavior permits perturbation solutions which mimic a normal shock where M goes through unity, since the perturbations decay away from the shock to uniform flow on both sides. Figure A.1 illustrates this behavior.

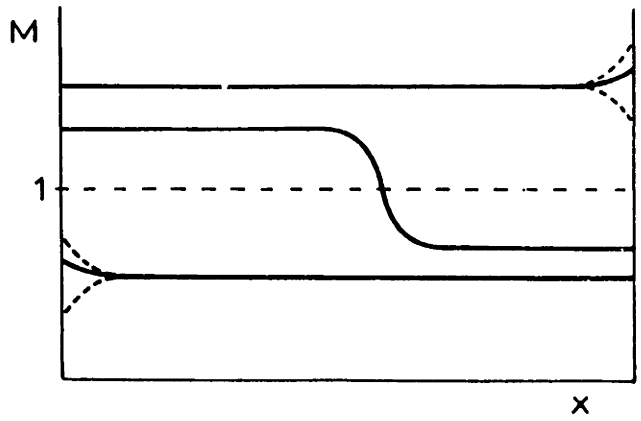

Figure A.1 "Boundary layer" behavior of perturbation solutions

The discrete counterpart of the continuous system (A.1-3) can be expressed as

$$\rho_2 q_2 \equiv m = \text{constant} \tag{A.9}$$

$$m\left(q_2 - \lambda(q_2 - q_1)\right) + p_2 = \text{constant} \tag{A.10}$$

$$\frac{\gamma}{\gamma-1}\frac{p_2}{\rho_2} + \frac{1}{2}q_2^2 = \text{constant} \tag{A.11}$$

Where the subscripts "1" and "2" denote two adjacent nodes separated by the distance Δx. Using the perturbation forms (A.4a-c), the above discrete equations become

$$M\rho_2' + q_2' = 0 \tag{A.12}$$

$$\gamma M\left(q_2' - \lambda(q_2' - q_1')\right) + p_2' = 0 \tag{A.13}$$

$$p_2' - \rho_2' + (\gamma-1)q_2' = 0 \qquad (A.14)$$

Eliminating ρ' and p' from equations (A.12-14), the following difference equation for q' results.

$$(\lambda - \lambda_c)q_2' - \lambda q_1' = 0 \quad , \text{ where } \quad \lambda_c = \frac{1}{\gamma}\left(1 - \frac{1}{M^2}\right) \qquad (A.15a\text{-}b)$$

The solution to equation (A.15a) is

$$q_i' \propto z^i \quad , \text{ where } \quad z = \frac{\lambda}{\lambda - \lambda_c} \qquad (A.16a\text{-}b)$$

and i is the spatial node index.

Consistency with the analytic equations requires that the direction of perturbation decay is upstream for supersonic flow, and downstream for subsonic flow.

<u>For subsonic flow</u>: $M < 1$, implying $\lambda_c < 0$ and $z < 1$

From (A.16a) it can be seen that q' will decay downstream (i increasing) and consistency is always achieved.

<u>For supersonic flow</u>: $M > 1$, giving three cases depending on value of λ

1) $\lambda > \lambda_c \quad \Rightarrow \quad 1 < z < \infty$
   This gives the proper exponential decay upstream (i decreasing).

2) $\lambda_c > \lambda > \lambda_c/2 \quad \Rightarrow \quad -\infty < z < -1$
   This still gives upstream exponential decay, but since z is negative, it can be seen from (A.16a) that the perturbation q' will alternately change sign with each successive node, giving an oscillatory decay.

3) $\lambda_c/2 > \lambda > 0 \quad \Rightarrow \quad -1 < z < 0$
   This case produces exponential decay downstream, making the discrete equations inconsistent with the analytic system.

The consequence of having an insufficient level of artificial dissipation as in case 3) above is that the Jacobian of the Newton

solution procedure will be nearly singular if shocks or sonic lines are present. In such a situation it would be impossible to obtain a converged transonic flow solution. The proper level of artificial dissipation is influenced by other considerations besides numerical stability. The sharpest shocks are obtained when $\lambda = \lambda_c$, which produces the most rapid perturbation decay possible. Because the artificial dissipation is an "error term" in the Euler equation discretization proportional to λ, the smallest truncation errors result when $\lambda = \lambda_c/2$, which is its minimum value for numerical stability. Another consideration is the applicability (or lack thereof) of the above uniform 1-D analysis to the much more interesting case of non-uniform 2-D flow. This dictates a "margin of safety" where the stabilizing dissipation is introduced at high subsonic conditions rather than at M=1 exactly. The actual formula used for λ is

$$\begin{aligned} M < M_c: \quad & \lambda = 0 \\ M > M_c: \quad & \lambda = \frac{1}{\gamma}\left(1 - \frac{M_c^2}{M^2}\right) \end{aligned} \tag{A.17}$$

M is now the local Mach number and M_c is a threshold Mach number above which the dissipation coefficient λ is nonzero. Typically, M_c is set to lie between 0.80 and 0.95, depending on the strength of shock waves expected in the solution.

APPENDIX B

Airfoil Far Field

In this Appendix the leading order far field behavior for transonic flow past an isolated airfoil is derived. For simplicity, the coordinate system is aligned with the subsonic freestream flow u_∞.

Since the present numerical method requires a boundary condition to be imposed on the outer streamline, it is useful to analyze the far field behavior of the velocity potential Φ. The far field flow is isentropic and hence irrotational, apart from the entropy wake due to the shock, and so the governing equation for the velocity potential is

$$\left(\rho\Phi_x\right)_x + \left(\rho\Phi_y\right)_y = 0 \tag{B.1}$$

where
$$\rho = \rho_t \left(1 - \frac{u_\infty^2}{2h_t}\left(\Phi_x^2 + \Phi_y^2\right)\right)^{\frac{1}{\gamma-1}} \tag{B.2}$$

A perturbation potential ϕ is now defined by

$$\Phi_x \equiv \frac{u}{u_\infty} = 1 + \phi_x \qquad\qquad \Phi_y \equiv \frac{v}{u_\infty} = \phi_y \tag{B.3a-b}$$

With the assumption ϕ_x, $\phi_y \ll 1$, the first and second order terms of (B.1) give the following equation (Liepmann and Roshko [31]).

$$(1-M_\infty^2)\,\phi_{xx} + \phi_{yy} = M_\infty^2\left((\gamma+1)\phi_x\phi_{xx} + (\gamma-1)\phi_x\phi_{yy} + 2\phi_y\phi_{xy}\right) \tag{B.4}$$

A Prandtl-Glauert coordinate transformation,

$$\begin{pmatrix} x \\ y \end{pmatrix} = \begin{pmatrix} \beta\bar{x} \\ \bar{y} \end{pmatrix} \qquad \text{where} \qquad \beta = (1-M_\infty^2)^{\frac{1}{2}} \tag{B.5}$$

transforms equation (B.4) into

$$\phi_{\bar{x}\bar{x}} + \phi_{\bar{y}\bar{y}} = M_\infty^2\left(\frac{\gamma+1}{\beta^3}\,\phi_{\bar{x}}\phi_{\bar{x}\bar{x}} + \frac{\gamma-1}{\beta}\,\phi_{\bar{x}}\phi_{\bar{y}\bar{y}} + \frac{2}{\beta}\,\phi_{\bar{y}}\phi_{\bar{x}\bar{y}}\right) \tag{B.6}$$

In the limit $\bar{x}^2+\bar{y}^2 \to \infty$, where $\nabla\phi \to 0$, the lowest order solution ϕ^0 satisfies the Laplacian lefthand side of (B.6), and is expressed as

$$\phi^0 = \frac{\Sigma}{2\pi} \ln(\bar{r}) - \frac{\Gamma}{2\pi} \Theta \tag{B.7}$$

where $\Theta \equiv \arctan(\bar{y}/\bar{x})$ and $\bar{r} \equiv (\bar{x}^2+\bar{y}^2)^{\frac{1}{2}}$

Physically this statement means that in the far field the airfoil appears to first order to be the sum of a vortex of strength Γ and a source of strength Σ. The vortex is due to the circulation around the airfoil, and the source is due to the shock produced entropy change, and also includes the effects of the viscous wake in Chapter 6.

The next higher order solution ϕ^1 to equation (B.6) consists of doublet terms and is related to the airfoil cross-sectional area, or "blockage", and to the pitching moment on the airfoil. An inhomogeneous term proportional to $(\Gamma M_\infty)^2$ from the lower order solution ϕ^0 also appears. The inhomogeneous term from the source is neglected here.

$$\phi^1 = \frac{D_x}{2\pi} \frac{\cos\Theta}{\bar{r}} + \frac{D_y}{2\pi} \frac{\sin\Theta}{\bar{r}} + \left(\frac{\Gamma M_\infty}{2\pi}\right)^2 \left(E \frac{\ln(\bar{r})}{\bar{r}} \cos\Theta + F \frac{\cos 3\Theta}{\bar{r}} \right) \tag{B.8}$$

where

$$E = \frac{1}{4}\left(\frac{\gamma+1}{\beta^3} + \frac{3-\gamma}{\beta}\right) \qquad \text{and} \qquad F = \frac{-1}{16}\left(\frac{\gamma+1}{\beta^3} + \frac{\gamma+1}{\beta}\right)$$

The net perturbation velocity potential ϕ which governs the airfoil far field is then simply

$$\phi = \phi^0 + \phi^1 \tag{B.9}$$

The velocity potential ϕ as defined above contains the quantities Σ, Γ, D_x, D_y which must be properly constrained for a well posed problem. An appropriate constraint on Γ is the Kutta condition as discussed in Chapter 3. Σ is calculated directly from the difference

between the actual mass flux in the wake infinitely far downstream and the mass flux of the equivalent irrotational, isentropic flow.

$$\Sigma = \int_{\text{wake}} \left(1 - \frac{\rho u}{\rho_\infty u_\infty}\right) dy = \int \left(\frac{1}{\rho u} - \frac{1}{\rho_\infty u_\infty}\right) dm \qquad (B.10)$$

Σ has two contributions. The first term is due to the inviscid entropy wake behind a shock, and the other is due to the viscous wake.

$$\Sigma = \Sigma_i + \Sigma_v \qquad (B.11)$$

Ideally, one would like to evaluate integral (B.10) very far downstream. If it is evaluated near the airfoil, the airfoil's pressure field will affect the value of ρu in the integrand and thus cause errors in Σ. However, the far-downstream value of ρu can be accurately calculated from the local stagnation pressure, since the stagnation pressure is invariant along any streamline behind the airfoil. Using the known values of the far-field stagnation enthalpy h_t and static pressure p_∞, this is done as follows.

$$u^2 = 2h_t\left(1 - \frac{p_\infty}{p_t}\right)^{\frac{\gamma-1}{\gamma}} \qquad (B.12)$$

and,

$$\rho = \frac{\gamma}{\gamma-1}\frac{p_\infty}{h_t}\left(\frac{p_t}{p_\infty}\right)^{\frac{\gamma-1}{\gamma}} \qquad (B.13)$$

Hence, $\rho u = f(h_t, p_t, p_\infty)$ and so the contribution Σ_i to the integral in (B.10) from the entropy wake due to the shock can be written as

$$\Sigma_i = \int \left(\frac{1}{f(h_t,\ p_t,\ p_\infty)} - \frac{1}{\rho_\infty u_\infty}\right) dm \qquad (B.14)$$

The contribution to the integral in (B.10) from the viscous wake

is simply the wake displacement thickness far downstream.

$$\Sigma_v = \delta^*_{+\infty} \tag{B.15}$$

It is still necessary to define the doublet coefficients D_x and D_y in equation (B.8) since it is needed to define the full potential Φ in the far field. As described in Chapter 3, Φ is used to determine the pressures which are specified as boundary conditions on the top and bottom streamlines. Barring truncation errors and terms in ϕ of higher order than ϕ^1, these boundary conditions should produce streamlines which lie in the direction of $\nabla\Phi$. It is therefore appropriate to define the doublet coefficients D_x and D_y in ϕ^1 such that the integral

$$I \equiv \frac{1}{2} \int \left| \nabla\phi \times \hat{\mathbf{s}} \right|^2 ds \tag{B.16}$$

is minimized. The integration is performed over the top and bottom streamline boundaries and $\hat{\mathbf{s}}$ is the unit vector parallel to the streamline. The conditions which determine D_x and D_y are then

$$\frac{\partial I}{\partial D_x} = \int \left| \nabla\phi \times \hat{\mathbf{s}} \right| \left| \frac{\partial \nabla\Phi}{\partial D_x} \times \hat{\mathbf{s}} \right| ds = 0 \tag{B.17}$$

$$\frac{\partial I}{\partial D_y} = \int \left| \nabla\phi \times \hat{\mathbf{s}} \right| \left| \frac{\partial \nabla\Phi}{\partial D_y} \times \hat{\mathbf{s}} \right| ds = 0 \tag{B.18}$$

In effect, D_x and D_y are chosen such that the two farthest streamlines lie along $\nabla\Phi$ as closely as possible.

APPENDIX C

Airfoil Drag Calculation

The total drag on an isolated airfoil can be calculated using a momentum balance. Coordinate axes are chosen so that the freestream velocity u_∞ is in the x direction. A control volume with outward unit normal $\hat{n}$ is constructed around the airfoil such that two of its boundaries are streamlines. The drag D on the airfoil can now be expressed by a surface integral over the control volume.

$$D = -\int \left((p-p_\infty) n_x + (\rho \vec{u} \cdot \hat{n}) u \right) ds \qquad (C.1)$$

$p-p_\infty = O(r^{-1})$ and $n_x = O(r^{-1})$ on the streamline sides and the length of these two sides is $O(r)$, so the integral contribution from these two sides is at most $O(r^{-1})$ and hence can be neglected. The integral contribution from the other two sides can be rewritten as,

$$D = \int_0^{m_{tot}} \left(\left(\frac{p-p_\infty}{\rho u} + u \right)_1 - \left(\frac{p-p_\infty}{\rho u} + u \right)_2 \right) dm \qquad (C.2)$$

where the integration variable now is $dm = \rho u \, dy$, the incremental mass flux through the control volume, and subscripts "1" and "2" denote the inlet and outlet values, respectively. For streamtubes which are not in either the viscous wake or the entropy wake behind a shock, $p-p_\infty$ and $u-u_\infty$ are both $O(r^{-1})$ so the integrand is $\frac{p_1-p_2}{\rho_\infty u_\infty} + u_1-u_2 + O(r^{-2})$. However for isentropic streamtubes $dp + \rho u \, du = 0$ and hence the integrand is $O(r^{-2})$ and so the integral over isentropic streamtubes can be neglected. Finally the viscous and entropy wakes have widths of $O(1)$ so the contribution of the pressure term can be neglected. This leaves the following simple expression for the total drag.

$$D = \int (u_1 - u_2)\, dm \tag{C.3}$$

where the integral is over the viscous wake and the entropy wake due to a shock as shown in Figure C.1.

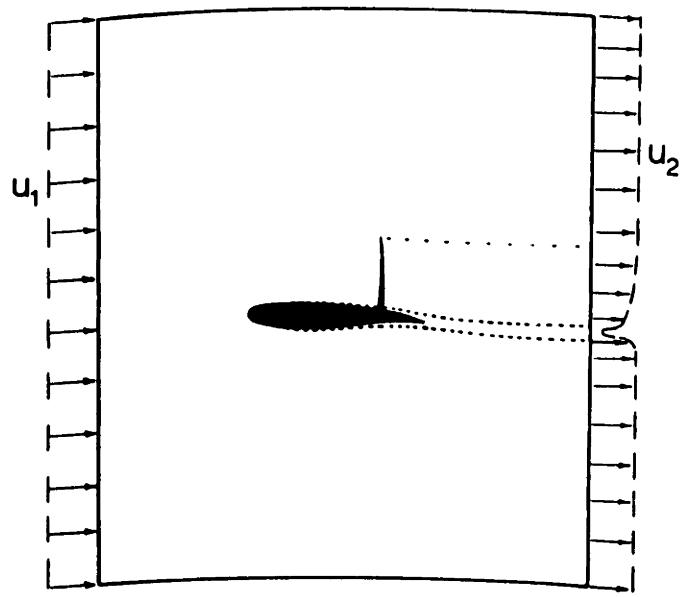

Figure C.1 Momentum defect in shock and viscous wakes

This equation is still approximate, containing errors of $O(r^{-1})$ which disappear in the limit $r \to \infty$. In calculating the drag due to a shock this equation can be made exact by using the stagnation pressure. The velocity is related to the pressure, stagnation pressure, and stagnation enthalpy by,

$$q^2 = 2h_t\left(1 - \frac{p}{p_t}\right)^{\frac{\gamma-1}{\gamma}} \tag{C.4}$$

Thus the drag is given by,

$$D = (2h_t)^{\frac{1}{2}} \int \left[\left(1 - \left(\frac{p_\infty}{p_t}\right)^{\frac{\gamma-1}{\gamma}}_1\right)^{\frac{1}{2}} - \left(1 - \left(\frac{p_\infty}{p_t}\right)^{\frac{\gamma-1}{\gamma}}_2\right)^{\frac{1}{2}}\right] dm \tag{C.5}$$

The range of integration in (C.3) was over the streamtubes lying in the viscous wake or coming through the shock. In (C.5) however the integrand is zero for isentropic streamtubes so the integration may be taken over all of the streamtubes, thus simplifying the programming. Also because equation (C.5) only involves stagnation pressure, which is invariant after the flow passes through the shock, the calculated drag is independent of r, and so is exact because it is exact in the limit $r \to \infty$.

This method of determining the total drag has two main advantages over the alternate method, which is to integrate the pressure and shear stress on the airfoil surface. The first is that for subsonic airfoils at high Reynolds number the numerical truncation error in numerically integrating the pressure may be comparable in magnitude to the total drag. With the method outlined here the only drag contribution comes from the wake and is equal to $\rho_\infty u_\infty^2 \theta$, where θ is the viscous plus the shock wake momentum thickness. This method has much lower numerical errors.

The second advantage is that the pressure drag on the airfoil is very sensitive to errors in the angle of attack, so if the effective angle of attack is slightly different from the far-field angle of attack which is prescribed the difference can cause a significant change in the calculated drag. The momentum balance method by contrast is insensitive to such discrepancies and so it is probably more accurate particularly when the far-field boundary is only a few chord lengths from the airfoil.

APPENDIX D

Orr-Sommerfeld Amplification Curve Calculation

The two-dimensional Orr-Sommerfeld equation governs the growth or decay of infinitesimal wavelike disturbances in parallel shear flows. It is derived from the unsteady Navier-Stokes equations with suitable thin-shear-layer and parallel-flow simplifications. A detailed derivation and discussion is given in Cebeci and Bradshaw [6]. Here it will suffice to say that a disturbance streamfunction of the form

$$\psi(\xi,\eta,t) = \phi(\eta)\, e^{-i(\alpha\xi - \omega t)} \tag{D.1}$$

is added to some base solution of the governing equations, where ξ,η are suitably non-dimensionalized streamwise and normal shear layer coordinates, and t is the time coordinate. When the higher powers of ϕ are neglected, the 4th-order Orr-Sommerfeld equation results. With $(\,)' = d/d\eta$, it is written below as a first-order system.

$$\phi' = \phi_1 \tag{D.2a}$$

$$\phi_1' = \alpha^2\phi + \phi_2 \tag{D.2b}$$

$$\phi_2' = \phi_3 \tag{D.2c}$$

$$\phi_3' = \alpha^2\phi_2 + iR\left((\alpha u-\omega)\phi_2 - \alpha u''\phi\right) \tag{D.2d}$$

Appropriate boundary conditions are:

$\eta=0$:

$$\phi = 0 \tag{D.3a}$$

$$\phi_1 = 0 \tag{D.3b}$$

$\eta\to\infty$:

$$\phi_3 + \left(\alpha^2 + iR(\alpha u-\omega)\right)\phi_2 = 0 \tag{D.3c}$$

$$\phi_3 + \alpha\phi_2 - iR(\alpha u-\omega)\left(\phi_1 + \alpha\phi\right) = 0 \tag{D.3d}$$

Here R is is the Reynolds number formed with the reference quantities, and $u = u(\eta)$ is the given velocity profile about which the perturbation is taken. The two wall boundary conditions (D.3a-b) are simply the usual no-transpiration and no-slip conditions, and the two far-field boundary conditions (D.3c-d) ensure that ϕ is well behaved as $\eta \to \infty$.

In general, ϕ, α, ω are all complex. The spatial amplification problem results when α is complex and ω is real. In particular, $u(\eta)$, R, and ω are prescribed, and the homogeneous Orr-Sommerfeld equation (D.2) and its boundary conditions (D.3) form an eigenvalue problem for the complex wavenumber α. Equations (D.2) and (D.3) are readily discretized using a second order accurate finite-difference box scheme with complex Fortran arithmetic. Because of the homogeneity of the problem, it is appropriate to impose the normalization condition

$$\eta=0: \qquad \phi_2 = 1 + i \tag{D.4}$$

as an additional equation. Newton's method is applied to the resulting nonlinear system for the nodal unknowns ϕ, ϕ_1, ϕ_2, ϕ_3, and the global unknown α. This produces a block tridiagonal system with complex 4×4 blocks and two righthand sides which is very rapidly solved by a standard block elimination algorithm.

From (D.1), it is clear that the sought-after spatial growth rate of the disturbance field is equal to $-\mathrm{Im}(\alpha)$. The overall procedure which was used to generate the amplification curves in Figure 6.7 for each velocity profile shape parameter H is as follows.

* Generate the appropriate Falkner-Skan velocity profile $u(\eta;H)$
* For each of about 10 distinct frequencies ωR
  - Determine the instability range of R (for which $\mathrm{Im}(\alpha) < 0$)
  - For each of about 15 values of R in the instability range
    - Solve equations (D.2-4) to obtain $\alpha(R)$
  - Spline and integrate $\mathrm{Im}(\alpha)$ over R to get the amplification ratio

APPENDIX E

Grid Generation

Initial grid generation

The initial grid generation uses an elliptic generation method developed by Thompson [47]. The position of grid nodes on the airfoil surface, stagnation streamline and far-field boundary are specified by the user through an input file. The grid points in the interior are determined by the elliptic differential equations,

$$\xi_{xx} + \xi_{yy} = 0 \tag{E.1}$$

$$\eta_{xx} + \eta_{yy} = 0 \tag{E.2}$$

which defines a transformation from physical space (x,y) to computational space (ξ,η). After interchanging dependent and independent variables, the above two equations become,

$$\alpha\, x_{\xi\xi} - 2\beta\, x_{\xi\eta} + \gamma\, x_{\eta\eta} = 0 \tag{E.3}$$

$$\alpha\, y_{\xi\xi} - 2\beta\, y_{\xi\eta} + \gamma\, y_{\eta\eta} = 0 \tag{E.4}$$

where

$$\alpha = x_{\eta}^2 + y_{\eta}^2 \quad , \quad \beta = x_{\xi}x_{\eta} + y_{\xi}y_{\eta} \quad , \quad \gamma = x_{\xi}^2 + y_{\xi}^2 \tag{E.5a-c}$$

In the computational space the line ξ=0 corresponds to the physical inlet boundary, the line ξ=1 corresponds to the outlet boundary, the line η=0 corresponds to the stagnation streamline and suction surface of the airfoil, and the line η=1 corresponds to the stagnation streamline and the pressure surface displaced upwards by one pitch, as illustrated in Figure E.1. The grid is defined to be uniformly spaced in the ξ direction, but since the lines η=constant are to be approximately streamlines the spacing in the η direction is defined to be proportional to the fractional mass flux through each streamtube.

Equations (E.3) and (E.4) are solved using SLOR (successive line

over-relaxation), with α,β,γ held fixed during each iteration and then updated afterwards. Convergence is achieved in about 20 iterations and the resultant grid is often so good an initial guess that it can hardly be distinguished from the final grid obtained from the full Euler calculation. This is not so surprising since the initial streamline grid is the incompressible solution for a given stagnation streamline because η satisfies the incompressible streamfunction equation (E.1).

Grid Redistribution

During the Newton iterations the discrete Euler equations determine the movement of the grid nodes in the direction normal to the streamlines, but there is nothing in the physics of the problem to determine the streamwise movement of the grid nodes. This is completely arbitrary, and is only really important near the leading edge where large movements of the leading edge stagnation point can distort the grid. To correct this a slightly modified version of the grid-generation algorithm is used occasionally to redistribute the grid nodes to maintain a good grid. The modification consists of weighting the $\Delta\eta$ metrics in the finite difference expression of (E.4) by $1/\rho$, where ρ is the local density obtained from the latest Newton iteration. In a parallel flow with a normal entropy gradient, such as a far shock wake, this produces the correct streamtube area distribution. In non-parallel flows, this modification tends to preserve the compressible streamline pattern generated by the Euler solver.